การศึกษาการปลูกและขั้นตอนการเตรียมแบบอินซิตูของโครงสร้างอินเดียมอาร์เซไนด์ควอนตัมด็อตชนิดจัดเรียงตัวเองเพื่อประยุกต์ที่ความยาวคลื่นยาว

นางสาวฤดีสันต์ ส่องเมือง

วิทยานิพนธ์นี้เป็นส่วนหนึ่งของการศึกษาตามหลักสูตรปริญญาวิศวกรรมศาสตรดุษฎีบัณฑิต
สาขาวิชาวิศวกรรมไฟฟ้า ภาควิชาวิศวกรรมไฟฟ้า
คณะวิศวกรรมศาสตร์ จุฬาลงกรณ์มหาวิทยาลัย
ปีการศึกษา 2546

ISBN 974-17-3417-4

STUDY ON GROWTH AND IN-SITU PROCESSING OF INAS SELF-ORGANIZED QUANTUM DOTS FOR LONG WAVELENGTH APPLICATIONS

Mrs. Rudeesun Songmuang

A Dissertation Submitted in Partial Fulfillment of the Requirements
for the Degree of Doctor of Engineering in Electrical Engineering
Department of Electrical Engineering
Faculty of Engineering
Chulalongkorn University
Academic year 2003

ISBN 974-17-3417-4

Thesis Title	Study on Growth and In-Situ Processing of InAs Self-Organized Quantum Dots for Long Wavelength Applications
By	Mrs. Rudeesun Songmuang
Field of Study	Electrical Engineering
Thesis Advisor	Professor Dr. Somsak Panyakeow
Thesis Co-advisor	Dr. Oliver G. Schmidt

Accepted by the Faculty of Engineering, Chulalongkorn University in Partial Fulfillment of the Requirements for the Doctor's Degree

…… Dean of Faculty of Engineering
(Professor Somsak Panyakeow , D.Eng.)

THESIS COMMITTEE

…… Chairman
(Professor Virulh Sa-yakanit , Ph.D.)

…… Thesis Advisor
(Professor Somsak Panyakeow , D.Eng.)

……. Thesis Co-advisor
(Oliver G. Schmidt , Ph.D.)

…… Member
(Professor Shunri Oda , D.Eng.)

…… Member
(Professor Chua Soo-Jin , Ph.D.)

…… Member
(Associate Professor Montri Sawadsaringkarn , D.Ing.)

ฤดีสันติ์ ส่องเมือง : การศึกษาการปลูกและขั้นตอนการเตรียมแบบอินซิตูของโครงสร้างอินเดียมอาร์เซไนด์ควอนตัมด็อตชนิดจัดเรียงตัวเองเพื่อประยุกต์ที่ความยาวคลื่นยาว. (STUDY ON GROWTH AND IN-SITU PROCESSING OF INAS SELF-ASSEMBLED QUANTUM DOTS FOR LONG WAVELENGTH APPLICATIONS)อ. ที่ปรึกษา : ศ.ดร. สมศักดิ์ ปัญญาแก้ว, อ. ที่ปรึกษาร่วม Dr. Oliver G. Schmidt, 134 หน้า. ISBN 974-17-3417-4.

วัตถุประสงค์ของวิทยานิพนธ์ฉบับนี้สามารถแบ่งออกเป็น 2 ส่วนสำคัญคือ การศึกษาการกระบวนการปลูกกลบโครงสร้างอินเดียมอาร์เซไนด์ควอนตัมด็อตเพื่อที่ประยุกต์ที่ใช้ที่ความยาวคลื่นยาว และการศึกษาการใช้ความเครียดที่เกิดขึ้นในชั้นแกลเลียมอาร์เซไนด์รวมกับกระบวนกัดแบบอินซิตูเพื่อสร้างโครงสร้างนาโนโฮล และควอนตัมด็อตโมเลกุล วิธีวิเคราะห์ตัวอย่างชิ้นงานในการทดลองได้แก่ การวัดด้วยแรงอะตอม (Atomic Force Microscopy) และ การวัดโฟโตลูมิเนสเซนต์ (Photoluminescence)

ควอนตัมด็อตที่ศึกษานี้คือควอนตัมด็อตขนาดใหญ่ที่มีความหนาแน่นน้อย ($3\text{-}6\times10^{9}$ ด็อตต่อตารางเซนติเมตร) จากการศึกษาผลของความเครียดและความหนาของชั้นอินเดียมแกลเลียมอาร์เซไนด์ที่ปลูกที่อุณหภูมิต่ำ เราพบว่าความสูงของควอนตัมด็อตลดลงอย่างรวดเร็วและมีการเปลี่ยนรูปเป็นโครงสร้างริดจ์วาลเลย์ ในช่วงแรกของการปลูกกลบควอนตัมด็อตด้วยแกลเลียมอาร์เซไนด์ และควอนตัมด็อตมีแนวโน้มที่จะคงรูปร่างเดิมไว้เมื่อถูกปลูกกลบด้วยอินเดียมแกลเลียมอาร์เซไนด์ การเปลี่ยนแปลงของควอนตัมด็อตเมื่อได้รับการปลูกกลบสามารถอธิบายได้ด้วยผลของพลังงานอิลาสติกและพลังงานพื้นผิวที่มีต่อเซอร์เฟสเคมิคอลโพเทนเชียล การเพิ่มขึ้นของพลังงานอิลาสติกและพลังงานพื้นผิวของชั้นปลูกทับจะทำให้อินเดียมอะตอมวิ่งออกจากควอนตัมด็อตไปยังพื้นผิวแกลเลียมอาร์เซไนด์ ดังนั้นการปลูกทับควอนตัมด็อตทำให้เกิดการไหลออกของอินเดียมอะตอมจากควอนตัมด็อตและการที่แกลเลียมอาร์เซไนด์ที่ปลูกทับควอนตัมด็อตไม่ก่อตัวด้านบนควอนตัมด็อตทำให้ความสูงของควอนตัมด็อตลดลงอย่างรวดเร็ว และเกิดโครงสร้างริดจ์วาลเลย์

ต่อมาเราได้ประยุกต์ใช้ความเครียดที่เกิดขึ้นในชั้นแกลเลียมอาร์เซไนด์กับกระบวนการกัดแบบอินซิตูด้วยอาร์เซนิกโบรไมด์ เพื่อสร้างโครงสร้างนาโนโฮล เราพบสองย่านสำคัญที่เกิดขึ้นคือย่านที่ความเครียดในชั้นปลูกทับเป็นตัวเร่งปฏิกริยาในการกัด ซึ่งจุดกำเนิดของการเกิดโครงสร้างนาโนโฮล ส่วนย่านที่สอง เราพบว่าเมื่อเริ่มเพิ่มเวลาการกัด ความลึกของหลุมมีแนวโน้มคงที่ แต่ความกว้างของหลุมยังคงเพิ่มขึ้น เนื่องจากอาร์เซนิกโบรไมด์มีแนวโน้มที่จะนำอะตอมแกลเลียมที่ขอบหลุมออกไปมากว่าอะตอมแกลเลียมที่บริเวณอื่น เมื่อเราสร้างโครงสร้างนาโนโฮลที่มีความสม่ำเสมอสูงได้แล้ว การปลูกผลึกอินเดียมอาร์เซไนด์ลงบนนาโนโฮลทำให้เกิดการก่อตัวของกลุ่มควอนตัมด็อตรอบขอบของนาโนโฮล ซึ่งเราให้ชื่อว่าควอนตัมด็อตโมเลกุล จำนวนของควอนตัมด็อตต่อโมเลกุลสามารถเพิ่มขึ้นได้จาก 2 ถึง 6 และมีการกระจายของปริมาณด็อตต่อโมเลกุลเพิ่มขึ้น เมื่อเราทำการลดอุณหภูมิแผ่นฐานลงขณะการทำปลูกอินเดียมอาร์เซไนด์ เนื่องมาจากการลดลงการระยะทางดิฟฟิวส์ของอินเดียมอะตอม จากผลการทดลองเราทำการเสนอโมเดลอย่างง่ายเพื่ออธิบายการเกิดควอนตัมด็อตโมเลกุล

ภาควิชา วิศวกรรมไฟฟ้า ลายมือชื่อนิสิต .....

สาขาวิชา วิศวกรรมไฟฟ้า ลายมือชื่ออาจารย์ที่ปรึกษา .....

ปีการศึกษา 2546

4371815221 : MAJOR ELECTRICAL ENGINEERING
KEY WORD: IN SITU ETCHING / SELF-ASSEMBLED QUANTUM DOTS / INAS/GAAS / MOLECULAR BEAM EPITAXY

RUDEESUN SONGMUANG: STUDY ON GROWTH AND IN-SITU PROCESSING OF INAS SELF-ASSEMBLED QUANTUM DOTS FOR LONG WAVELENGTH APPLICATIONS. THESIS ADVISOR : PROF. DR. SOMSAK PANYAKEOW, THESIS CO-ADVISOR: DR. OLIVER G. SCHMIDT, 134 pp. ISBN 974-17-3417-4.

The aim of this research work can be divided into 2 parts. First is to understand the overgrowth process of InAs/GaAs self-assembled quantum dots (QDs) to extend the emission wavelength to long wavelength region. Second is to combine strain modulation in GaAs cap layer with $AsBr_3$ *in situ* etching to create the new structures such as nanoholes and QD molecules. The properties of the investigated structure were measured by *ex-situ* atomic force microscopy (AFM) and photoluminescence (PL).

The investigated QD array is large, low-density QDs with density of about 3-6×10^9 cm^{-2}. The effects of strain and thickness of an $In_xGa_{1-x}As$ (x=0-0.2) cap layer grown at low temperature are systematically studied. The dot height drastically reduces and the dot shape transforms into an elongated ridge-valley structure at the early stage of GaAs overgrowth, while the dots tend to preserve their shape during InGaAs capping. The effects of elastic energy and surface energy included in the surface chemical potential can qualitatively explain the observed surface evolution. The emission wavelength from the QDs covered with InGaAs layer can be extended beyond 1.3 μm.

The strain modulation in GaAs cap layer was combined with $AsBr_3$ *in situ* etching process to create the nanoholes. The etching process can be divided into 2 regimes depending on the nominal etching depth and the thickness of the GaAs cap layer. In the first regime, nanoholes are formed ascribing to a strain selectivity of the etchant. Further supply of the etching gas causes the hole diameter to increase, while the depth stays approximately constant since the etching gas preferentially remove the atoms at the hole edge due to the less binding energy. InAs deposited on the filled-hole layer forms into groups of closely spaced self-assembled InAs QDs—termed lateral QD molecules. Deposition of InAs onto the nanoholes causes a preferential formation of the InAs QD molecules around the holes. The number of QDs per QD molecule ranges from 2 to 6, depending on the InAs growth conditions. By decreasing the substrate temperature, the number of QDs per QD molecule increases, but the statistical distribution is wider due to a reduced In atom diffusion length. From experimental results, we propose the simple model for QDs molecule formation.

Department ….Electrical Engineering.. Student's signature ……

Field of study ..Electrical Engineering. Advisor's signature ……

Academic year ……2003……

Acknowledgements

My biggest gratitude goes to Dr. Oliver G. Schmidt and Prof. Dr. Somsak Panyakeow, who accompanied this work with enthusiasm, especially for a chance to have an exciting experiences both life and science in MBE group, Max-Planck-Institute for Solid State Research, Stuttgart, Germany. Moreover, their suggestion, idea and knowledge always encourage me to continue doing a research.

I gratefully acknowledges all those who provided invaluable help during the research time at the Semiconductor Device Research Laboratory (SDRL), Department of Electrical Engineering, Faculty of Engineering, Chulalongkorn University. In particular, the author is deeply indebted to Associate Professor Dr. Montri Sawadsaringkarn, Associate Professor Dr. Choompol Antarasena, Assistant Professor Dr. Somchai Ratanathammaphan, and Assistant Professor Dr. Songphol Kanjanachuchai.

As always, this thesis could not have been completed without special helps of colleagues and members in the MBE group and the SDRL. These are colleagues at Max-Planck-Institute: Mrs. Claudia Müller, Mr. Henry Heidemeyer, Ms. Yvonne Manz, Mr. Ulrich Denker, Mr. Karsten Tötemeyer, Mr. Wolfgang Winter, Mr. Christoph Deneke, Dr. Neng Yun Jin-Phillipp, and colleagues at Chulalongkorn University: Mr. Supachok Thainoi, Dr. Suwat Sopitpan, Mrs. Kwanruan Thainoi. In addition, I would like to thank for seamless collaboration with Mr. Suwit Kiravittaya at both Chulalongkorn University and Max-Planck-Institute.

I would like to acknowledge the Royal Golden Jubilee (RGJ) scholarship for the research fund in Thailand and DAAD-RGJ scholarship and also Prof. Dr. Klaus von Klitzing for funding of a the short research program at Max-Planck-Institute for Solid State Research, Stuttgart, Germany.

Finally, I am profoundly indebted to my parents and all the friends for their encouragement and continuous supports during the time of difficulty.

CONTENTS

CONTENTS (continued)

CONTENTS (continued)

LIST OF FIGURES

Page

LIST OF FIGURES (continued)

Page

LIST OF FIGURES (continued)

Page

LIST OF FIGURES (continued)

Page

LIST OF FIGURES (continued)

Page

LIST OF FIGURES (continued)

Page

LIST OF FIGURES (continued)

Page

LIST OF FIGURES (continued)

Page

LIST OF FIGURES (continued)

Page

LIST OF SYMBOLS

a_e	lattice constant of deposited material
a_S	lattice constant of substrate material
A	surface area
AFM	atomic force microscopy
AlAs	aluminium arsenide
AlGaAs	aluminium gallium arsenide
AlP	aluminium phosphide
$AsBr_3$	arsenic tribromide
b	valence band (001) axial deformation potential or base of pyramidal quantum dot
CB	conduction band
CC	conventionally capped
δ	delta function
$\Delta\gamma$	change of surface free energy
$D_{bulk}(E)$	bulk density of state
$D_{QW}(E)$	quantum well density of state
$D_{QWR}(E)$	quantum wire density of state
$D_{QD}(E)$	quantum dot density of state
D.O.S.	density of state
ε	misfit
ε_0	lattice mismatch
$\varepsilon_{//}$	in-plane strain
$\varepsilon_{\perp}$	strain in perpendicular to the growth direction
E	carrier energy or total energy per unit cell
E_0	characteristic energy
E_g	band gap energy
$E_{n,x}$	quantized energy in x-direction
$E_{n,y}$	quantized energy in y-direction

LIST OF SYMBOLS (continued)

$E_{n,z}$	quantized energy in z-direction
E(el)	elastic strain energy
E_{WL}	energy of wetting layer
E_{island}	energy of single island
$E_{elastic}$	elastic strain energy
$E_{surface}$	island surface energy
E_{edge}	island edge energy
$F(\mathbf{r})$	envelope wave function
FWHM	full width at half maximum
γ_e	surface free energy of the epilayer/vacuum interface
γ_i	surface free energy of epilayer/substrate interface
γ_S	surface free energy of the substrate/vacuum interface
GaAs	gallium arsenide
GaP	gallium phosphide
Ge	germanium
h	Planck's constant
	or height of pyramidal quantum dot
$\hbar$	reduced Planck's constant
i	critical island size
InAs	indium arsenide
InGaAs	indium gallium arsenide
InGaP	indium gallium phosphide
InP	indium phosphide
k	amplitude of wave vector
k_B	Boltzmann's constant
$k_{//}$	amplitude of in-plane (y-z) wave vector
$k_{\perp}$	amplitude of wave vector in x-direction
$\mathbf{k} = (k_x, k_y, k_z)$	carrier wave vector
$\boldsymbol{k}_{in}$	wave vectors of incident electron
$\boldsymbol{k}_{diff}$	wave vectors of diffraction electron
λ	elastic modulus

LIST OF SYMBOLS (continued)

$\lambda_{\text{de Broglie}}$	de Broglie wavelength
l	quantum number in x-direction
L	macroscopic length scale
	or base size of pyramidal quantum dot
L_0	characteristic length
L_x	nanometer length scale in x direction
L_y	nanometer length scale in y direction
L_z	nanometer length scale in z direction
m	quantum number in y-direction
m^*	effective mass
MBE	molecular beam epitaxial
	or molecular beam epitaxy
MFC	mass flow controller
ML	monolayer
n	quantum number in z-direction
N_D	volume density of quantum dot
N_e	number of state per unit surface
N_{wi}	area density of quantum wire
p	carrier momentum
PL	photoluminescence
QW	quantum well
QWR	quantum wire
QD	quantum dot
ρ	quantum dot density
$\mathbf{r} = (x, y, z)$	carrier position vector
RHEED	reflection high-electron energy diffraction

LIST OF SYMBOLS (continued)

Re	rhenium
RT	room temperature
σ	Poisson's ratio
sccm	standard cubic centimeter
Si	silicon
SiGe	silicon germanium
STM	scanning tunneling microscopy
Θ	Heaviside's unit step function
t	film thickness
T	temperature
$V(\mathbf{r})$	confinement potential
W	tungsten
WL	wetting layer

CHAPTER 1

Introduction

During the last few years, heteroepitaxial growth of highly strained structures has been a topic of great fundamental and technological interest as it offers a possibility to fabricate nanoscale islands with high crystaline quality. The change from an initially two-dimensional (2D) to three-dimensional (3D) island like nature when the amount of deposited material exceed a critical value is referred to **Stranski-Krastanow (SK)** growth mode . For nearly five decades, it was assumed that a transition from planar 2D growth to 3D island morphology was accompanied by the formation of defects such as dislocations. However, there was a discovery revealing that the 3D islands formed under suitable growth conditions were coherent and possessed quantum dot (QD) behaviors (Leonard et al., 1993; Marzin et al., 1994; Oshinowo et al., 1994). Since then, there have been intensive efforts towards the understanding of 3D island formation and the utilization of these coherent islands for several applications. The SK growth mode has been observed in a wide range of materials systems, including $Ge_{1-x}Si_x/Si$ (Mo et al., 1990), $In_xGa_{1-x}As/GaAs$ (Moison et al., 1994) and others (Carlsson et al., 1995). For $In_xGa_{1-x}As/GaAs$, where the maximum lattice mismatch is 7%, there are intensive investigations on this material system due to the possibility that it might extend the emission wavelength in to 1.3 – 1.55 μm region, which is important for optical communication system. Several research groups succeed in producing $In_xGa_{1-x}As/GaAs$ laser, which exhibited low threshold current density (Eliseev et al., 2001, Grundman et al., 2000). Since the QDs used for device applications need to have uniform size distribution, high density, and few dislocations, studies on the effects of growth parameters on the island formation must be intensively investigated.

Even though there are many experimental results have been reported in literatures about the SK growth in several material systems, there exists of a not-yet-understood common mechanism governing this growth process. Several theoretical groups keep trying to provide the generic and applicable models, which are responsible for the growth mechanism in a wide class of materials (Daruka and Barbá

si, 1998; Dobbs et al., 1997; Schuckin et al., 1995). There are 2 main approaches which are widely used to explain the mechanisms of QD formation and natural size distribution: thermodynamics and kinetics concepts. However, the thermodynamics equilibrium hypothesis allows only the consideration of self-assembled average parameters, thus unable to provide the understanding of the kinetic effects which play a major role in SK growth mode (Dobbs et al., 1997). Hence, the experimental results in this dissertation will be qualitatively described mainly in kinetics approach.

Generally, the dependence of the QDs structural properties on the growth parameters is studied by the investigation of freestanding QDs on substrate surface. For the QDs to be used in an optoelectronics device, they must be embedded in a confining layer. Because embedding itself can alter the structure of the QDs, changes in the overgrowth parameters can be used to influence the properties of the buried layer. Thus, the understanding of the overgrowth process is also an essential issue to determine the properties of the nanostructures and to realize new devices. There are several research groups that report the drastic evolution of QDs shape during the overgrowth process (Garcia et al., 1997; Sutter and Lagally, 1998; Joyce et al., 2001). Furthermore, the partially capped QDs show different optical and electrical properties comparing to the buried QDs (Kamiya et al., 1998; Saito et al., 1998, Lorke et al., 2000). However, this issue is still controversial and is of far less interest since this process involves complex kinetic aspects, which are rather complicate to treat for semiconductor systems. Hence, one main part of this research is to thoroughly investigate and provide a qualitative understanding of the overgrowth process of InAs QDs grown on GaAs substrate.

Not only the self-assembled QDs grown by SK growth mode are widely of interest as a potential pathway to tune the properties of material and its simple way of fabrication, but also the controllable long range spatial ordering of QDs are required thorough investigation for photonics and electronics devices. It is widely known that the surface strain field modulation from the buried islands plays a controlling role for the islands nucleation in the next layer as has been observed in the vertical alignment characteristic of the closely stack QDs (Ledentsov et al., 1996; Heidemeyer et al., 2002). However, the lateral spatial ordering is a rather more complicated issue. The closely space of QDs group are ideally suitable for the quantum computing device fabrication, for example, the switching of spin-spin interaction of electrons localized in two closely spaced QDs was proposed to act as a quantum gate (Burkard et al.;

2002). For an experimental realization, the use of vertically self-aligned InAs QDs was suggested. In such a quantum gate a controlled tuning of the QD potential profiles, especially the tunnel barrier, is desirable and could be realized by the application of an electric field generated by gate electrodes. The ultimate goal would be to selectively address different parts of the QDs with different gate electrodes to have perfect control over the electronic structure of the QD configuration. However, from a technological point of view, the fabrication of gate electrodes in a vertical QD arrangement seems rather ambitious, mainly because the electrodes need to be attached to the side of an etched mesa that includes the QDs (Austing et al., 1998). There are several attempts, which succeed to create the lateral ordering of the self-assembled QDs by the combination of prepatterning substrate and self-assembled growths (Jin et al., 1997; Lee et al., 2000; Schmidt et al., 2002). Even though there are several successes reported, the realization process of lateral ordering of SK QDs is still a complicated, contaminated and time-consuming process. Moreover, the size of the prepatterning substrate is also limited by the resolution of the lithographic equipment. Schuler et al. (1998) discovered that the strain modulation from the buried InAs QDs perturbed the GaAs etching rate of GaAs cap layer when $AsBr_3$ was supplied on to GaAs surface, providing the realization of 10-15 nm holes on GaAs cap. In this work, the holes were intentionally used as a pattern to order lateral position of self-assembled QDs. The combination of etching and growth functions in the same molecule beam epitaxy (MBE) system offers considerable advantages for *in situ* processing such as allowing instantaneous switching between atomically precise etching and growth process under contamination-free atmosphere. The hole template created by this technique is therefore clean, requires no prepatterning process, and has nano-sized resolution (Schuler et al., 1998; Kiravittaya et al. 2002; Kiravittaya et al. 2003) known as **self-assembled nanoholes**. By depositing InAs on to the nanoholes template, the group of lateral closely spaced QDs naturally form around the nanohole edge. In the following, these groups of closely spaced QDs will be referred as **lateral QD molecules**, as has been done in the literature (Schedelbeck et al., 1997; Deng and Krishnamurthy, 1998; Schmidt et al.; 2002).

In summary, this research works can be divided into two main parts. First part is dealing with the investigation of the growth and the overgrowth of InAs/GaAs self-assembled QDs with the qualitative model to capture the mechanism of structural evolution during the overgrowth process. Second part is the fabrication process to

create the nanoholes and QDs molecule by the combination of $AsBr_3$ *in situ* etching and strain modulation in GaAs cap layer.

The dissertation is organized as follows: Chapter 2 gives experimental details including fabrication systems, sample details and characterization process. Chapter 3 presents the basic concepts of self-assembled QD structure. The experimental results dealing with the structural and optical properties of InAs/GaAs QDs depending on growth conditions such as the amount of deposition, growth rate and growth temperature are given in chapter 4. In chapter 5, the overgrowth process of InAs QDs with GaAs and $In_xGa_{1-x}As$ are thoroughly investigated. The chemical potential model is applied to qualitatively explain the observed surface evolution during the overgrowth process. The PL investigation of the InAs QDs in different matrixes is also presented. Chapter 6 provides the details of nanohole fabrication process, which utilizes the combination of the strain modulation in GaAs cap layer and *in situ* etching process. Systematic investigation of the nanohole formation is presented in this chapter. Chapter 7 gives the details of the QDs molecule realization by depositing InAs onto the nanohole template under different growth conditions. In this chapter, the qualitative model of QD molecules formation is proposed. Finally, chapter 8 is the conclusion of this work.

CHAPTER 2

Experimental Details

This chapter gives the experimental details, which have been done in this research work. This chapter is divided into three main parts: fabrication systems, sample details, and sample characterizations.

2.1 Fabrication systems

This section provides information about i) molecular beam epitaxy (MBE) machine, ii) reflection high energy electron diffraction (RHEED) system, which is used for calibrating substrate temperature, growth rate and etching rate, and iii) the $AsBr_3$ *in situ* etching system and its basic mechanism.

2.1.1 Molecular Beam Epitaxy

All experimented samples are grown in a modified RIBER 32P solid source MBE machine integrating with an $AsBr_3$ *in situ* etching gas system. The MBE system consists of 3 chambers: preparation chamber, transfer chamber and growth chamber. These 3 chambers are separated by isolation gate valves and the samples are transferred from chamber to chamber by magnetic arm. In preparation and transfer chambers, there are heaters used for a heat treatment process (called preheat) of the substrate in suitable conditions, which is an important step for MBE growth. The preparation chamber is vacuumed by a cryopump, while the transfer chamber is equipped with a cryopump, a turbo-molecular pump, a titanium sublimation pump, and an ion pump. The pressure is measured by ion-gauge. A propose of preheat process is to remove contaminated substance, mainly water (H_2O), from the substrate surface. After the preheat process, the sample is transferred to the manipulator in the growth chamber via magnetic arm. A schematic drawing of the modified MBE growth chamber is shown in figure 2.1. The building blocks of this growth chamber consists of material source cells, substrate heater, monitoring equipment (for

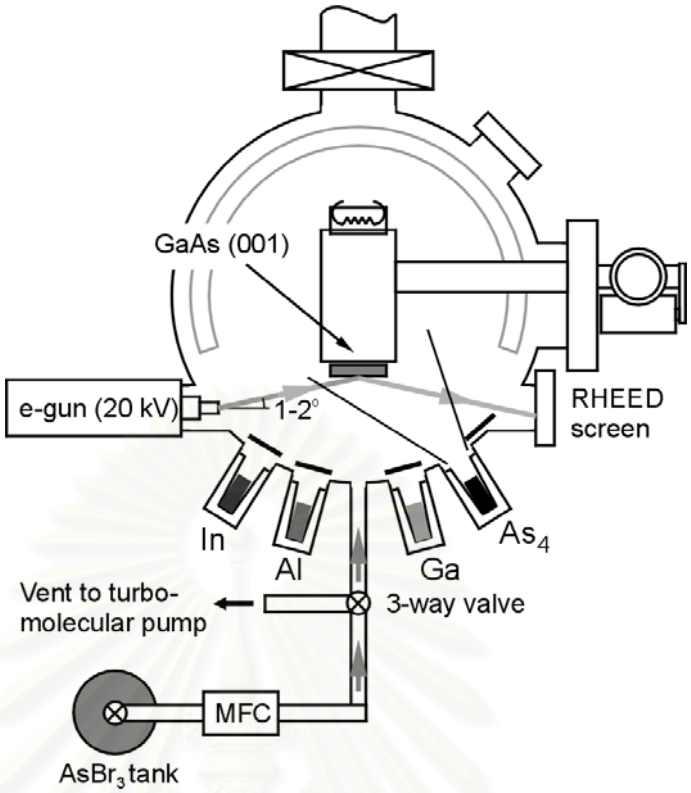

Figure 2.1 Schematic drawing of the III-V MBE growth chamber modified with $AsBr_3$ *in situ* etching gas system.

temperature, pressure, particle and surface analysis), *in situ* etching system, and vacuum system. The materials used in this experiment are In, Ga, Al, and As_4, which are contained in pyrolytic boron nitride (PBN) crucibles, installed in separated effusion cells. The temperatures were measured by W-Re with 5% or 26% Re thermocouples and controlled by computer via controller card (EUROTHERM^{TM}). The substrate is continuously rotated during the epitaxy to provide uniform flux profile on substrate surface. The beam flux is mechanically controlled by tantalum shutter in front of each cell. There are two ionization gauges in this chamber: one, located at equivalent substrate position behind the substrate heater, is for beam flux measurement and the other, which is installed in front of the ion pump, is for background pressure measurement. The quadruple mass spectroscopy is used for the particles analysis in the growth chamber. The equipment for RHEED investigation consists of a 20-kV electron gun, a fluorescent screen, a CCD camera, and a computer. The RHEED diffraction pattern generated by the sample surface is displayed on a phosphor screen and captured by CCD camera. The $AsBr_3$ *in situ*

etching gas system is connected to the growth chamber via a port at the middle of cell flange. The tube is generally vacuumed by a turbo-molecular pump and is heated about 80°C to avoid the condensation of etching gas. The flow rate of the etching gas is controlled by a mass flow controller (MFC) (MKS Instrument type 250D).

2.1.2 Reflection high-energy electron diffraction

Reflection high-energy electron diffraction system is important equipment for the MBE growth since it provides the information of surface quality and the indirect information of substrate temperature related to the surface reconstruction (Alexeev et al., 1996; Farrell and Palstrøm, 1990). Moreover, the RHEED intensity oscillation during material deposition reveals the growth rate of the deposited material and the change of the RHEED pattern indicate the growth modes during the epitaxy. The left-hand side of figure 2.2 illustrates the experiment geometry of RHEED showing the electron beam incident on substrate surface with small impinging angle in the range of 1-2°. The short de Brogile wavelength of incident high-energy electron allows a shallow penetration depth into the substrate, therefore, the diffraction pattern provides an information of a few outermost atomic layers of the surface. We can simply describe that the RHEED pattern is the reciprocal lattice representation of the

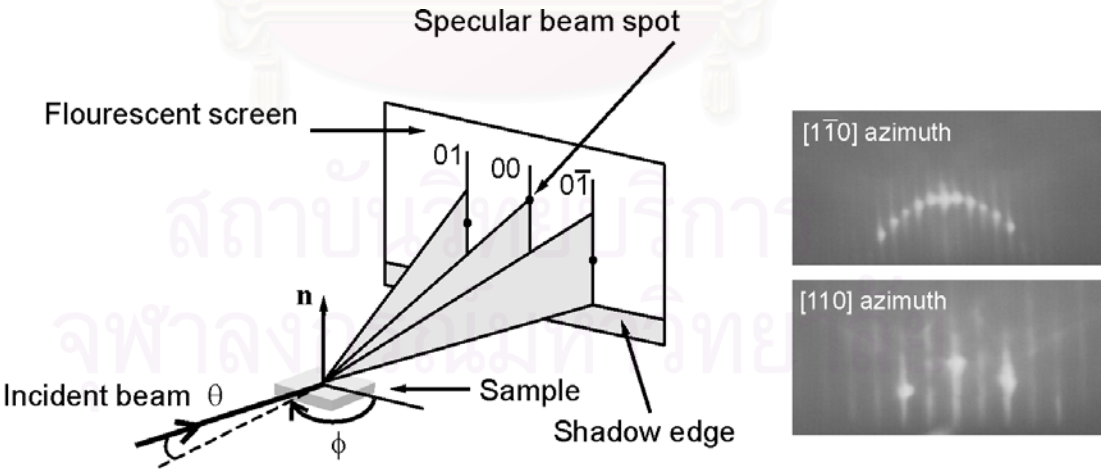

Figure 2.2 Schematic diagram of RHEED geometry showing the incident electron beam at an angle θ to the surface plane (Herman and Sitter, 1989). The right part shows diffraction pattern from the GaAs (001) (2×4) surface, in the [1-10] and [110] azimuths.

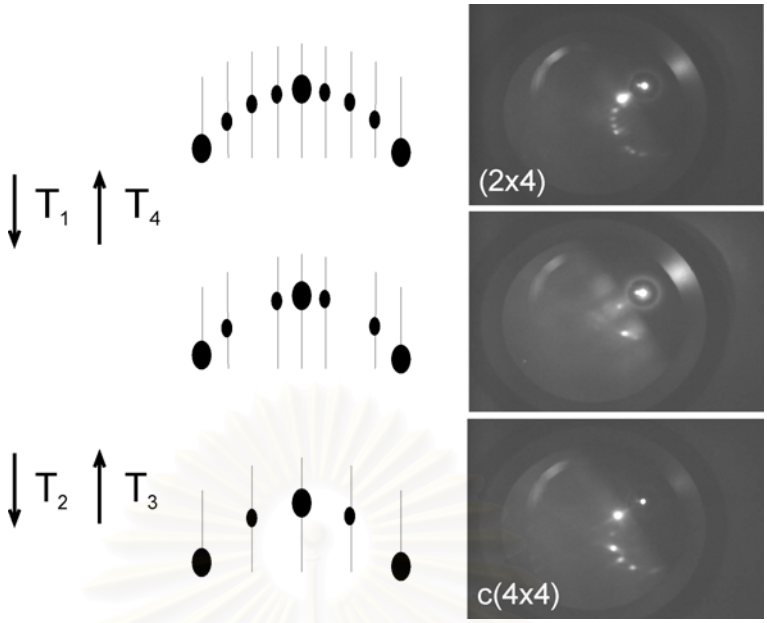

Figure 2.3 Schematic diagram of RHEED pattern transition in [-110] azimuth of (001) GaAs substrate during the temperature calibration process. The substrate temperature was decreased and increased with the rate of 10°C/min, and transition temperatures T_1, T_2, T_3, and T_4 were recorded and the average temperature of these four temperature was defined as 500°C

sample surface, which reflects the surface nature in atomic scale (Herman and Sitter, 1989). The right-hand side of figure 2.2 shows the streaky RHEED patterns of GaAs (001) (2×4) surface under As-rich atmosphere in the [1-10] and [110] azimuth, revealing the atomically flat surface. In this experiment, the change of RHEED pattern with temperature is used for temperature calibration, and the RHEED intensity oscillation is for growth rate calibration, which will be described in the following section.

Temperature calibration

Since the temperature read from thermocouple is not the real temperature of substrate surface, a more reliable method is needed to control the growth temperature. Temperature causing a surface reconstruction transition is a reliable temperature to be used as a reference point for the growth process. In our experiment, the (001) GaAs substrate temperature was decreased at a rate of 10°C/min until RHEED pattern

change from (2×4) to *c*(4×4) as shown in figure 2.3, and then the substrate temperature was increased again to record the transition temperature T_1, T_2, T_3, and T_4. The average temperature of T_1, T_2, T_3, and T_4 is defined as 500°C. The calibration process has been done under As-rich atmosphere of 6-8×10^{-6} mbar.

Growth rate calibration

The growth dynamic of MBE growth can be explored by monitoring temporal variation in the intensity of RHEED pattern. The maximum reflectivity of the incident beam occurs with the complete or smooth surface while the minimum is due to the intermediate stage where the growing layer is the fraction of surface coverage. Hence, in a layer-by-layer growth mode, the full coverage and fractional coverage occurs in cycles and causes the oscillation of RHEED intensity. The period of the oscillation signal corresponds to the growth of 1 ML. In this experiment, the growth rates of GaAs and AlAs are calibrated by this oscillating signal.

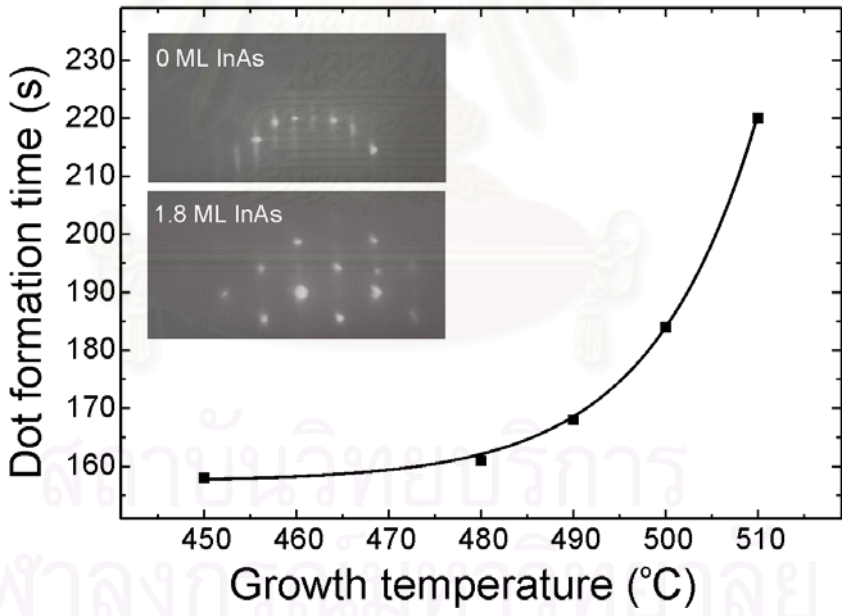

Figure 2.4 The dependence of QD formation time on the growth temperature. At high growth temperature the QDs are hardly formed due to thermal desorption of InAs. Inset shows the RHEED patterns at 500°C (a) before InAs deposition and (b) after 1.8 ML of InAs deposition in [1-10] azimuths.

For the InAs, which is lattice mismatched with GaAs substrate, we can also use RHEED intensity oscillation by adding Ga during InAs deposition and calculate back InAs growth rate from InGaAs RHEED intensity oscillation. In this work, we use QD formation time for the InAs growth rate calibration. The RHEED pattern transition from streaky to spotty pattern as depicted in the inset of figure 2.4 during the growth of InAs from 2D to 3D was defined as 1.8 ML InAs deposition. The growth rate can be calibrated by recording the dot formation time. However, due to the low sticking coefficient of In adatoms, it can easily desorb from GaAs substrate at high temperature. By this fact, the calibration process should be done at the temperature range where the In desorption is negligible (below 450°C). At the substrate temperature higher than 520°C and low In growth rate, the QDs hardly form due to the thermal desorption. Figure 2.4 reveals that the dot formation time increases with the growth temperature (The In growth rate is set at 0.01 ML/s).

2.1.3 $AsBr_3$ *in situ* etching system

This section deals with $AsBr_3$ *in situ* etching system which explains the $AsBr_3$ etching gas properties, etching mechanism, material selectivity, and *in situ* etching process in this experiment.

$AsBr_3$ etching gas properties

There are several demonstrations of chemical etching process of GaAs or InP by using group V-halide such as $AsCl_3$, PCl_3, and $AsBr_3$ under ultra high vacuum system (Tsang et al., 1993; Zhang et al., 1997). In this system, the $AsBr_3$ was selected to be the etching gas due to the lower electron affinity of the Br comparing to F and Cl, hence less chemical reaction against MBE system is expected (Schuler et al., 2000). Moreover, the melting point of $AsBr_3$ etching gas is 32.8°C which is above room temperature, thus this gas is less critical to handle and for this experiment the source of the etching gas is kept below room temperature. The vapor pressure of $AsBr_3$ etching gas at 20°C is sufficient to introduce the etchant into the system through a mass flow controller without pre cracking process and carrier gas. In addition, the other advantage of using $AsBr_3$ gas is that there is no need to supply additional As

flux during the etching process since $AsBr_3$ can provide arsenic overpressure which can stabilize GaAs surface (Ritz et al., 1997).

$AsBr_3$ etching mechanism

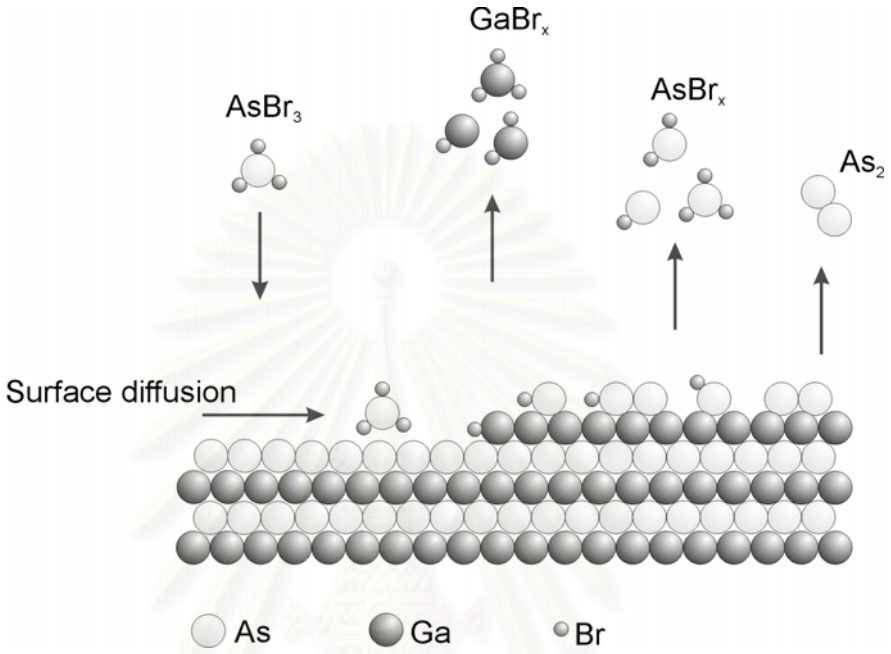

Figure 2.5 Schematic illustration of the $AsBr_3$ etching mechanism of the GaAs surface (Schuler et al., 2000).

When $AsBr_3$ molecules impinge and migrate on the GaAs surface, the $GaBr_x$ molecule form due to their higher binding energy compared to $AsBr_x$. The etching process performs by the $GaBr_x$ desorption from GaAs surface. Zhang et al. (1997) discovered that the etching rate limit step is due to the desorption or the formation of $GaBr_x$, not the decomposition of $AsBr_3$. The schematic illustration of $AsBr_3$ etching process is shown in figure 2.5. As the etching process occurs on a layer-by-layer basis, the etching rate can be calibrated by the RHEED intensity oscillation. Figure 2.6 reveals that the etching process can be divided into 2 different regions. At low substrate temperatures, the etching rate increases with substrate temperature and was named a *reaction rate-limited region*. At higher substrate temperature, the constant etching rate indicates a *supply rate-limited region* (Ritz et al, 1997; Schuler et al.; 2000). Moreover the etching rate shows the dependency on the flow rate. The inset in

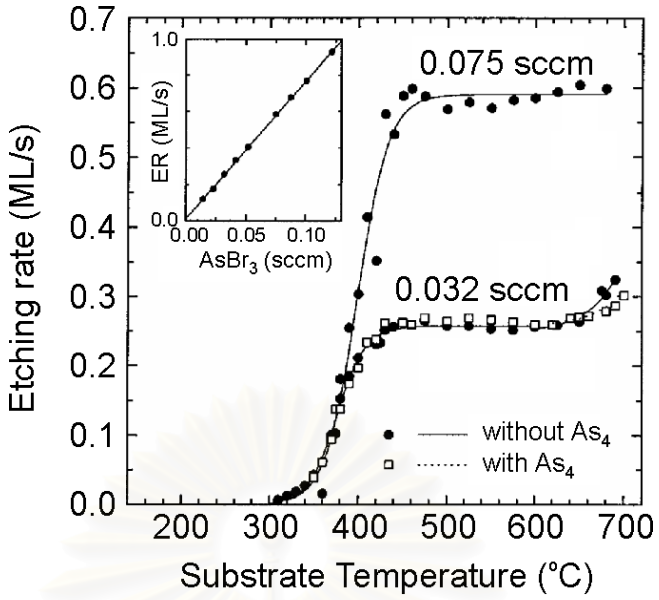

Figure 2.6 The etching rate of GaAs (001) versus substrate temperature for two different $AsBr_3$ flow rates. For 0.032 sccm of $AsBr_3$, the etching rate with and without concomitant As flux (Ritz et al., 1997).

this figure shows that the etching rate linearly increases with the flow rate of the etching gas. One interesting result is that a concomitant supply of As flux to maintain As-rich atmosphere has little effect on the etching rate since $AsBr_3$ can provide enough As concentration on GaAs surface.

In addition, Kaneko et al. (1995) discovered the decaying of RHEED intensity and the disappearing of the oscillation at the intermediate temperature and reappearing at lower substrate temperatures.

Material selectivity

To determine the etching rate dependence on the material, the RHEED intensity oscillation during the supply of etching gas on to the planar (100) substrates of binary compounds InAs, GaAs and AlAs was recorded. The etching rates as a function of substrate temperature of different materials are plotted in figure 2.7 (Schuler et al., 2000). The etching process shows two different etching mechanism in each materials but the temperature which causes the transition from the reaction rate-limited to the supply rate-limited region is different. The etching gas can etch InAs at the highest etching rate and AlAs at the lowest one.

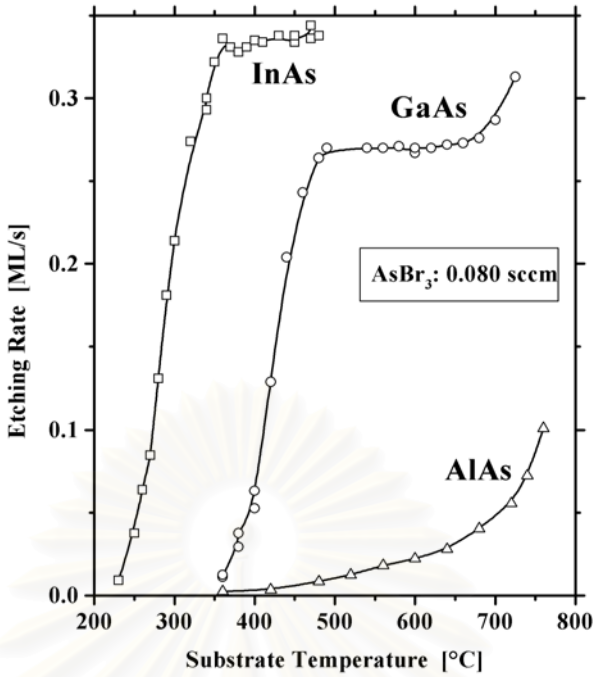

Figure 2.7 Temperature dependent etching rate for binaries GaAs, InAs and AlAs (001) measured by RHEED intensity oscillations (Schuler et al., 2000).

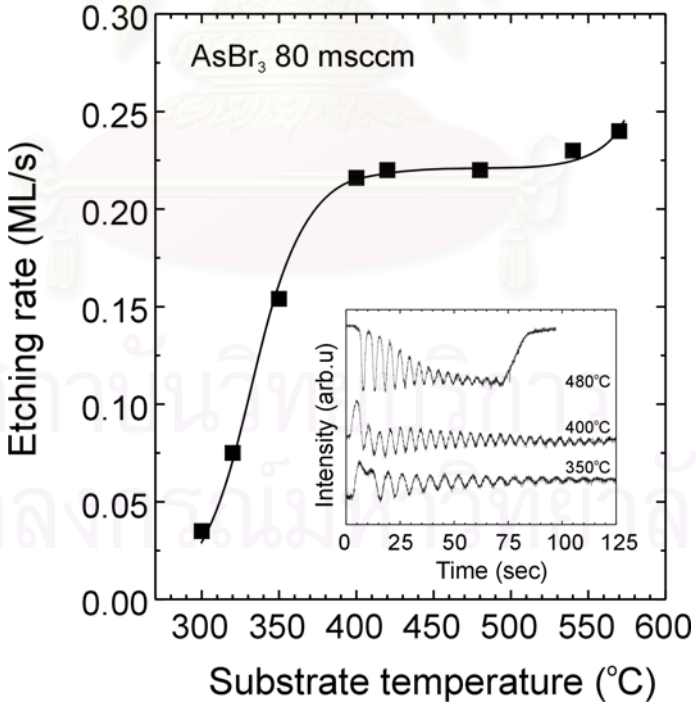

Figure 2.8 Temperature dependent etching rate for GaAs (001) measured by RHEED intensity oscillations. The inset shows the RHEED intensity oscillation during the etching process at different temperature.

Etching conditions

In this experiment, the calibration curve of the $AsBr_3$ etching gas as a function of the substrate temperature is shown in figure 2.9. The flow rate is fixed at 80 msccm throughout this work, which is equivalent to the etching rate of 0.23 ML/s. The substrate temperature during the etching process is kept at 500°C, which is in the supply rate limited region. The additional As_4 flux is supplied during the etching process.

2.2 Sample details

Sample preparation

All the investigated samples were grown on epi-ready semi-insulating (001) GaAs wafer. The sample was glued on an unpolished 3" Si wafer by using indium glue and was mounted into a molybdenum block. The preheat temperature in the introduction chamber or the transfer chamber is set at 300°C for more than 30 min. Before the buffer growth, the surface oxide layer was removed at 630°C for 10 min, under As_4 pressure of ~$6\text{-}8\times10^{-6}$ mbar, then 300-nm thick GaAs buffer layer was grown to flatten the surface. The temperature calibration as presented in section 2.1.2 was performed, followed by the growth of 100 nm of GaAs and the desired structure.

Sample outline

After a 0.4-μm GaAs buffer layer was grown at 610°C with a growth rate of 0.6 ML/s., a 20-nm thick $Al_{0.4}Ga_{0.6}As$ and a 20-nm thick GaAs layers were grown and the substrate temperature was decreased to 500°C, followed by the desired structures such as the QDs, the nanoholes, and the QD molecules. For photoluminescence (PL) investigation, the structure was covered by a 100-nm thick GaAs, a 20-nm thick $Al_{0.4}Ga_{0.6}As$, and a 20-nm thick GaAs layers at 500°C. The two 20-nm $Al_{0.4}Ga_{0.6}As$ layers were grown to enhanced carrier confinement. Finally, a similar structure was grown on the surface and the substrate temperature was cooled down immediately by turning off the heater power supply to freeze the examined structures for *ex situ* AFM characterization. The schematic of sample structure grown for this work is shown in figure 2.9.

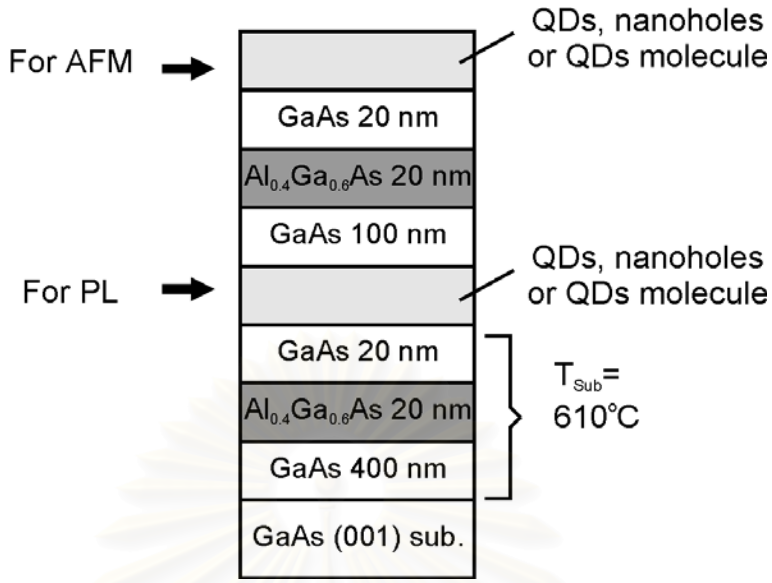

Figure 2.9 Schematic diagram of the sample structure grown in this experiment.

2.3 Sample characterization

The structural and optical properties of the investigated samples are characterized by atomic force microscopy (AFM) and photoluminescence (PL) measurements, respectively. This section gives the details of the analytical tool which are used in this experiment.

Atomic Force Microscopy (AFM)

For surface analysis atomic force microscopy (AFM) is performed by using a DIGITAL INSTRUMENT Nanoscope IIIa in the tapping mode. The scan rate is ~ 1.2 Hz and the scan size is usually 2×2 μm^2. The number of data per scan line is 512, therefore the lateral resolution of all AFM images is about 4 nm. The vertical resolution of this measurement is usually in the subnanometer range.

Photoluminescence (PL) measurement

The samples were excited by the 488-nm line of an Ar^+ laser (SPECTRA PHYSICS SERIES 2000). The laser beam was chopped and focused onto the sample by a 33-cm focal length lens. An 8-cm focal length and a 40-cm focal length lens are used to collect the PL signal. The light signal was resolved by a 1-m monochromator

(JOBIN YVON THR1000). Typically, the entrance and exit slits' widths are 0.5 mm. A high-pass filter (RG665) is used to filter out the visible-light noise and the reflected laser beam signal. The resolved light signal is detected by a liquid-N_2-cooled Ge detector (NORTHCOAST EO-817L). The chopper and the lock-in amplifier (EG&G 5207) are used to enhance the signal by the standard lock-in technique.

Chapter 3

Self assembled nanostructures

As predicted by Arakawa and Sakaki (1982) that multi-dimensional quantum well such as quantum wire and quantum dots (QDs) are expected to further improve the characteristic of the optical device due to their reduced dimension, leading the change of electron density of state. There are great efforts to create a lateral confinement potentials of the quantum well to obtain such low dimensional structure such as using e-beam lithography, photolithography, or growth on pre-pattern substrate. However, these artificial processes are not only time consuming and complicating processes but also suffer from the low crystal quality of created structure. A breakthrough occurred when the islands which spontaneous form during the deposition of highly strain material were discovered that they are dislocation-free and show zero dimensional confinement properties. This leads many research groups both experimental and theoretical deeply to investigate the self-assembled islands and try to utilize the novel properties from this kind of QDs.

In this research work, the self-assembled QDs grown by Stranski Krastanow growth mode are experimentally investigated. Therefore, the introduction of the energy level and density of states depend of the dimension of the nanostructures are briefly introduced which will be useful for the interpretation of photoluminescence investigation of QD structure. To understand the growth process, the mechanism which leads the island formation are qualitatively presented in both thermodynamic and kinetic approaches. Since the strain field is a major parameter which induces the QD formation and determines the structural evolution of the QD, the roles strain distribution are detail discussed both on the freestanding and buried QDs. The last section provides the information of the material system which we used to create the self-assembled QDs.

3.1 Low dimensional nanostructures

When the size of the crystal is reduced into the order of de Broglie wavelength in one direction and the crystal is surrounded by other crystals acting as potential barriers, the freedom of electron movement is lost in that direction. The de Broglie wavelength, $\lambda_{\text{de Broglie}}$, is a function of a carrier effective mass, m_{eff}, and temperature, T (Bimberg et al., 1999)

$$\lambda_{\text{deBroglie}} = \frac{h}{p} = \frac{h}{\sqrt{3m_{\text{eff}}k_B T}} \tag{3.1}$$

where h is Planck's constant, p is carrier momentum, and k_B is Boltzmann's constant. As schematically illustrated in figure 3.1, the electrons are confined in one direction (z) and can move freely in two directions (x-y) in quantum well structure, while those in quantum wire can move only in x directions. In quantum dot, electrons are completely localized. The confinement results in the quantization of the electron energy and in the variations of the electron density of states.

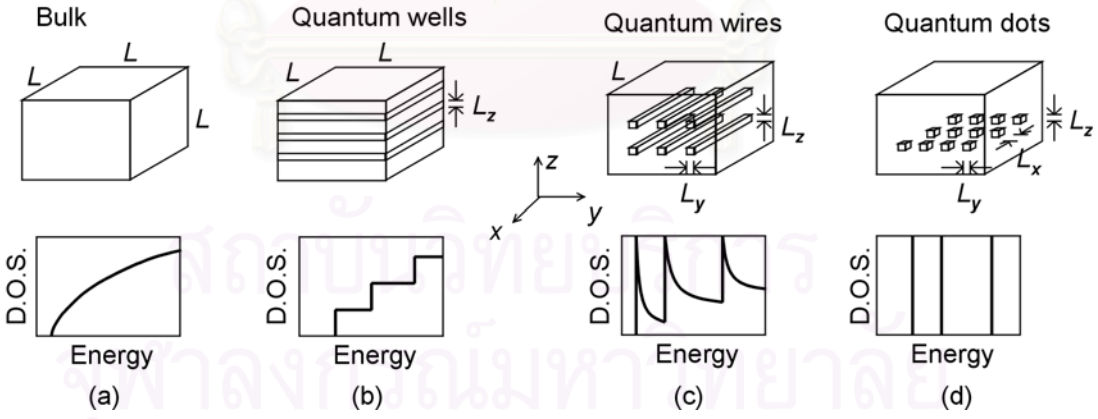

Figure 3.1 Schematic views and graphs of (a) bulk, (b) quantum wells, (c) quantum wires, and (d) QD and their density of states (D.O.S.). (Sugawara, 1999).

In semiconductor quantum wells, an effective-mass approximation is widely used for the quantized energy levels calculation as a function of the well width (Bastard and Brum, 1986). The main assumption of the effective-mass approximation is that the envelope wave function does not significantly vary in the unit cell with a length scale of subnanometers, therefore this assumption is valid in all low-dimensional nanostructures. Assuming parabolic band dispersion, band-edge electron states of semiconductors can be described by Schrödinger-like equation as

$$\left[-\frac{\hbar^2}{2m^*}\nabla^2 + V(\mathbf{r})\right]F(\mathbf{r}) = E\,F(\mathbf{r}) \tag{3.2}$$

Here, m^* is the effective mass; $\hbar$ is the reduced Planck's constant; $\mathbf{r} = (x,y,z)$ is the carrier position vector; $V(\mathbf{r})$ is the confinement potential due to band offset. $F(\mathbf{r})$ is the envelope wave function; and E is the carrier energy.

From eq. (3.2), by assuming the barrier potentials with *infinite height*, the carrier energy E and density of states per unit volume in case of bulk, quantum well (QW), quantum wire (QWR) and QD can be written as follow (Sugawara, M. 1999.)

Bulk materials

$$E_{\text{bulk}} = E(\mathbf{k}) = \frac{\hbar^2 k^2}{2m^*} \tag{3.3}$$

$$D_{\text{bulk}}(E) = \frac{1}{2\pi^2}\left(\frac{2m^*}{\hbar^2}\right)^{3/2} E^{1/2} \tag{3.4}$$

where $\mathbf{k} = (k_x,k_y,k_z)$ is the wave vector of carriers and $k^2 = k_x^2 + k_y^2 + k_z^2$

Quantum well (QW)

Assuming that the confinement potential barrier for the square QW has infinite height, we obtain (Sugawara, M. 1999.)

$$E_{\mathrm{QW}} = E(\mathbf{k}) = \frac{\hbar^2 k_{//}^{\ 2}}{2m^*} + E_{n,z} = \frac{\hbar^2}{2m^*}\left[k_{//}^{\ 2} + \left(\frac{n_z \pi}{L_z}\right)^2 \right] \tag{3.5}$$

$$D_{\mathrm{QW}}(E) = \frac{m^*}{\pi \hbar^2 L_{QW}} \sum_{n_z} \Theta(E - E_{n_z}) \tag{3.6}$$

where $k_{//}^{\ 2} = k_x^2 + k_y^2$, Θ is the Heaviside's unit step function, n_z=1,2,3,…., and L_{QW} is the sum of the well and barrier regime thickness. From eq. 3.5, the minimum energy and the energy separation between each quantized state increase as the well width decreases.

Quantum wires

Assuming that the confinement potential barrier for the square QWires has infinite height, we get (Sugawara, M. 1999.)

$$E_{\mathrm{QWR}} = E(\mathbf{k}) = \frac{\hbar^2 k_{\perp}^{\ 2}}{2m^*} + E_{n_y} + E_{n_z} = \frac{\hbar^2}{2m^*}\left[k_{\perp}^{\ 2} + \left(\frac{n_y \pi}{L_y}\right)^2 + \left(\frac{n_z \pi}{L_z}\right)^2 \right] \tag{3.7}$$

$$D_{\mathrm{QWR}}(E) = \frac{N_{wi}}{\pi} \frac{\sqrt{2m^*}}{\hbar} \sum_{n_y,\, n_z} \frac{1}{\sqrt{E - E_{n_y} - E_{n_z}}} \tag{3.8}$$

where $k_{\perp}^{\ 2} = k_x^2$, n_y, n_z=1,2,3,…., and N_{wi} is the area density of the quantum wires (the number of quantum wires divided by the quantum-wire region area in the *y*-*z* plane),

Quantum dot

Assuming that the infinite confinement potential barrier in all direction, we get (Sugawara, M. 1999.)

$$E_{\mathrm{QD}} = E_{n_x} + E_{n_y} + E_{n_z} = \frac{\hbar^2}{2m^*}\left[\left(\frac{n_x \pi}{L_x}\right)^2 + \left(\frac{n_y \pi}{L_y}\right)^2 + \left(\frac{n_z \pi}{L_z}\right)^2 \right] \tag{3.9}$$

$$D_{\mathrm{QD}}(E) = 2N_D \sum_{n_x, n_y, n_z} \delta(E - E_{n_x} - E_{n_y} - E_{n_z}) \tag{3.10}$$

where δ is the delta function, and N_D is the volume density of QD.

The change of density of states for the low-dimensional nanostructures (Figure 3.1) considerably affects the fundamental properties of the devices, which use these nanostructures as an active layer (Arakawa and Sakaki, 1982). The electronics properties for QD structure differ drastically from the bulk system due to the discrete energy levels and delta peak density of states, which are in contrast to the continuous spectrum of the bulk. Hence QD structure sometimes was name as *artificial atom*. In case of QD structures, there are several theoretical and experimental proves that semiconductor lasers consisting of QD structures have the lowest threshold current density due to the delta-function-like density of states (Asada et al., 1986).

3.2 Growth of self-assembled quantum dots

Since there is particular interest to self assembled QDs for device applications due to their zero dimensional confinement nature and dislocation free structure, the basic study of the self organized process is required. To ensure the fabrication process to realize the high quality structure, one has to master the way to control the spontaneous formation of the arrays of island. To achieve this goal, the physical mechanism governing the islands formation, their shape, size, size distribution and the relative arrangement on the surface are greatly important. This section therefore briefly introduces the mechanism which is responsible for the formation and growth of self-assembled islands.

3.2.1 MBE growth modes

To define the growth mode which occur during the film deposition, we consider $\Delta\gamma$ which is the change of total energy of a surface before and after deposition:

$$\Delta\gamma = \gamma_F + \gamma_{S/F} - \gamma_S \tag{3.11}$$

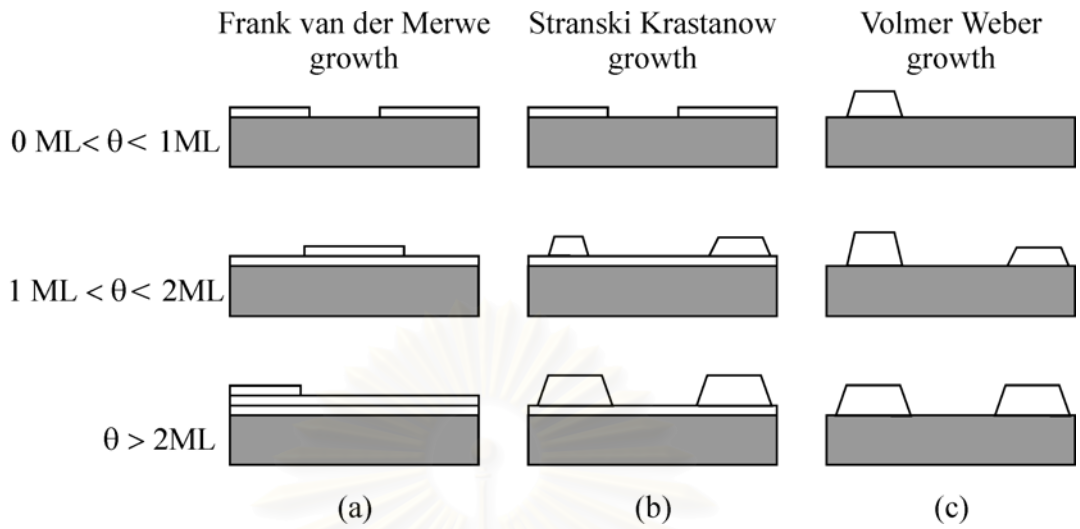

Figure 3.2 Schematic representation of the 3 important growth modes of a film for different coverage (θ) (a) Frank van der Merwe (FM) (b) Stranski Krastanow (SK) and (c) Volmer Weber (VM).(Herman and Sitter (1989)

where γ_S is substrate surface energy, γ_F is film surface energy, and $\gamma_{S/F}$ is interface energy between film and substrate which includes the additional energy arising from the strain between film and substrate.

If $\Delta\gamma < 0$, the deposited material would prefer to cover the substrate surface, then we obtain Frank Van de Merwe growth mode or layer-by-layer growth (Figure 3(a)). In this mode, the interaction between the substrate and deposited atoms is stronger than that between neighboring atoms. In the opposite case, if $\Delta\gamma < 0$, the 3D growth mode as Volmer Weber mode is observed (Figure 3.2(b)), where the interaction between substrate neighboring atoms exceeds the overlayer substrate interactions. In some case the deposited film can grow in layer by layer mode at the early stage of deposition ($\Delta\gamma < 0$). However, due to the strain between the film and substrate increasing with the deposited film thickness, $\Delta\gamma$ becomes less than zero and growth mode changes from 2D-growth mode to 3D-growth mode. The intermediate case was named **Stranski Krastanow** (SK) growth mode.

3.2.2 Stranski Krastanow growth mode

When the strained layer was deposited on to the substrate, in some growth conditions there would be a strong driving force for the material to form islands rather than to form the uniformly strained flat film. In that growth condition, for the first few monolayers, the deposited material will form in to 2D platelets which proceed in layer by layer mode until they merge with each other to complete 2-D epilayer. The accumulated elastic strain energy, *E(el)*, will increase linearly with the deposited volume, according to eq. 3.12 (Seifert et al., 1996)

$$E(el) = \lambda \varepsilon^2 At \tag{3.12}$$

where λ is the elastic modulus, ε is the lattice mismatch, A is the surface area and t is the film thickness. If the system keep 2D growth, the energy will increase till overcome the activation energy of dislocation process. On the other hand, if the growth conditions drive the system to the SK growth, when the strain energy outweigh the surface energy the system has to release the strain energy by change the growth mode from 2D to 3D growth mode, cause the island formation (Slolovitz, 1989).

In general, the theoretical work on self- assembly can be grouped into two classes. First aspect explains the QD formation by using energetic principles and equilibrium thermodynamics (Shchukin et al., 1995; Daruka and Barbasí, 1997). Second, since some properties of QD formation clearly exhibit nonequilibrium features, the dynamic models are invented to explain such a feature (Dobb et al., 1997; Barbasí, 1997). This section will descriptively present the island formation mechanism in both thermodynamic and kinetic approach.

Thermodynamic approach

There is a belief that if the islands were formed on the surface, there would be the driving force towards Oswald ripening, which causes the reduction of island density and widens the size distribution. This idea is in contrast with several experimental results

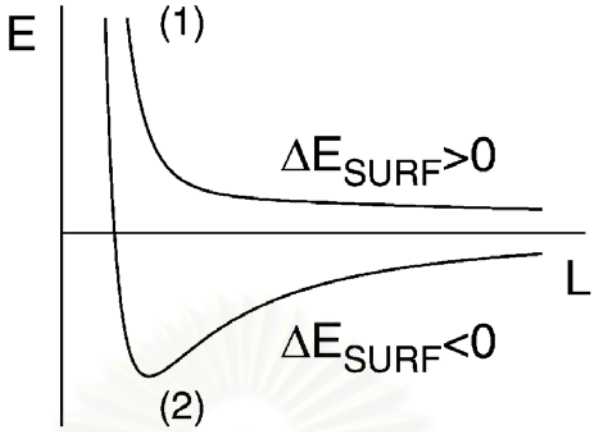

Figure 3.3 Energy per atom versus island size for and array of 3D strained islands. (1) An array of islands exhibits a driving force to Ostwald ripening. (2) an optimum size of the islands exists. (Shchukin et al., 2001)

which present uniform island formation in some growth conditions. Shchuckin et al. (1995) proposed the thermodynamic model which explain the narrow size distribution of islands with an absence of Oswald ripening process by considering the energentics of an array of islands. The total energy change of the system due to the formation of a single island of a size L can be written as a sum of the following distributions (Schucking et al., 2001)

$$\Delta E = -f_1 \lambda L^3 + (\Delta\Gamma)L^2 + f_2 \eta L - f_3 \frac{(\Delta\tau)^2}{\lambda} L \ln \frac{L}{a} \qquad (3.13)$$

The first term is the energy of the elastic relaxation, λ is a characteristic elastic modulus of the material ; the second term is the change of the surface energy of the system; the third term is the short range contribution to the energy of the islands edges, η being the energy per unit length of the edge and the forth term is the energy of the elastic relaxation due to the surface stress discontinuity ($\Delta\tau$) at the edges. a is lattice parameter; f_1 f_2 and f_3 are geometrical factors depending on the island shape. The quantity $\Delta\Gamma$ represents the

energy change due to the appearance of the side facets, the disappearance of a certain area of the wetting layer, the appearance of the interface between the island and the substrate and the strain induce corrections to the surface energies; therefore, $\Delta\Gamma$ can be positive or negative due to an interplay between different contributions. By assuming a fixed islands shape, the energy *E(L)* is given in figure. In case of $\Delta\Gamma > 0$, the formation of a single island from a flat film causes an increasing of the total surface energy and the system has to reduce the energy to the minimum of *E(L)* which locate at $L \to \infty$, as shown in figure 3.3 inducing the ripening process. If $\Delta\Gamma < 0$, the formation of the islands decrease the total surface energy and then cause the minim energy *E(L)* locates at a finite size of island. There is no driving force for the ripening in this case, implying that there exists the stable island array with finite shape. This model is based on the scaling behavior of various contributions to the total energy, leading to a criterion for Oswald ripening process or island formation.

Daruka and Barbasí (1997) proposed the model which can give more understanding of the equilibrium morphology of the system by taking the existence of the wetting layer into account. Therefore neither the thickness of wetting layer nor the total volume of the island are fixed separately. By this model, they can obtain the equilibrium phase diagram of lattice mismatched system as a function of lattice mismatch and the total amount of deposited material. The details of the calculation and the phase diagram are presented by Daruka and Barbasí (1997)

Kinetic approach

The kinetic approach can give an understanding of the island formation and growth as a function of growth parameters such as growth rate, growth temperature and substrate temperature. Several kinetic models of 3D island formation have been proposed. (Chen et al., 1995; Chen and Washburn, 1996; Barabasi, 1997; Dobbs et al.,1997). Such models take the microscopic processes on the crystal surface into account such as deposition, diffusion, attachment to the island and detachment from islands. The mechanism of the QD growth is which described by these models can be divided into 2 processes i.e. island nucleation and growth

Island nucleation

Dobb et al. (1998) formulated a mean-fielded theory for the density of adatoms in 2D and 3D islands and try to explain the island density as a function of growth parameters such as amount of material deposition, growth rate and substrate temperature. The model described the island nucleation by assuming that after the wetting layer has already formed, the mobile adatoms would migrate on the surface and collide with each other to form 2-D island, which can be stable or break-up into adatoms again. The 2D-islands with the size beyond critical size are able to grow by capture migrating adatoms atoms and have a potential to transform to 3D islands. From the model, the island density increases rapidly at the early stage of the deposition and then saturates. Further depositing material does not significantly effect to the island density but leads to the growth of the island size. As a function of the growth rate and substrate temperature, the island density appears to be controlled by the 2D island nucleation that the density is an increasing function of the growth rate and a decreasing function of temperature. This also can be simply explained by the classical nucleation theory which is suggested by Seifert et al. (1996).

Island growth

The model presented by Dobb et al.(1998) can provide an understanding during an initial stage of island formation but is not sufficient to explain the narrow size distribution of island array. Chen and Wasburn (1996) proposed the model which can explain the distribution of the island on the surface by the gradient of chemical potential which is modified by the strain induced by the islands. When the 2D-islands reach critical size which posses high strain energy, the island has to release strain by transition from 2D to 3D islands. At the early stage of 3D-island formation, the islands show broader size distribution. When 3D islands are formed, the surface strain would be modified by the strain relaxation of the islands on the surface. The surface strain can be approximated by using an analytic solution of the stress field in 2D mound on a strained semi-infinite substrate as a contour plot of absolute value of ε_{xx} and a surface tangential strain ε_s along the system surface shown in figure 3.3 (Chen and Wasburn (1996)). The

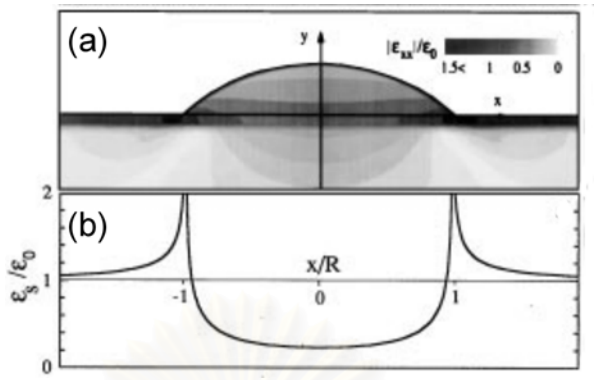

Figure 3.4 (a) A contour diagram showing strain ε_{xx} in the island (b) the variation of the surface strain ε_s along the system surface. (Chen and Washburn, 1996)

partially relaxation at the top of the island induce an extra strain in the substrate and increasing the strain in the wetting layer. The results from the calculation correspond to the strain energy distribution calculate by an atomistic model presented by Barabási (1997) or by a finite element method reported by Spencer and Tersoff (2001) that there exist the high strain energy at the island edge due to the strain relaxation of the strain material. Since the net adatoms current on substrate surface caused by the gradient of chemical potential, chemical potential modified by the surface strain biases a random motions of adatoms, generating the net current deposited adatoms from the high strain sites to the lower one.

Chen *et al* (1996) suggested that the 3D islands will grow by the accumulation of adatoms, which are directly deposited onto the island surface and the attachment of adatoms that deposited on the wetting layer surface with in the critical distance from the island edge. These adatoms are supposed to overcome the energy barrier to attach the islands. Their calculation results reveal that the small island rapidly increase in size due to the deposited adatoms. However, the attached adatoms to the islands tend to increase the strain concentration at the island edge, then increase the barrier for the migrating adatoms to overcome to attach the islands. This leads the slower growth rate of the larger islands. In additions, Barabási (1997) proposed that for the large islands, the strain energy at the island edge becomes comparable to the bonding energy of the edge atoms,

enhancing the detachment of the atoms at the island edge and consequently causing gradual island dissolution. The two mechanisms lead the size uniformity. Further material deposition cause the growth of the exist islands. As a consequence, the high strain energy occurs at the edge of the larger island. The formation of the misfit dislocation at the island edge is one way to relieve the strain energy of the system, the energy barrier would decrease and enhance the directional migration of adatoms to this island. The process permits the resumption of the island growth to reach the second critical size.

We can summarize the process of the QDs formation by the schematic illustration shown in figure 3.4. When the latticed mismatched material was deposited on to the substrate, the 2D platelets formed (figure 3.4(a)) and became the wetting layer (figure 3.4(b)). Further deposition, the strain energy in the wetting layer increase until overcome the surface energy, inducing 2D to 3D island transition (figure 3.4(c)). The smaller islands posses the lower energy barrier due to the less strain energy, leading the directional migration of the deposited adatoms from the larger to the smaller island

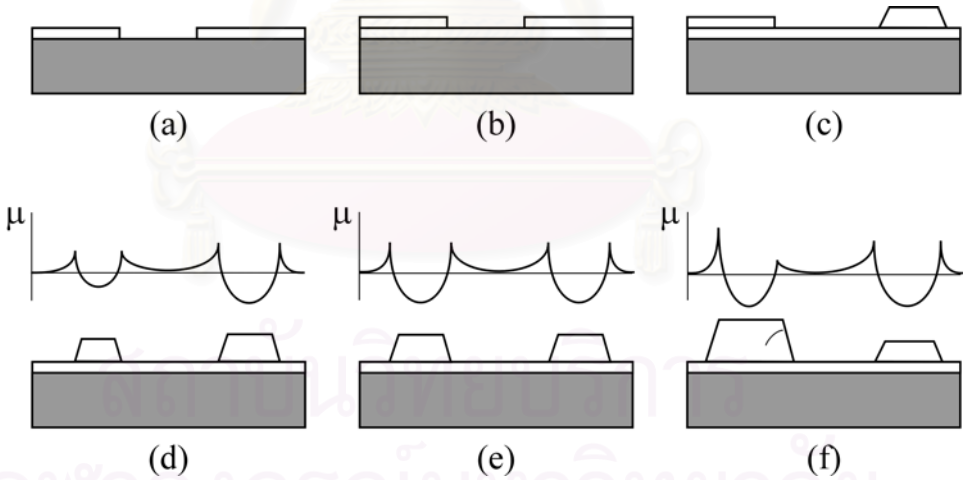

Figure 3.5 Schematic illustration of SK QDs formation process (a) initial stage of wetting layer formation (b) the wetting layer (c) 2-D to 3-D islands transition, (d) non-uniform 3D islands (e) self-regulation process and (f) misfit dislocation formation.

including the dissolution of the larger island causing the narrow size distribution (figure 3.4(d)). When the island size increase further, the misfit dislocation form to relieve the strain concentration (figure 3.4(e)). The strain relief in the island with dislocation decrease the energy barrier, then permit the further growth of the island.

3.2.3 Strain distribution of buried QDs

As described in previous section about the QDs growth process, the strain distribution in QD structure plays an important role for the formation and growth of this structure. The strain profile of free standing QDs originates the mechanism called "self-regulation process" which leads the narrow size distribution of the self-assembled QDs. For the measurement of the basic electronics properties as well as for device applications, it is necessary to create buried QDs by embedding such a nanostructures in a matrix. The matrix normally has a lattice constant matched or nearly matched to the substrate therefore the buried QDs cause the strong deformation of the matrix surround the QDs and produce the non uniform strain distribution on the epitaxial surface. In the case of multi-layer QD with thin spacer layer, the strain modulation in the cap responsible for the preferential nucleation of the QD in the next layer at the place where the local minima of the strain energy locates. The strain profile in the cap layer is not only utilized for the creation of the QDs superlattice but the novel structure such as the nanohole (chapter 5) and the ordering of QDs without patterning can also be obtained by using the strain for the buried QDs (Capellini et al., 2003). This section therefore devotes to the model which provide an understanding of the strain distribution which induce by the buried QDs. We concentrate only on the model, which is based on the continuum elastic theory model. For the simplest model, the buried island is treated as the point-like defect buried in the semi- infinite matrix. This description is a quite good approximation under the condition that the island size is significantly smaller than the cap thickness.

Approximating that the buried islands located at $z=z_0$ and $x=y=0$, the induced in-plane strain distribution which is equal to (Springholz et al.,2001; Hu,1989)

$$\varepsilon'_{//} = \varepsilon'_{xx} + \varepsilon'_{yy} = -P\frac{2z_0^2 - (x^2 + y^2)}{(x^2 + y^2 + z^2)^{5/2}} \tag{3.14}$$

where P is the strength of the point source given by

$$P = \frac{\varepsilon_0 V_0 (1-\nu)}{\pi} \tag{3.15}$$

where ε_0 is the lattice mismatch between the island an matrix material, V_0 is the island volume and ν is the Poisson's ration. By the approximation presented by Springholz et al (2001), they proposed that the radial dimensionless normalized strain energy variation on the surface can be defined as

$$\rho(\mathbf{r}) = \frac{\varepsilon'_{xx} + \varepsilon'_{yy}}{\varepsilon_0} = -\frac{1+\nu}{\pi}\left(\frac{2-(r/z_0)^2}{\left(1+(r/z_0)^2\right)^{5/2}}\right)\times\left(\frac{V_0}{z_0^3}\right) \tag{3.17}$$

where $\mathbf{r} = \sqrt{x^2 + y^2}$. From this equation, the amplitude of $\rho(\mathbf{r})$ is proportional to $\frac{V_0}{z_0^3}$ and its minimum located exactly above the buried island as depicted in figure 3.5. Thus, the elastic strain field scales linearly with the increasing of island volume and decay by one over the cube of the spacer thickness.

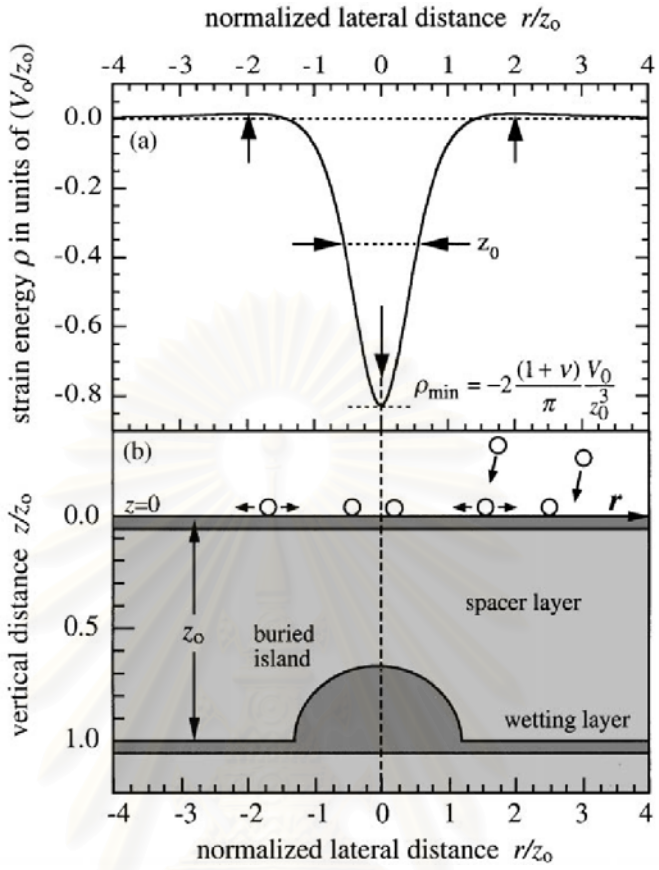

Figure 3.5 (a) Normalized radial strain energy distribution on the wetting layer surface above a buried island in isotropic medium at a depth z_0 as schematically shown in figure 3.3(b). (Springholz et al.,2001)

The strain distribution in the cap layer is responsible for the growth the islands in the next layer, which is evident by the vertical alignment of the islands in multi-stack structure. Considering InAs/GaAs material systems, the GaAs cap layer above buried InAs islands would face the highest tensile strain. When the InAs was deposited to created the islands in the second layer, the deposited In adatoms which impinge on the region where the high tensile strain locates would accumulate there since they can achieve the lower thermodynamic state due to the lower lattice mismatch of InAs with GaAs in tensile strain. For In adatoms which reach the no-strain region, will be driven by the gradient of chemical potential which is modified by the strain field. The chemical

potential, μ, on layer which is responsible for the migration of adatoms on surface can be written as

$$\mu^{In}(\mathbf{r}) = \mu_0^{In} + \Omega E_s(\mathbf{r}) + \gamma\Omega\kappa(\mathbf{r}) \tag{3.18}$$

where μ_0^{In} is the chemical potential of In adatoms on an unstressed surface. The second term describes the contribution of the surface elastic energy, $E_s(\mathbf{r})$, to the chemical potential, with Ω being the atomic volume. The third term is the surface energy contribution, where γ is the surface energy per unit area and $\kappa(\mathbf{r})$ is the surface. In this case the third term can be negligible since the surface is assumed to be nearly flat after covering InAs with GaAs. Hence, the strain contribution is the crucial parameter to modify the chemical potential and drive In adatoms to the region of GaAs with high tensile strain. Figure 3.6 schematically illustrates the vertical alignment mechanism during the growth of second layer island. Xie et al.(1995) presented the pairing probability of the islands in the first and second layer depending on the spacer thickness by using the phenomenological model dealing with the gradient of chemical potential. By using some approximation and fitting parameters, the simulation results agree well with the experiment.

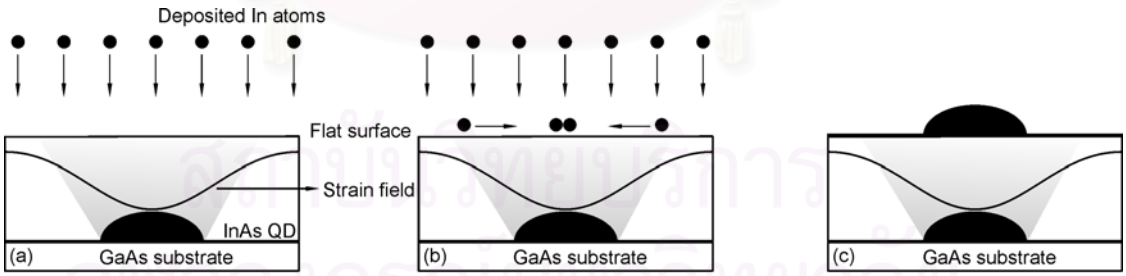

Figure 3.6 The schematic illustration of the vertical alignment process. (a) the uniform In deposition, (b) the accumulation of deposited adatoms at the place where GaAs has high tensile strain (c) the island formation above the buried one.

In additions, Tersoff et al. (1996) pointed out that there is other effect induced by strain from buried island which is responsible for the vertical alignment. They suggested the simple and relatively generic model by assuming the buried island is a point like strain source. The strain from the island decreases the nucleation barrier at the position where the lattice mismatched between the surface and island is reduced. Therefore at the position above the buried island where the highest tensile strain located, it is high potential for the islands to nucleate.

Even though the different explanation of the vertical alignment process between Xie et al. (1995) and Tersoff et al (1996), they suggested that crucial parameter which affect to the growth of the island in the second layer is the strain modulation in the cap layer. Moreover, the strain profile used in the models is a rather simple model approximating the islands as a point like source buried in isotropic medium but agree well with several experimental results. More striking point which mentioned by Tersoff et al. (1996) is that for successive layers, the island size and spacing be comes progressively more uniform; therefore, they suggested that by controlling the spacing thickness, one can directly determines the spacing between the islands. This means that the strain can also responsible for lateral ordering of the islands. Holý et al. (1999) proposed the model, which takes the anisotropic of material into account. Their results indicate that the 3 dimensional ordering of the island are more pronounced in high elastic anisotropic material.

The strain distribution is the important parameter which is responsible for the island formation, the size distribution, the spatial ordering and also the electronics properties of the QDs. Thus, this motivates several theoretical groups to deeply study the strain distribution by using several techniques such as using analytic solution base on continuum elastic theory (Pearson and Faux, 2000), finite element method (Benabbas, 1999) or molecular dynamics technique (Yu and Madhukar, 1999; Daruka,1999) to provide the exact strain distribution of the QDs in different size and shape from different material system. The simulation results must be useful in both fabrication process and device application.

3.3 Material Consideration

The self-assembled growth, which can be used to realize QD structures, can be done in several semiconductor material systems, e.g., In(Ga)As/GaAs, InP/InGaP, and SiGe/Si, because the preliminary condition for the growth is only that the QD material have a larger lattice constant and a smaller band gap compared with substrate material. Figure 3.7 shows the relationship between band gap energy and the lattice constant of III-As material systems. This work concentrate only on the InAs/GaAs material system.

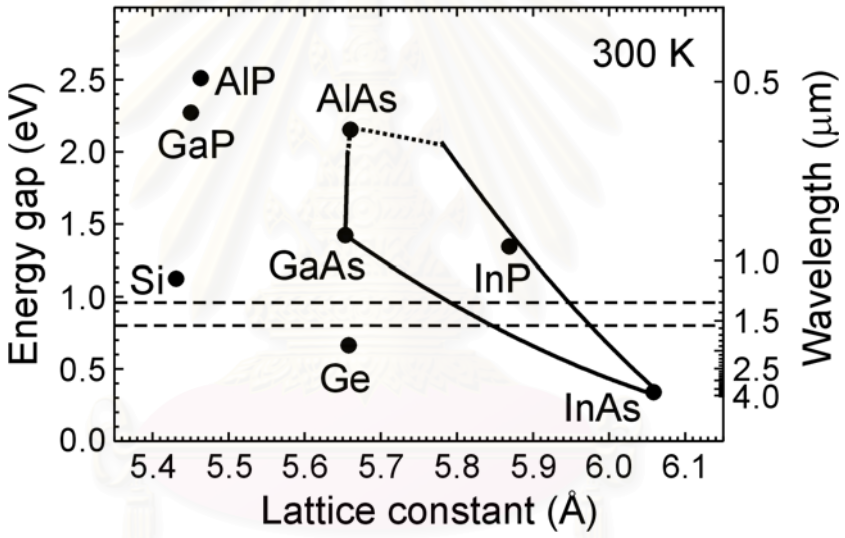

Figure 3.7 The relationship between lattice constant versus energy gap at room temperature of the III-As material system. The lines represent the relationship between energy gap of alloy of two binary compounds and lattice constant. The solid line is for direct band gap material and the dotted line is for indirect band gap material.

Chapter 4

Self assembled InAs/GaAs quantum dots

Apart from processing technique involving lithography and etching, the direct growth of nanostructures has evolved as a promising approach due to the simplicity of fabrication process. It is based on the tendency of strained epitaxial layers to spontaneously form islands after completion of the 2-D wetting layer. The islands obtained by self assemble growth are three dimensional, epitaxial and coherently strained. This chapter focuses on islands grown by using InAs/GaAs materials system with 7% lattice mismatch. The fundamental parameters of the growth process are systematically examined to provide the understanding of the islands formation and the tuning of island properties by changing growth parameters. The experimental results are divided into 2 parts: the structural properties of InAs QDs as a function of growth conditions and the optical properties of different types of QDs thoroughly investigated by PL measurements.

The fundamental experiments in this chapter give the basic idea of the QDs growth and their optical properties. Despite the simplicity of this experiment, the results are crucial issues for tuning the QDs for desired applications.

4.1 InAs/GaAs self assembled QDs growth

This section presents QDs realization by systematically tuning the growth conditions such as growth rate, amount of deposition and substrate temperature.

Effect of deposited amount of InAs

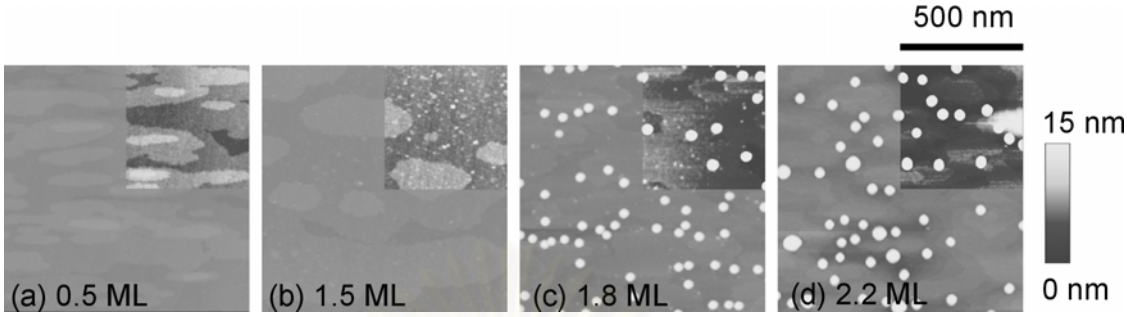

Figure 4.1 The 1×1 μm^2 AFM images of thin InAs on GaAs surface (a) 0.5 ML, (b) 1.5 ML, (c) 1.8 ML, and (d) 2.2 ML. The inset shows height contrast image (2-nm height scale)

In this experiment, the InAs was deposited at 500°C with the growth rate of 0.01 ML/s, and the amount of deposited InAs was changed from 0- 2.0 ML. Figure 4.1 shows AFM images of the surface morphology after the deposition of different amounts of InAs. With 0.5 ML of InAs, the surface shows the terraces with 1-ML height elongated in [1-10] direction due to the anisotropic diffusion coefficient (Figure 4.1(a)). 2D islands, which are initial stage for 3D-island formation, are clearly observed when InAs thickness reaches 1.5 ML as shown in figure 4.1(b). The 1.8 ML of InAs deposition provides QDs which have average height 10.7 nm and the diameter of 38 nm with low density of 3-6 × 10^9 cm^{-2} as illustrated in figure 4.1(c). The island density does not significantly increase if the deposited amount of InAs is beyond 2.2 ML. On the other hand, the non-uniform size distribution of the QDs occurs and the 2D islands disappear.

As described in chapter 3, after the completion of the wetting layers, the small 2D islands nucleated. Further InAs deposition causes 2D islands to reach a critical size at which the 2D-island to 3D-island transformation starts. The 3D-islands will act as a material sink of the adatoms on the surface, not only deposited adatoms but also the material from 2D islands. Therefore, the deposition beyond 1.8 ML of InAs which causes uniform fully develop islands will introduce the non-uniform size distribution and disappearance of 2D islands. The atom detachment from 2D islands to large islands prohibits the increasing of island density. The larger islands observed at 2.2 ML of InAs

deposition result in the onset of dislocation formation during the overgrowth process due to the excessively high strain (Chen and Washburn, 1996).

Effect of InAs growth rate

Figure 4.2 shows AFM images of the 1.8 ML of InAs QDs grown on (001) GaAs substrate at 500°C by using different growth rate in the range of 0.01-0.4 ML/s. The dot density changes from 1.20×10^{9} cm^{-2} to 4.24×10^{11} cm^{-2} and the average dot height decreases from around 14 nm to 5 nm.

The dot height and dot density as a function of InAs growth rate in figure 4.3(a) reveals that the 3D-island density increases and the dot size decreases with the growth rate. For higher growth rates, island formation is put into a narrow time interval, resulting in less material diffusion as well as smaller diffusion length. Therefore 2D-3D nucleation process occurs at a relatively higher rate (Seifert et al., 1996; Nakata et al., 1999). In this limit, the 3D islands density is controlled by the 2D-island density, which nucleate on the wetting layer (Seifert et al., 1996). At the growth rate higher than 0.1 ML/s, the dot density shows the tendency of saturation. Although the number of 2D islands continue to increase with the degree of supersaturation (growth rate in this case), with high density the 2D-island size eventually fall below the critical value for 2D to transition to 3D islands, thus, the dot density saturate or even decrease in some cases at high growth rates (Dobbs et al., 1997).

Due to the material conservation, the low density QDs should have larger size compared to the high density QDs. Seifert et al. (1999) suggested that the relationship between average size and density yield $\bar{h} \alpha \rho^{-\frac{1}{3}}$ by approximating the island shape as a spherical cap structure. However, the summary of average dot height as a function of the growth rate in figure 4.2(b) shows a power law relationship between dot height and dot density that yields the exponent equal to –0.17. Therefore, the results can not be completely explained by mass conservation since there is a high degree of Ga interdiffusion into the dots depending on growth conditions (Joyce et al., 2000).

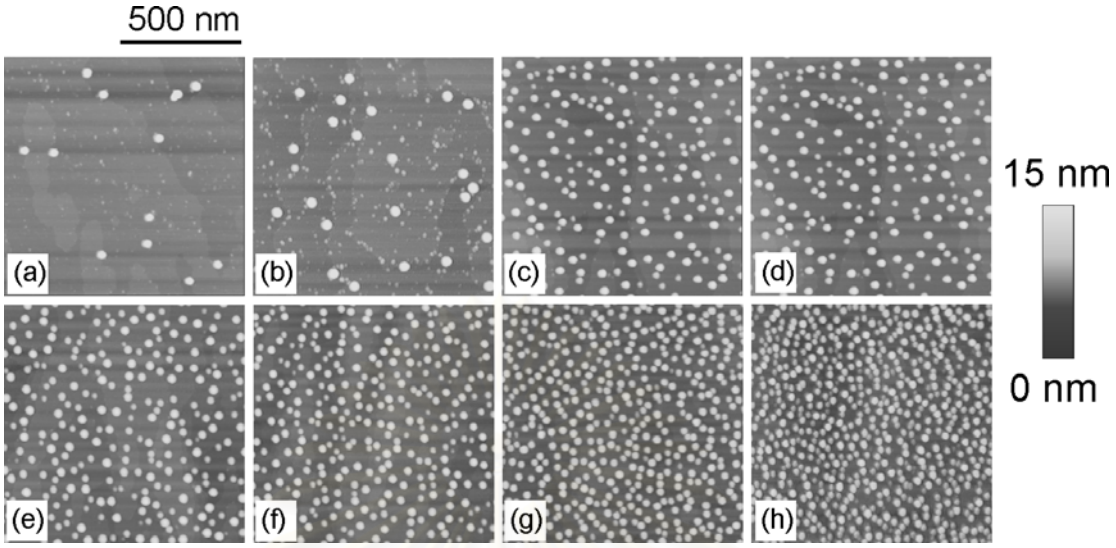

Figure 4.2 1×1 μm^2 AFM images of large InAs QDs grown at (a) 0.005 ML/s (b) 0.008 ML/s (c) 0.03 ML/s (d) 0.04 ML/s (e) 0.06 ML/s (f) 0.1 ML/s (g) 0.2 ML/s and (h) 0.4 ML/s.

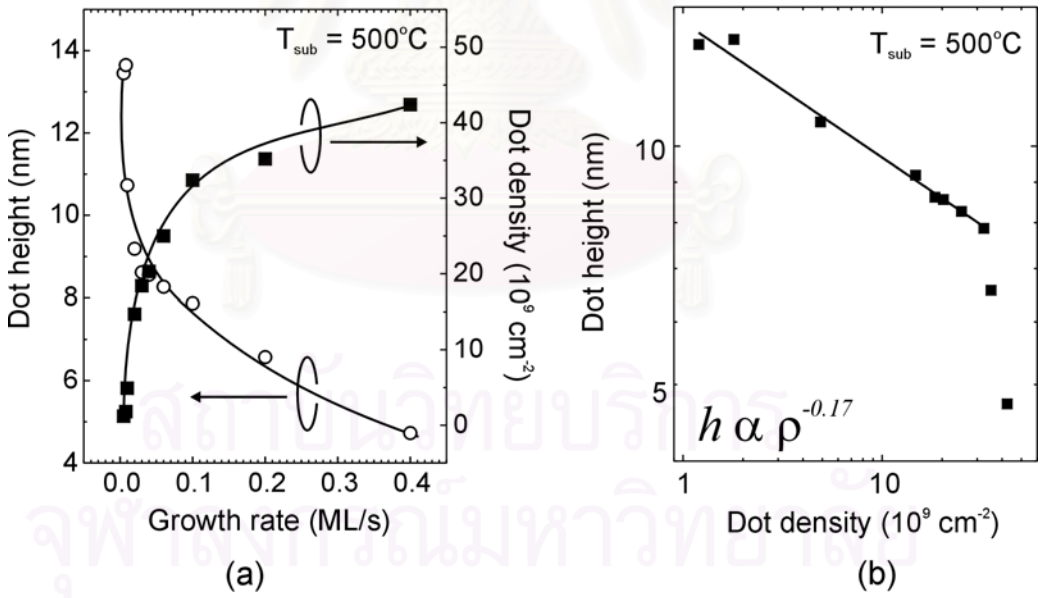

Figure 4.3 (a) Dot height and dot density as a function of the growth rate. (b) Average dot height versus dot density plotted on a log-log scale. A power fit yields the exponent –0.17. The 0.2 and 0.4 ML/s values are excluded from the fit.

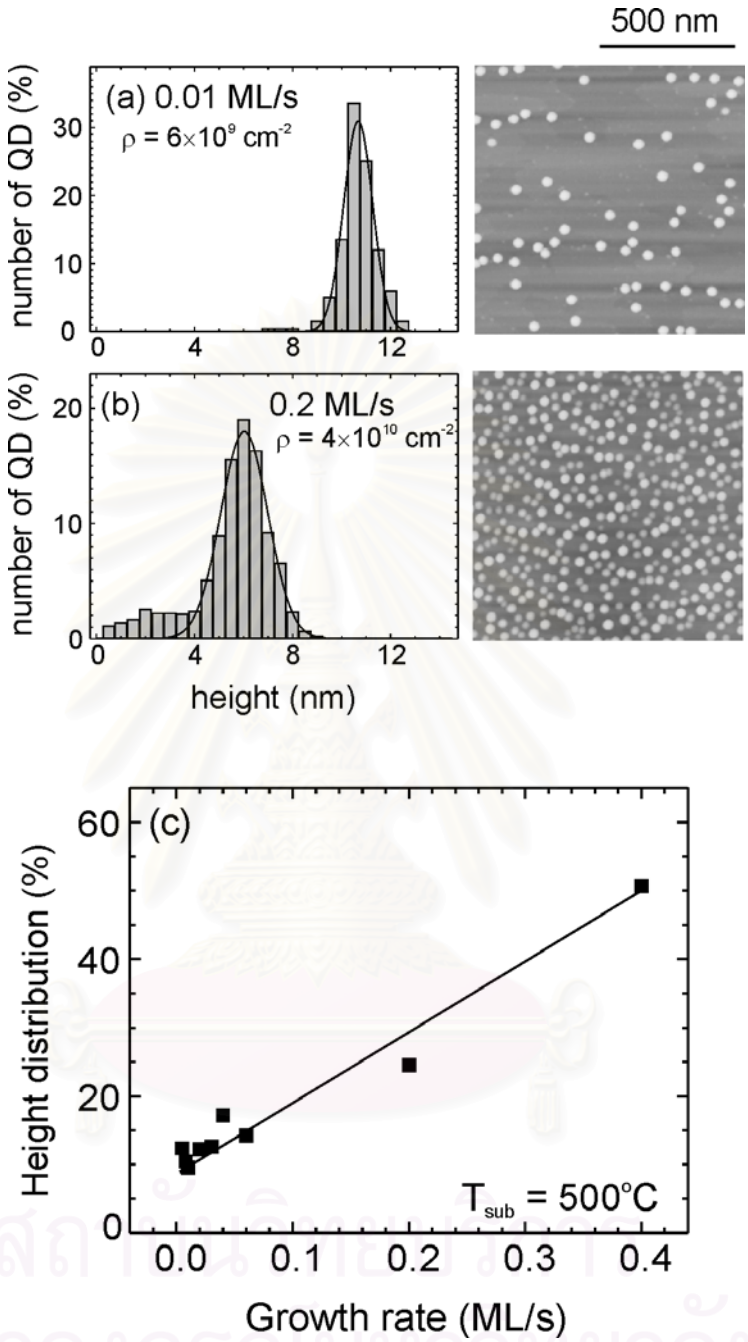

Figure 4.4 The height distribution of the QDs grown with (a) 0.01 ML/s and (b) 0.2 ML/s (c) percent distribution of the height of the fully developed island versus InAs growth rate.

Figure 4.4(a) and (b) show the height distribution and corresponding AFM images of the QDs grown by using the growth rate of 0.01 ML/s and 0.2 ML/s, respectively. Small dot with high density grown by using high growth rate shows broader size distribution. The size distribution dependence on growth rate can be explained as follows. After the completion of wetting layer, the islands started to form. The adatoms incidents after island formation were preferably incorporated into existing islands which acted as a material sink. The uniformity of QDs ensemble is caused by self-regulation process which is mainly due to the surface strain field. The strain field modifies the chemical potential on the surface and leads the directional migration of adatoms from large dot to small dots, resulting in the high growth rate of smaller dots compared to the larger ones. The decreasing of the growth rate enhances the In adatom migration lengths. Therefore, the adatoms have high possibility to reach small islands and incorporate therein. In case of high deposition rate, with less migration length, In adatoms can not find the most suitable places to attach, leading the non uniform size distribution. In other words, the large adatom migration length enhances the self-regulation process.

Effect of InAs growth temperature

Figure 4.5 shows AFM images of the 1.8 ML of InAs QDs grown on (001) GaAs substrate by using growth rate in the range of 0.008- 0.01 ML/s at the substrate temperature in the range of 450°C-515°C. The dot density changes from 1.0×10^{9} cm^{-2} to 2.37×10^{10} cm^{-2} and the dot height decreases from around 14 nm and 5 nm by decreasing the substrate temperature.

The summary of dot density as a function of the growth temperature is shown in Figure. 4.6. The observed dependencies of dot density and dot size agree well with a classical nucleation theory presented in chapter 3 that the nucleation density increases with substrate temperature. Moreover, the AFM images show that the dots preferentially nucleate at kinks or steps on the surface, especially at lower substrate temperature. Since kinks or steps are the places which have minimum energies, In adatoms would be collected at kinks and easily form stable 2D-islands which is the initial stage of 3D islands. The effect of the low substrate temperature is in the same direction as the increase in the InAs growth rate, which cause the high density with small size QDs.

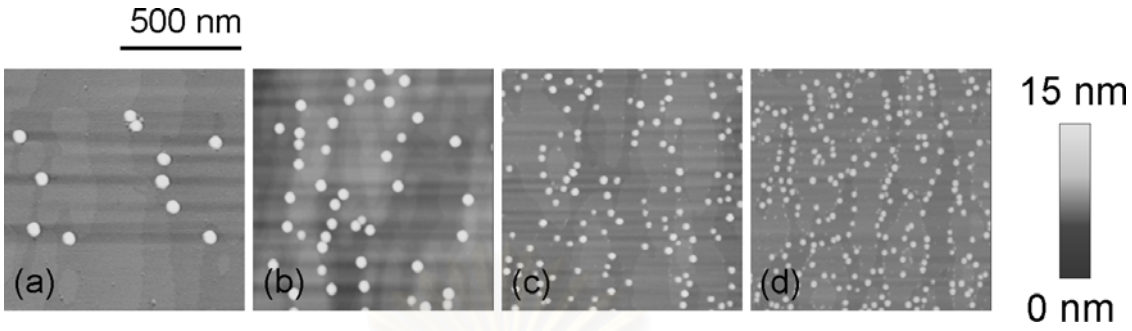

Figure 4.5 **1×1 μm^2 AFM images of InAs QDs grown at substrate temperature equal to (a) 515°C (b) 493°C (c) 470°C (d) 450°C**

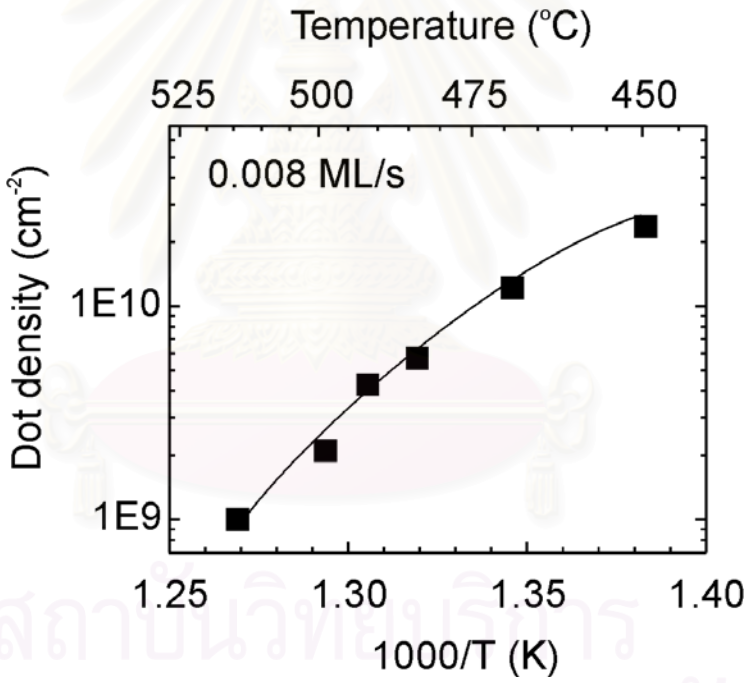

Figure 4.6 Dot density as a function of the substrate temperature. The InAs growth rate was kept at 0.008 ML/s.

Annealing of QDs structure

In this experiment, the large QDs, which are grown at substrate temperature of 500°C with a very low growth rate of 0.01 ML/s and with a 30 sec growth interruption to improve the dot size uniformity, are annealed at substrate temperature in the range of 450°C -500°C for 5 min. The dot shape and density are investigated by AFM measurement depicted in figure 4.7. The dot height and density are similar to the QDs with zero annealing time. In additions, we observed that at 450°C by increased annealing time from 0 to 5 min., the PL spectra from the QDs are similar (Figure 4.8).

Kiravittaya et al. (2001) reported that the 30 second growth interruption at 500°C can improve the size uniformity of the large dots. The annealing time beyond 30 second deteriorate the uniformity of the QDs ensemble due to the thermal desorption of In from the surface leading to the dissolution of existing islands. In this experiment, the annealing temperature was kept below 500°C since the desorption of indium atoms is negligible. The AFM results show that there is no significant effect of annealing process at these low temperatures. At substrate temperature equal to 450°C where the In desorption rate is nearly zero, PL results reveal that annealing process does not play an important role in the optical properties of the large QDs.

The shape preservation of large QDs during low annealing temperatures combined with their narrow size distribution is one indication that large QDs are equilibrium structures. Furthermore, the scanning tunneling microscopy (STM) results reported by Costantini et al.(2003) showed that the large low density QDs are composed of (110) and (111) facets and can compare to the theoretical prediction of the equilibrium shape of InAs islands on GaAs (001) substrate (Moll et al., 1996). Therefore, we can deduce that the growth conditions which provide the large QDs with low density (low growth rate (less than 0.01 ML/s) and high substrate temperature (500°C)) are close to thermodynamic equilibrium.

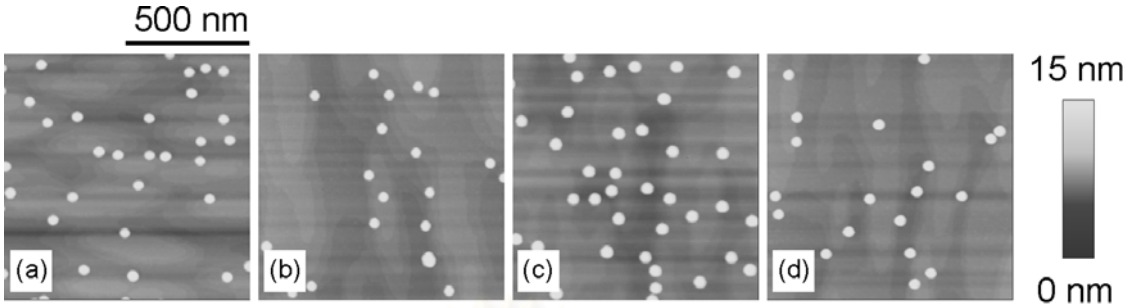

Figure 4.7 1×1 μm^2 AFM images of large InAs QDs grown at 500°C after 5-min annealing at (a) 470°C (b) 450°C (c) 430°C and (d) 400°C

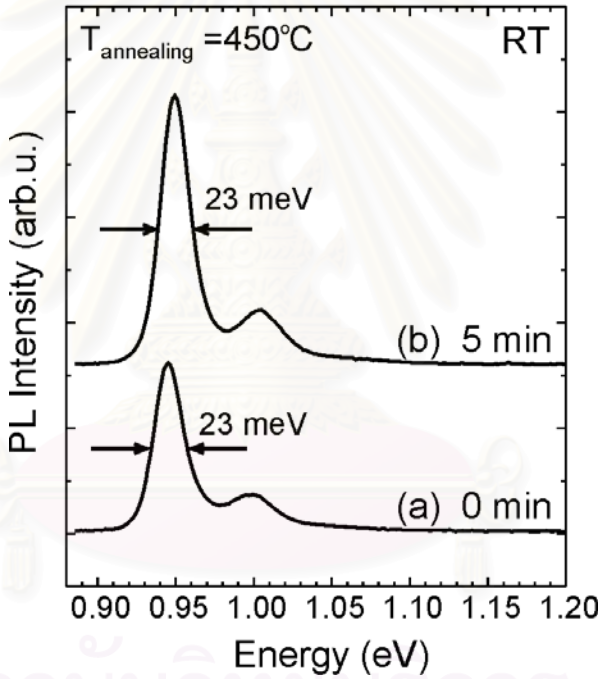

Figure 4.8 PL spectra at room temperature of large InAs QDs grown at 500°C after 450°C annealing at (a) 0 min and (b) 5 min

4.2 Photoluminescence from self-assembled InAs/GaAs QDs

In this section, the optical properties of QDs investigated by PL are comparatively studied among different types of the QDs.. In this study, the 1.8 MLs of the InAs QDs were grown at various InAs growth rates such as 0.01, 0.04, and 0.2 ML/s and are defined as the large, medium, and small QDs, respectively. The substrate temperature was decreased to 470°C after finishing QD growth. The GaAs cap layer was grown during which the temperature was increased to 500°C.

Size dependence photoluminescence

Room temperature PL spectra from the large, medium and small QDs excited by 5 mW and 500 mW are shown in figure 4.9. The ground state peak systematically red shifted from 0.957 eV to 1.00 eV and the separation between the ground state and excited state increased from 51 meV to 75 meV by increasing the deposition rate. At low excitation power, the PL linewidth was in the range of 23-26 meV. At high excitation power of 500 mW, PL linewidth from experimented structure broaden to 31-32 meV

The results correspond to the relation between the dot size and carrier energy levels in QDs presented in chapter 3 that the minimum energy level and the energy separation between each quantized state increase as dot size decreases. At low excitation power, the PL linewidth is rather narrow compared to that from the InAs QDs covered with GaAs at high substrate temperature (Nakata et al., 2000). The results are mainly due to the suppression of In segregation during the overgrowth process by using low substrate temperature overgrowth which will be discussed later in chapter 5. The PL spectra broadening at high excitation power was suggested by Grundmann et al. (1996) that it was caused by the excited state peak that convoluted with the ground-state peak.

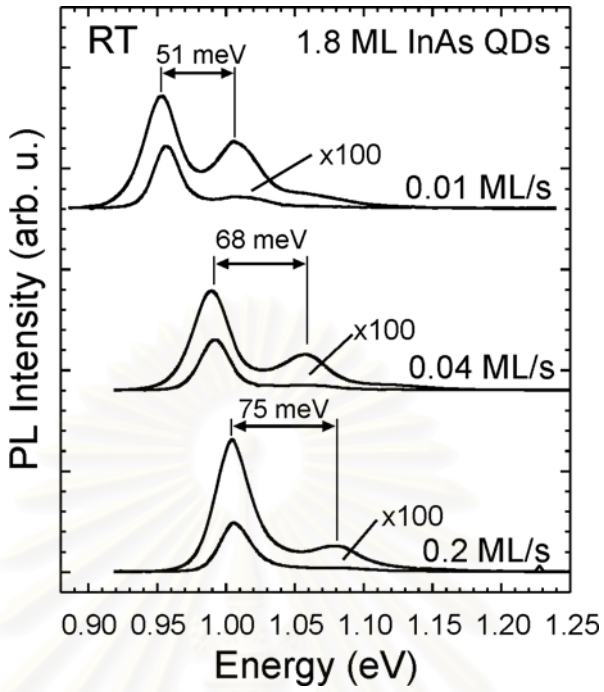

Figure 4.9 (a) Room-temperature PL spectra of 1.8 ML InAs QDs grown at InAs growth rates of 0.01 ML/s, 0.04 ML/s and 0.2 ML/s with excitation powers ranging from 5 to 500 mW (lower and upper spectrum, respectively).

Power dependence photoluminescence

The PL peak intensity dependence on the excitation power is shown in Figure 4.10 (a). All ground state peak intensities monotonically increase as the excitation power increases. However, the ground-state peak intensity of the large QDs increases at a slower rate than that of small QDs attributed to the lower density of the large QDs grown at low growth rates. At high excitation power, the PL intensity shows the saturation tendency. This is due to the state filling effect. Figure 4.10(b) reveals that the ratio of the first excited-state peak intensity to the ground-state intensity of these QDs also increases. As a consequence, the number of photo-excited carriers recombining through the excited states is expected to be larger for the large QDs. It is clearly seen that the ratio is higher for low-density QDs compared to the high-density QDs because the filling of ground

state is more pronounced for the low density QDs due to the smaller number of available states.

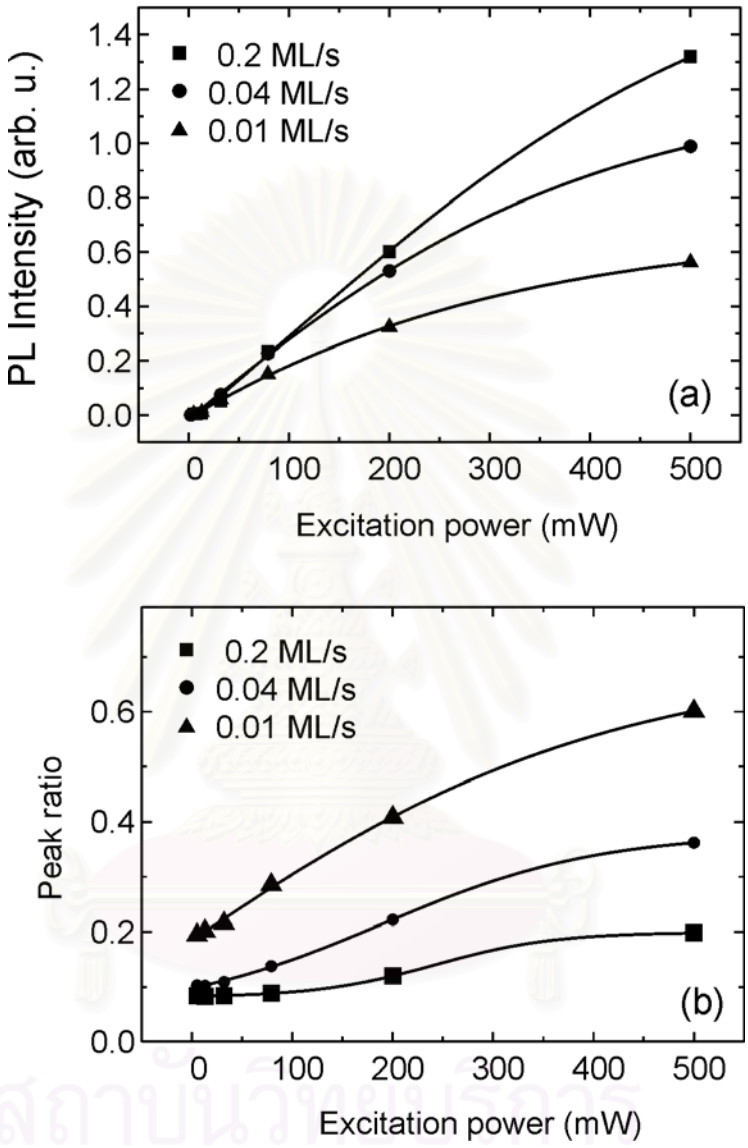

Figure 4.10 (a) PL peak intensity dependence on excitation power for the QDs grown at different growth rates. (b) The ratio of excited state peak intensity to the ground state peak intensity of these QDs.

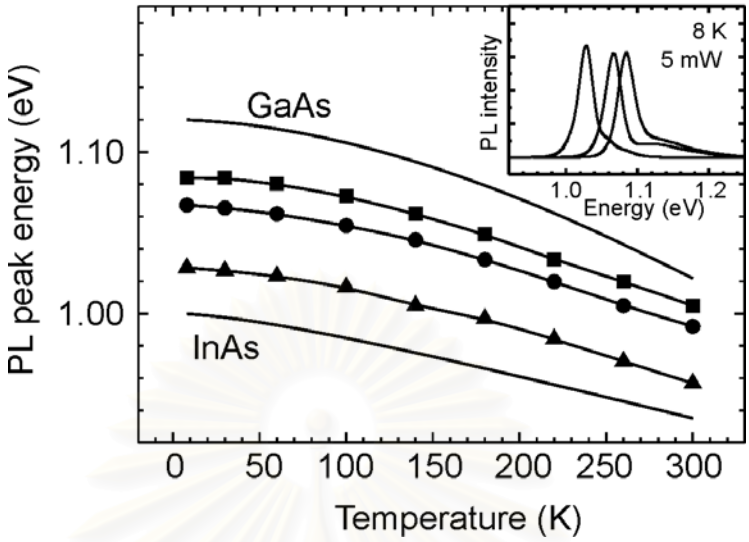

Figure 4.11 PL ground state peak energy as a function of PL temperature of the QDs grown at 0.2 ML/s (■), 0.05 ML/s (●), and 0.01 ML/s (▲). The solid lines represent the slope of GaAs and InAs energy gap as a function of temperature. The inset shows typical spectra of QDs at 8 K.

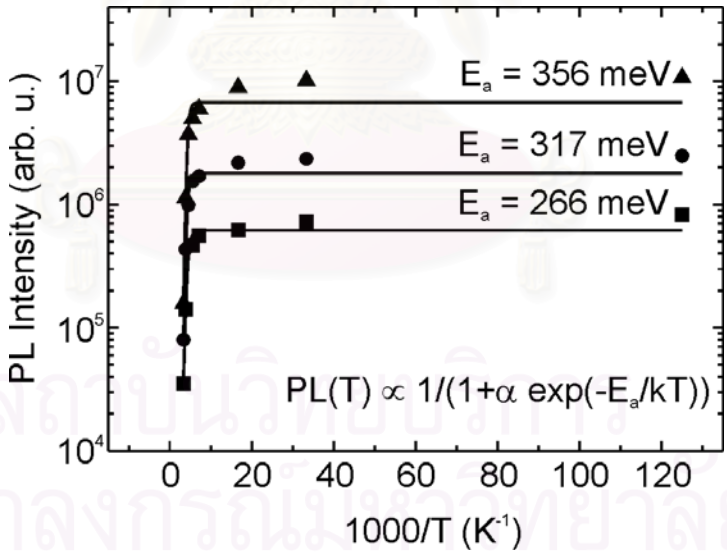

Figure 4.12 PL ground state intensity as a function of PL temperature of the QDs grown at 0.2 ML/s (■), 0.05 ML/s (●), and 0.01 ML/s (▲). The activation energy E_a is extracted by fitting the data with PL(T) = c/(1+α exp(-E_a/$k_B T$)).

Temperature dependence photoluminescence

The dependence of PL ground-state peak energies as a function of temperature for the QDs is shown in Figure 4.11 and compared with the temperature dependence of the bulk InAs and GaAs bandgap. When the measuring temperature is increased from 8 K to 300 K, we observe 71-79 meV redshifts of the relevant PL peak energies. The results reveal that the relation of the PL peak energy change with temperature according to Varshni's law with fitting parameters between GaAs and InAs bulk material parameters taken from Bhattacharya (1993). The main reason for these shifts might be the temperature dependence of the material bandgaps. Moreover, the lineshapes of the PL spectra are invariant to the temperature change. Low-temperature PL spectra are shown in the inset of Figure 4.11. The invariance confirms that the linewidth is dominated by the inhomogeneity of the QDs and that thermal broadening is negligible.

Figure 4.12 shows the temperature dependence of the ground state PL intensities. The equation used for fitting with the experimental result is the simple equation to find the activation energy of quantum wells and also applied for the quantum dots (Farfard et al., 1996; Bacher et al., 1991)

$$I(T) = \frac{\mathrm{C}}{1 + \alpha e^{-\frac{E_A}{kT}}} \tag{4.1}$$

where C is constant, α is a fitting parameter, k is the Boltzmann's constant, and T is the measuring temperature. This equation means that the PL intensity will decrease with the temperature. Even thermal energy are small compared to the activation energy, there should be a certain part of carrier jump out of the QDs structure due to thermal excitation. We observe the onset of the thermal quenching at about 220 K for our QDs. The activation energy (E_a) for the PL quenching can be determined by fitting the PL intensity The E_a values are equal to 356 meV, 317 meV, and 266 meV for the QDs grown by 0.01 ML/s, 0.04 ML/s, and 0.2 ML/s, respectively. These values correspond to the higher carrier confinement in large dots compared to small dots. Note that, the quenching phenomenon does not affect the PL linewidths of the ground- and the excited-states of the QDs because the linewidth is almost constant over the whole range of measuring temperatures.

Chapter 5

Overgrowth of self-assembled InAs QDs

Recently, it has been reported that the shape of InAs QDs changes drastically during the initial stage of GaAs overgrowth (Garcia et al., 1997; Joyce et al.,2001; Lorke et al. 2001; Heidemeyer et al., 2002; Blossey et al. 2002.). P. B. Joyce et al. (2001) reported the collapse and the shape change of the conventional QDs grown by 0.1 ML/s during the early stage of the encapsulation. This research group also observed the changes of the shape and surface morphology of the large QDs (Joyce et al., 2001). By using different growth processes, the shape QDs during overgrowth evolve into a different structure. Lorke et al. (2001) claimed that they observed the quantum ring properties of the partially covered InAs QDs with GaAs. While much effort has been devoted to understanding the processes involved during QD nucleation and growth, far less attention has been paid to the overgrowth and capping processes.

In this chapter, the overgrowth of large low-growth-rate (LGR) InAs QDs with InGaAs (In composition 0-20%) at low substrate temperature was investigated. In order to understand the effect of the cap layer on the QD structure, the strain (In composition) and the thickness of the cap were systematically changed and atomic force microscopy (AFM) was employed to study the QDs shape evolution. Not only the structure evolution but also the optical properties of the experimented samples were investigated by photoluminescence (PL) measurement. The chapter comprises two parts: the structural evolution and the optical evolution.

5.1 Surface evolution during the overgrowth of InAs QDs

The experiment in this section provides an information of surface evolution during the overgrowth of the large LGR QDs. The results obtained by the systematic variation of the cap thickness and the strain between the cap layer and QDs (In

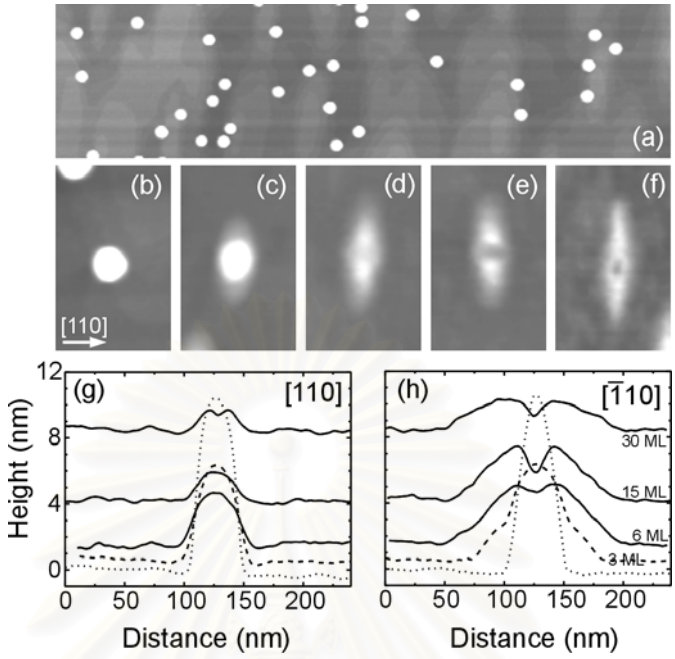

Figure 5.1 (a) 2×0.5 μm^2 AFM image of large InAs QDs after 300 s GI and 0.125×0.2 μm^2 AFM images of QD capped at 460°C with (b) 0 ML, (c) 3 ML, (d) 6 ML, (e) 15 ML, and (f) 30 ML GaAs. (g) and (h) show the linescans of single partially covered dot along [110] and [-110], respectively. The dotted line is the linescan of a free-standing QD.

composition in the cap layer) indicate the factors which induce the evolution of the QDs during the overgrowth process at low substrate temperatures.

The 1.8 ML InAs were deposited at a growth rate of 0.01 ML/s at a substrate temperature of 500°C. After the dot formation, a 30 second growth interruption (GI) was inserted to improve the dot size uniformity (Kiravittaya et al., 2002). The substrate temperature was decreased to 460°C and a 300 s GI was inserted to adjust the In source cell temperature. Subsequently, $In_xGa_{1-x}As$ layers with x = 0-0.2 were grown at a growth rate of 0.6 ML/s and the thickness of the overlayer was varied up to 30 MLs.

The AFM images and the linescans in figure 5.1 illustrate the evolution of large LGR InAs QDs partially capped with GaAs of various thicknesses. The linescans were taken along the [110] and [-110] directions through the middle of the nanostructures.

Figure 5.1(a) shows the reference sample decorated with LGR InAs QDs after a 300 s GI at 460°C. The average dot height and diameter are 11.8 nm and 44.1 nm with ±5.5% and ±8.5% fluctuation, respectively. The dot density is 3×10^{9} cm^{-2}. It is noteworthy that the size distribution and density are similar to the LGR QDs grown under the same conditions but without the 300 sec GI. Figures 5.1(b)-(f) illustrate the evolution of the QD at the initial stages of GaAs overgrowth at low temperature of 460°C. We find that the dot height collapses to 5-6 nm when capped with 3 ML GaAs. The material taken away from the top of the QDs is possibly seen as shallow elongated mounds around the QD in [-110] direction (Figure 5.1 (c)). An even more drastic shape change is observed after 6 ML GaAs deposition. At this stage the height has reduced to only 2.93 nm in the middle of the structure. The base of the partially capped QD experiences a further anisotropic elongation along the [-110] direction and the average base length defined along the [-110] and [110] directions increase to 148.0 nm and 69.5 nm, respectively. Furthermore, a shallow valley forms, which runs through the middle of the mound structure along the [110] direction (Figure 5.1(g) and (h)). The average depth of this valley relative to the flanking ridge is 0.47 nm. For 15 ML GaAs deposition, the valley depth increases to 1.45 nm but the base length and width are preserved. Figure 5.2(f) reveals that – for 30 ML GaAs thickness – the valley shape structure eventually transforms into a well-defined hole with an average depth of 0.73 nm. The elongation of the buried structures is attributed to the anisotropic migration of adatoms in the [-110] direction (Shiraishi et al., 1992).

To investigate the effect of the cap layer on the shape evolution of the covered dot, the lattice mismatch between the cap and the dot was adjusted by varying the In composition and the thickness of the $In_xGa_{1-x}As$ overlayer. Figure 5.2 shows the AFM images and the corresponding linescans of the QDs by an $In_xGa_{1-x}As$ layer (x=0.1 and 0.15). The deposited material, in case of 6 ML $In_{0.1}Ga_{0.9}As$, surrounds the existing dots and the buried dots elongate into the [-110] direction as shown in Figure 5.2(a). The initial dots become completely covered after the deposition of 30 ML of $In_{0.1}Ga_{0.9}As$. The base length defined in the [-110] direction increases with increasing thickness of the overlayer.

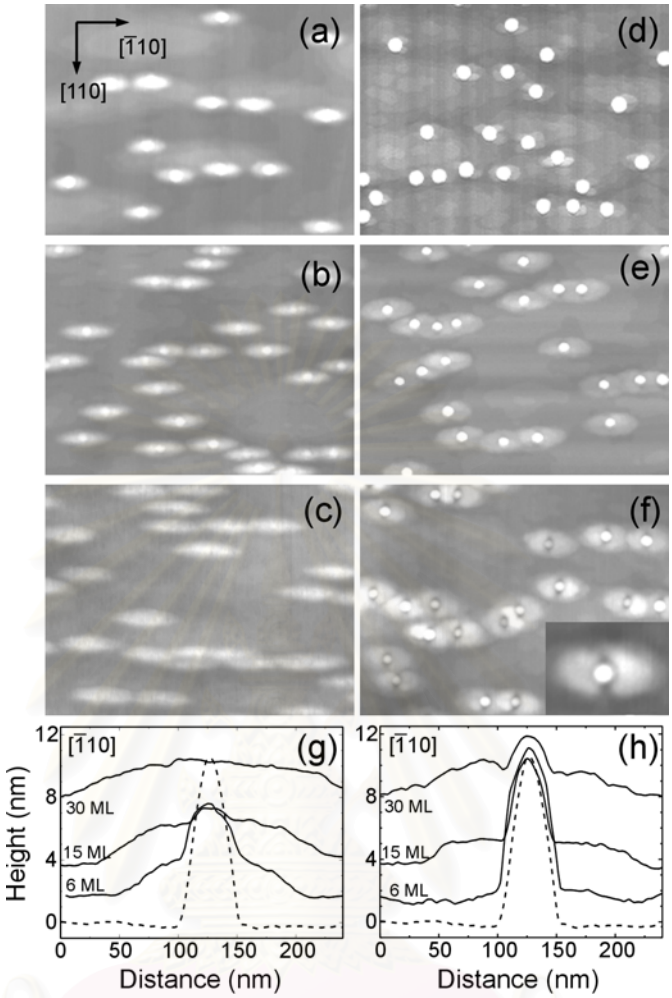

Figure 5.2 $1\times0.75\ \mu m^2$ AFM images of large InAs QDs after (a) 6 ML, (b) 15 ML, and (c) 30 ML $In_{0.1}Ga_{0.9}As$ overgrowth and (d) 6 ML, (e) 15 ML, and (f) 30 ML $In_{0.15}Ga_{0.85}As$ overgrowth at 460°C. The inset in (f) is a zoomed AFM image ($0.2\times0.15\ \mu m^2$) of the dot overgrown with 30 ML of $In_{0.15}Ga_{0.85}As$. (g) and (h) show the linescans along [-110] of single partially covered dots with $In_{0.1}Ga_{0.9}As$ and $In_{0.15}Ga_{0.85}As$, respectively.

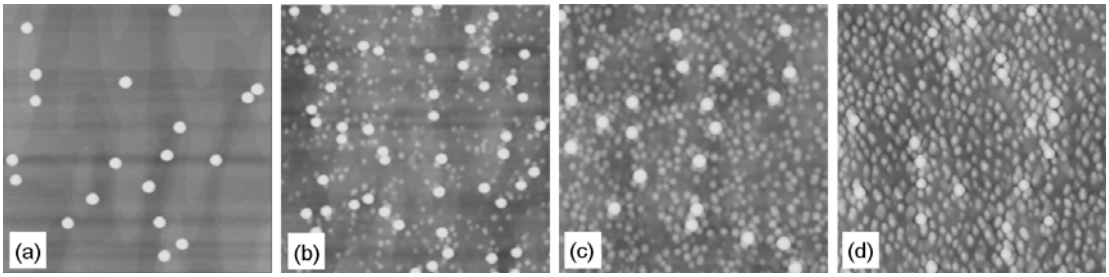

Figure 5.3 1×1 μm^2 AFM images of large InAs QDs after (a) 0ML (b) 3 ML, (c) 6 ML, and (d) 30 ML of $In_{0.2}Ga_{0.8}As$ overgrown at 460°C.

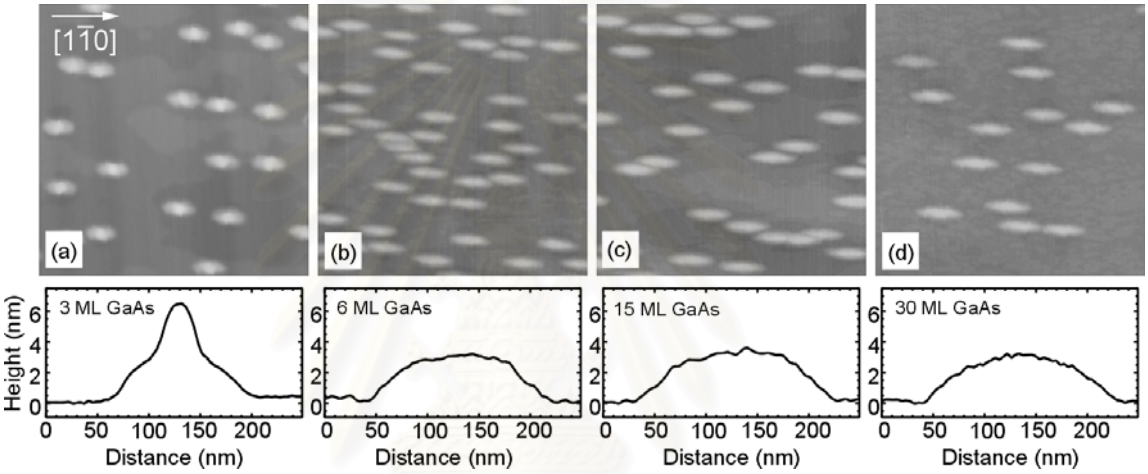

Figure 5.4 1×1 μm^2 AFM images of large InAs QDs after (a) 3 ML, (b) 6 ML, (c) 15 ML, and (d) 30 ML of GaAs overgrown at 500°C.

Figures 5.2(d)-(f) shows a similar series of samples, where the overgrowth material consists of $In_{0.15}Ga_{0.85}As$. Figure 5.2(d) shows that after the deposition of 6 ML $In_{0.15}Ga_{0.85}As$ small platelets with 2-3 ML height form around the QDs and arrange themselves in the [-110] direction. With further deposition up to 15 ML $In_{0.15}Ga_{0.85}As$, the overgrowth material mounts up around the QDs, leaving the QD shape in the middle unchanged. The material mounds around the dots are elongated and align along the [-110] direction. The $In_{0.15}Ga_{0.85}As$ overlayer does not cover the dot even after 30 ML overgrowth, and there is a thin trench between the dot and the surrounding mound as shown in the inset of figure 5.2(f). In addition, when the In content of the overgrown layer is 20%, with only 3-ML thickness, we observed the formation of the tiny dots in

between the large dots as shown in figure 5.3(b). Further deposition of $In_{0.2}Ga_{0.8}As$ increases the size and the density of the tiny dots (figure 5.3(c)-(d)).

Moreover, we investigated dot shape evolution during the overgrowth at 500°C as shown in figure 5.5. At the first 3 ML of GaAs deposition (figure 5.5 (b)), the mound shape, with the remains of the QDs in the middle, form as the case of substrate temperature equal to 460°C and the QDs height rapidly decreases. With increasing GaAs thickness, we observe only the elongation of the mound structure without the ridge valley formation (figure 5.5(c) and (d)).

The height (h) evolutions of the QDs as a function of the In composition and the thickness of the overlayer are summarized in figure 5.5. The definitions of the heights of the different structures are given in the figures. The height of the ridge-valley (ridge-hill) is defined from the bottom of the valley (the top of the hill) to the flat surface. By assuming that the overlayer simply surrounds the dot without any effects on the dot shape and size as the schematic in figure 5.5(a), the straight dotted line in figure 5.5(b) represents the expected height (the average dot height subtracted by the cap thickness, h_0-h_{cap}). The average measured height is plotted as a function of the $In_xGa_{1-x}As$ thickness. We find that the height of partially covered dots approaches the dotted line with increasing In content. For In contents less than 20%, the measured dot height decreases faster than the increase of the cap layer thickness, indicating the collapse of the QDs at the early stage of the overgrowth. Similar observations were reported by Joyce et al. (2001) and Garcia et al.(1997). In case of an $In_{0.2}Ga_{0.8}As$ cap, the dot height even slightly exceeds the expected height (dotted line). This behavior is caused by the formation of tiny dots between the existing large dots as presented in figure 5.4. Hence, overgrowth material is used to form these small dots instead of surrounding the large ones, which causes the deviation of the experimental data points from the dotted line in figure 5.5.

An interesting result is observed if the QDs are overgrown at higher temperatures (500°C) (dashed line in figure 5.5). In this case the QDs collapse at the same rate as those overgrown at low temperature (460°C), but the height saturates at a value close to the case of $In_{0.1}Ga_{0.9}As$ overgrowth. The inset of figure 5.5 shows the transition from the ridge-valley to the ridge-hill structure as a function of In content in the cap layer. The hill height and the valley depth are defined as the positive and negative value of h_2 in the

schematic. The inset quantifies that the valley depth becomes shallower and even transforms into the hill structure when the In content of the overlayer is increased.

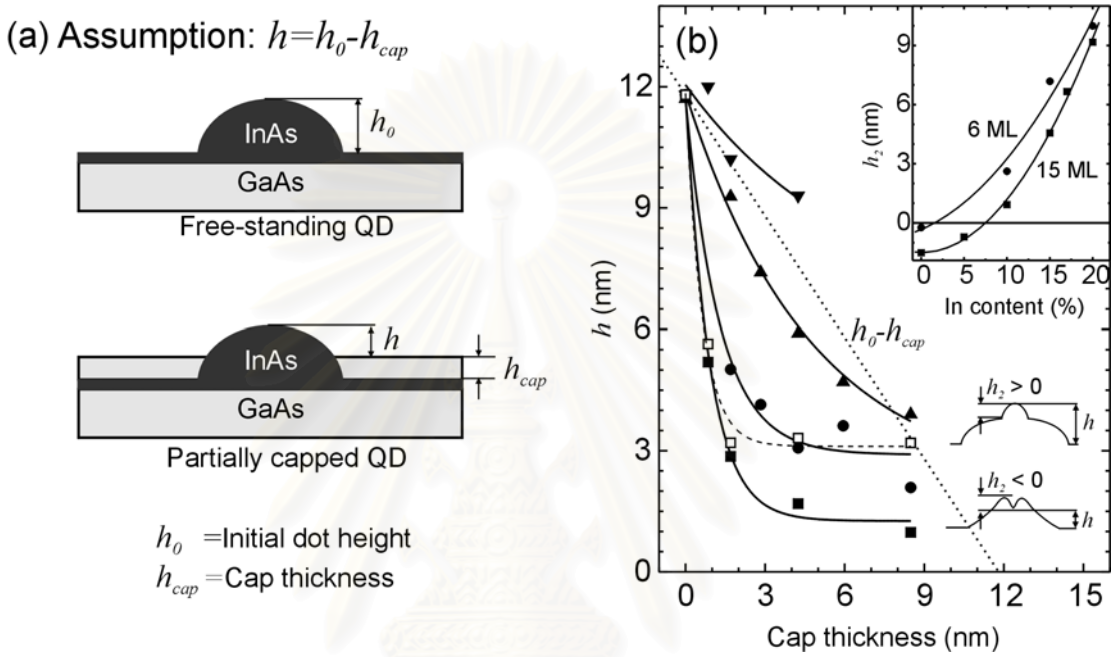

Figure 5.5 (a) The schematic showing how the QD height (h) was obtained from AFM images after GaAs overgrowth; h_0 is the initial dot height and h_{cap} is the GaAs cap thickness. (b) Height (h) of partially capped large InAs QDs as a function of the cap thickness for GaAs (■), $In_{0.1}Ga_{0.9}As$ (●), $In_{0.15}Ga_{0.85}As$ (▲), $In_{0.2}Ga_{0.8}As$ (▼) with the overgrowth temperature equal to 460°C and GaAs (□) with the overgrowth temperature equal to 500°C. The dotted line is the nominal height calculated from the dot height minus the cap thickness (h_0-h_{cap}), assuming that the cap only surrounds the dot. The inset shows the hill height or the valley depth (h_2) as a function of In content for 6 ML and 15 ML $In_xGa_{1-x}As$ cap layer.

5.2 Surface chemical potential model

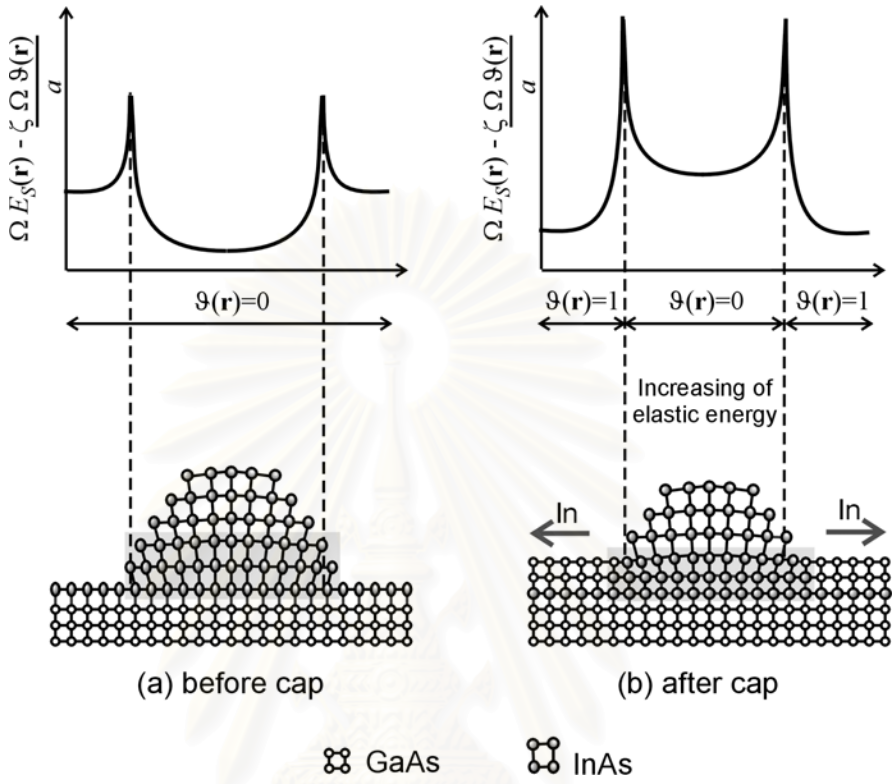

Figure 5.6 Schematic illustrations of the term $\Omega E_s(\mathbf{r}) - \frac{\zeta \Omega \vartheta(\mathbf{r})}{a}$ for (a) free- standing (b) partially capped InAs QDs with thin GaAs.

The experimental results in figure 5.5 reveal an important role of the In content of the $In_xGa_{1-x}As$ cap layer on the collapse of the dots. The material transport away from the InAs QDs is caused by a gradient of the surface chemical potential, which leads to the directional migration of adatoms on the surface. The influence of the cap layer on the In atom detachment from InAs QDs can be qualitatively described by a position-dependent surface chemical potential (Srolovitz, 1989; Ledentsov et al., 1996; Jesson et al., 1993; Xie et al., 1994).

The chemical potential, μ, of In atoms can be written as

$$\mu^{In}(\mathbf{r}) = \mu_0^{In} + \Omega E_s(\mathbf{r}) + \gamma\Omega\kappa(\mathbf{r}) \tag{5.1}$$

where μ_0^{In} is the chemical potential of In adatoms on an unstressed surface. The second term describes the contribution of the surface elastic energy, $E_s(\mathbf{r})$, to the chemical potential, with Ω being the atomic volume. The third term is the surface energy contribution, where γ is the surface energy per unit area and $\kappa(\mathbf{r})$ is the surface curvature. The deposited GaAs covering the InAs QDs and wetting layer affects the elastic energy of the dots and the surface energy surrounding the dots. Due to the lower surface energy of InAs compared to most GaAs surfaces (Wang et al., 2000), there is a general tendency of InAs to cover the GaAs surface. The surface chemical potential of In atoms on partially capped InAs QDs with GaAs can be modified to (Ledentsov et al., 1996)

$$\mu^{In}(\mathbf{r}) = \mu_0^{In} + \Omega \mathrm{E}_s(\mathbf{r}) + \gamma\Omega\kappa(\mathbf{r}) - \frac{\zeta\Omega\vartheta(\mathbf{r})}{a} \tag{5.2}$$

The last term modifies the chemical potential due to a wetting process, where ζ is the energy benefit due to the formation of a second wetting layer on the GaAs cap layer, a is the lattice parameter, and $\vartheta(\mathbf{r}) = 1$ on the GaAs surface and $\vartheta(\mathbf{r}) = 0$ on the InAs surface. This concept was supported by the calculation of the total free energy of partially capped InAs dots with GaAs, which revealed that the reduction of the total free energy is caused by the redistribution of InAs to form the second wetting layer which will be presented in the next section (Wang et al., 2001).

In our case, we assume that the local surface curvature remains unchanged when the dot is initially covered with a thin GaAs cap. We only consider the effects of the cap layer on the elastic energy and the energy benefit due to the wetting process on the chemical potential, i.e., $\Omega \mathrm{E}_s(\mathbf{r}) - \frac{\zeta\Omega\vartheta(\mathbf{r})}{a}$. For a free-standing InAs QD on an InAs wetting layer, $\vartheta(\mathbf{r}) = 0$ at every position and only the term $\Omega \mathrm{E}_s(\mathbf{r})$ needs to be considered. The elastic relaxation of the QD causes a high strain energy at the QD edge

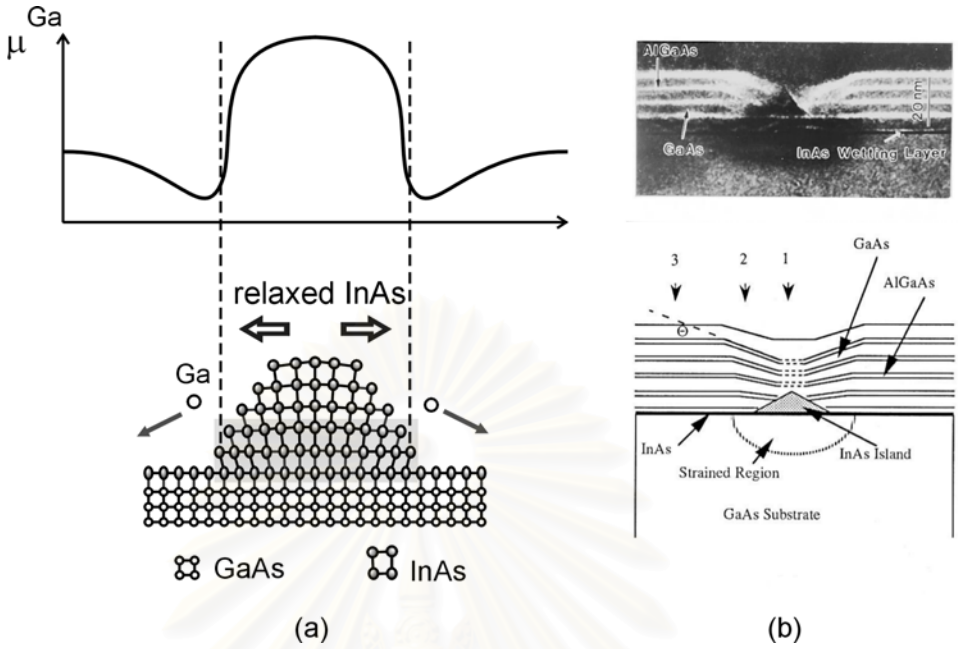

Figure 5.7 (a) Schematic illustrations of the chemical potential of Ga atoms during the overgrowth process for (b) the upper part shows TEM image show the tilted AlGaAs marker layer and the lower part schematically depicts the GaAs growth front evolution (Xie et al., 1994)

as shown in figure 5.6(a) (Chen and Washburn, 1996; Barabási, 1997). The situation is changed when the InAs QDs are overgrown with a thin GaAs layer as shown in figure 5.6 (b). The lower part of the dot becomes more compressed by the surrounding GaAs and consequently increases the surface elastic energy. It is plausible to expect the increase in strain energy at the edge of the partially covered InAs dot, which can cause In atom detachment (Barabási, 1997). The increase of the surface energy due to the surrounding GaAs layer also induces the detached In atoms to cover the thin GaAs cap layer surface. Hence, the change of the elastic energy and the surface energy during the overgrowth process cause the dissolution and the collapse of InAs QDs.

We point out that during GaAs overgrowth not only do the In atoms tend to move from the dot to the cap surface, but also the deposited Ga atoms prefer to migrate away from the top of the dots. This tendency was described by the gradient of the chemical

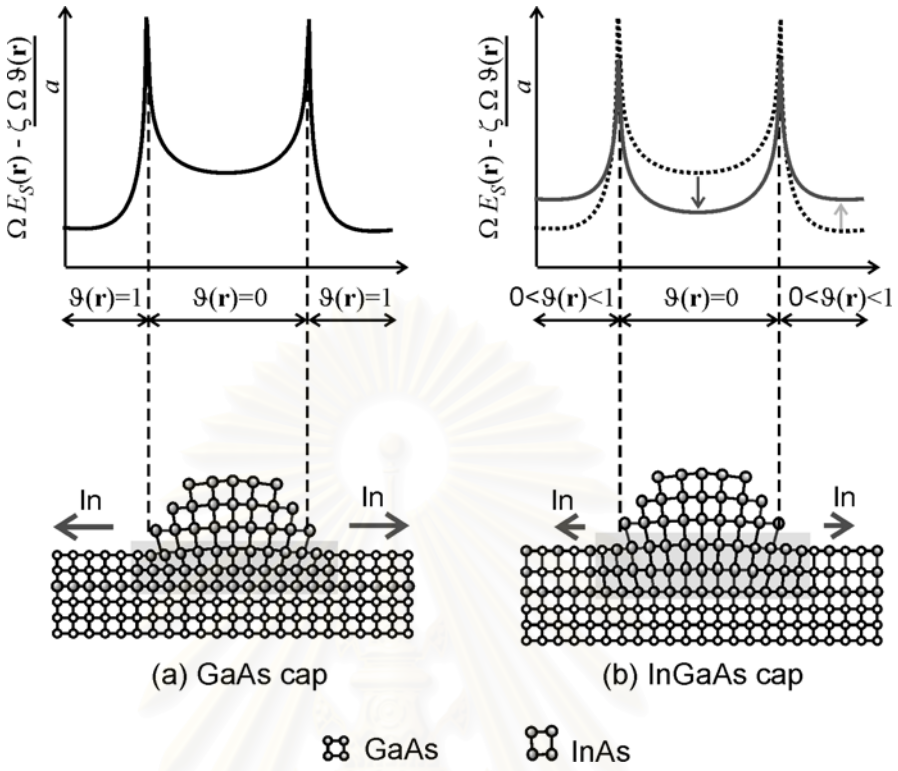

Figure 5.8 Schematic illustrations of the term $\Omega E_s(\mathbf{r}) - \frac{\zeta \Omega \vartheta(\mathbf{r})}{a}$ for partially capped InAs QDs with (a) thin GaAs (b) thin InGaAs.

potential of Ga adatoms due to both strain and surface curvature (Xie et al., 1994). Since at the top of the QDs was partially relaxed, the lattice mismatch between GaAs and InAs at the top of QDs is higher than that between GaAs and InAs at wetting layer where InAs is compressed by GaAs substrate. The strain profile modifies the chemical potential of Ga adatoms on surface as shown in figure 5.7(a), which induces the directional migration from the top of the QDs to the wetting layer region and hence reduces the growth rate of GaAs at the top of QD. This idea is supported by the TEM image in figure 5.7(b) which reveals the tilted of AlGaAs marking layer of the cap, confirming the lower growth rate at the top of the QDs. Xie et al (1994) suggested that the strain from the QDs plays a major role to the growth rate reduction at the top of the QDs. From our AFM results, we therefore deduce that the In atoms migration away from InAs QDs plus the unfavorable growth of GaAs on the top of InAs QDs cause the collapse of the dot and the ridge-valley structure formation, respectively.

When the overgrowth material was changed from GaAs to $In_xGa_{1-x}As$, the In content in the $In_xGa_{1-x}As$ cap layer affects both the elastic energy contribution and the energy benefit from the wetting process in eq. 5.2. By increasing the In content on the $In_xGa_{1-x}As$ cap layer, the lattice mismatch between the cap and the QD decreases, resulting in an elastic energy reduction. Moreover, the tendency of In atoms to cover the free cap surface decreases with high In content (we might estimate the effect of In content by interpolating $\vartheta(\mathbf{r})$ value between 0 and 1, depending on the In content). The $In_xGa_{1-x}As$ cap layer therefore decreases the In atom detachment rate and the migration of In atoms away from the QD to the cap surface. The schematic in figure 5.8 illustrates the effect of InGaAs cap layer to $\Omega E_s(\mathbf{r}) - \frac{\zeta\Omega\vartheta(\mathbf{r})}{a}$. As a consequence, the height of the InAs QDs during the overgrowth with $In_xGa_{1-x}As$ is partially preserved.

The effects of the elastic energy distribution and the energy benefit due to the second wetting layer formation on the chemical potential can qualitatively describe the overgrowth process of the large InAs dots by both GaAs and $In_xGa_{1-x}As$ at low temperature (460°C). In case of high temperature overgrowth at 500°C, we still observe the collapse of QDs but we do not find any ridge-valley formation and the saturated height in figure 5.5(b) is higher than for the low-temperature cap. We suggest that at high overgrowth temperatures, In-Ga material intermixing across the interface of the QDs with the cap layer occurs and causes the surface around the dot to incorporate a certain amount of In. The In rich surface reduces the In atoms outward migration, similar to the growth of the InGaAs cap layer. Hence, the height saturates at a larger value than for the low temperature overgrowth.

5.3 Thermodynamic model

The chemical potential model presented in the previous section can qualitatively describe the kinetic process during the overgrowth of InAs LGR QDs with GaAs. Another idea that can also explain the surface evolution of partially capped QDs is based on the consideration of the total free energy being a sum of elastic and surface energy (Wang et al., 2001). The total energy, E^{tot}, is a contribution of i) the elastic strain of the

pseudomorphic island and the surrounding substrate and capping layer, E^{Elast}, ii) the energy of the facets of the island and the interior walls of the hole, E^{surf}, and iii) the second wetting layer, E^{wl}.

$$E^{tot} = E^{elast} + E^{surf} + E^{wl} \tag{5.3}$$

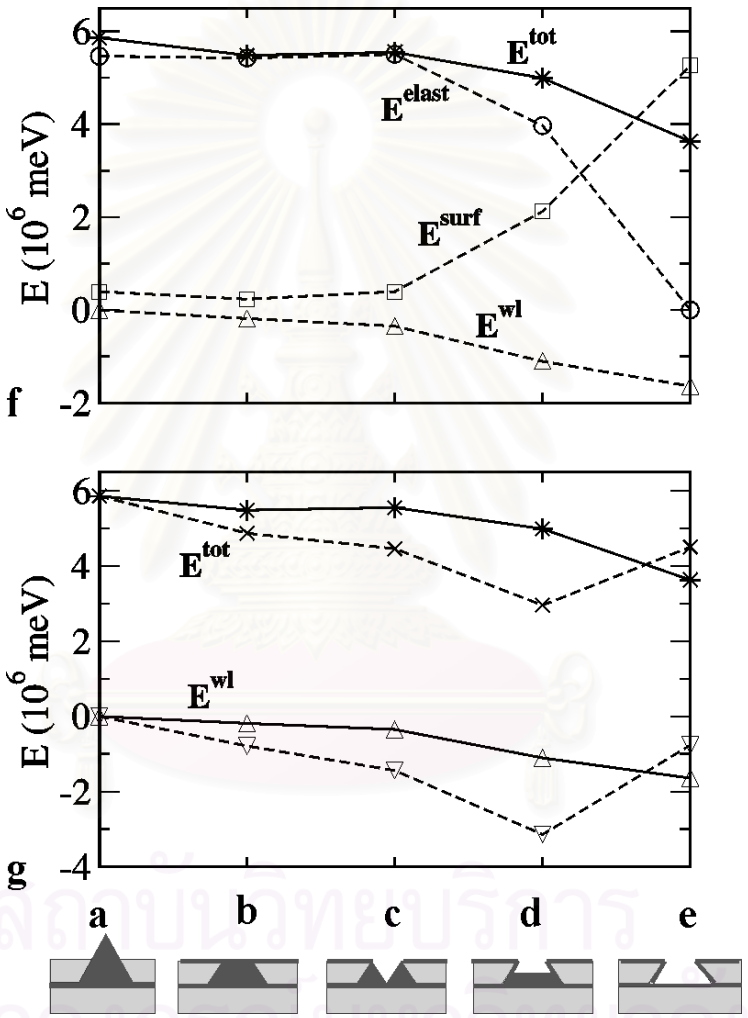

Figure 5.9 (a)-(e) Schematic of the transformation from a large InAs partially overgrown by a GaAs capping layer to a hole in five steps. (f) The energetic in for a density of partially covered island equal to 4.4×10^{9} cm^{-2} (g) The energetic for a density of 4.4×10^{9} cm^{-2} (solid line) compared with those for a density of 10^{10} cm^{-2} (dashed lines). (Wang et al., 2001).

From figure 5.9, their calculation shows that the elastic energy, E^{Elast} , relief favors island dissolution, since the buried part of the island is under compressive strain. The removal of the tip of the pyramid from figure 5.9 (a) to (b) leads to a reduction of the surface area. From the steps b to e, the surface area of the pure InAs facets and the interior walls of the whole increases, and thus E^{surf} increases again. The wetting layer contribution arises from the difference in the surface energies of GaAs and InAs. The redistributed InAs on GaAs decreases the surface energy of the system. Hence, the sum of the contributions indicates that the dissolution for the island and hole formation is energetically favorable. From this calculation, they found out that the total energy followed the tendency of E^{wl}. They also suggested that the wetting effect plays a key role in island dissolution. This thermodynamic model is consistent with the chemical potential model, which suggests the outdiffusion of InAs from the QDs during GaAs overgrowth process.

5.4 Effect of the overgrowth condition to the photoluminescence of InAs QDs

QDs lasers have been thoroughly investigated due to their predicted improved operating temperature and ultra low power consumption. The achievement of GaAs-based structures emitting light at the range 1.3 μm and 1.55 μm is a major challenge since these wavelengths are the suitable for optical telecommunication systems. There are reports of successful extension of the emission wavelength into the 1.3 μm regime by overgrowing QDs grown at a growth rate 0.1 ML/s with InGaAs layer (Tatebayashi et al., 2001; Wang et al., 2000; Wang et al.; 2001). In this section, we investigated the effects of the overgrowth process on the optical properties of the LGR InAs QDs and the role of overgrowth temperature on the large and small QDs.

5.4.1 GaAs overgrowth

After InAs QDs were grown at 500°C at a rate of 0.01 ML/s, the substrate temperature was ramped down to 430°C-470°C and 300 sec-GI is inserted, followed with 6 ML of GaAs deposition at the temperature ranging from 430°C to 500°C. The

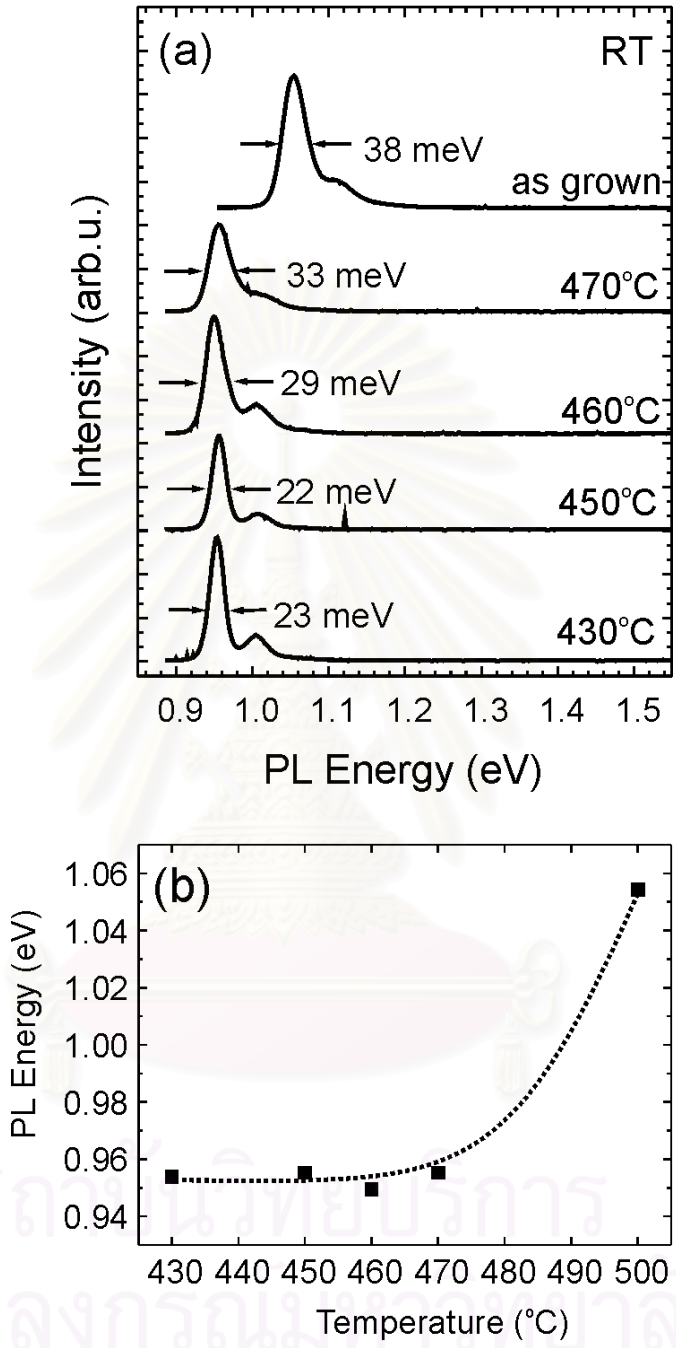

Figure 5.10 (a) PL spectrum of InAs QDs capped with GaAs at different temperature (b) PL peak as a function of the growth temperature of GaAs cap layer.

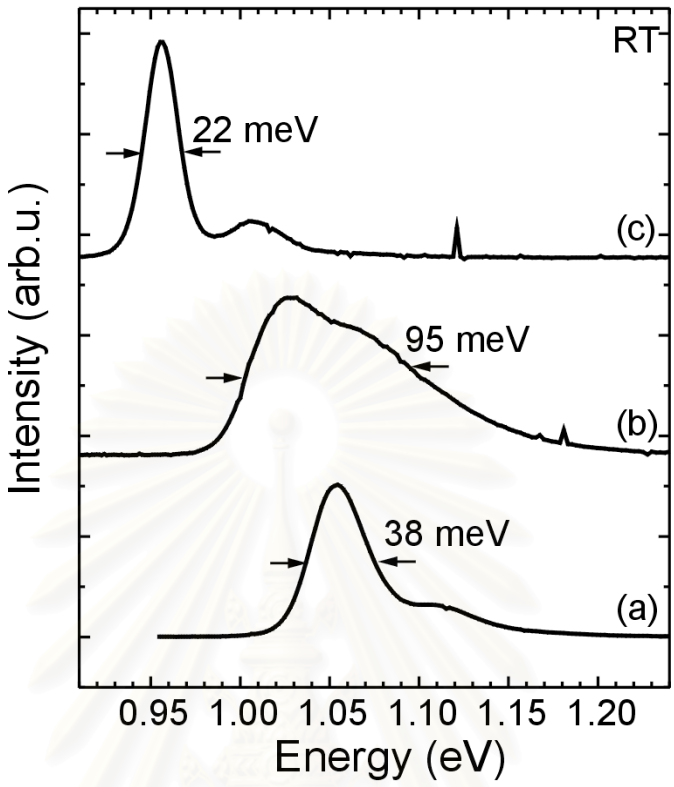

Figure 5.11 PL spectrum of InAs QDs capped with GaAs at (a) 0.6 ML/s at 500°C (b) 0.1 ML/s at 450°C and (c) 0.6 ML/s at 450 °C

substrate temperature was increased to 500°C during the deposition of the remaining GaAs layer. In the case of GaAs overgrown at 500°C, the 300 sec GI was removed to prevent In desorption. PL spectrum and the summary of the peak and FWHM with substrate temperature are shown in figure 5.10. The PL peak red shifts from 1.054 eV to 0.949 eV and then saturates when the growth temperature of GaAs cap is decreased to 470°C. While the FWHM continually decrease from 38 meV to 22 meV when the T_{cap} reaches 450°C.

Figure 5.11 shows the comparison between the PL spectra from different overgrowth processes (a combination between different growth rate and substrate temperature) during the overgrowth. The spectral result in (a) is obtained by overgrown QDs at 500°C at a rate of 0.6 ML/s, where the peak locates at 1.054 eV with 38 meV

linewidth. Spectra (b), the growth rate of GaAs cap is 0.1 ML/s but the substrate temperature decreases to 450°C, we obtain the PL peak at 1.028 eV with a 95-meV linewidth. If we change the growth rate of GaAs cap layer to 0.6 ML/s at 450°C, the peak shifts to 0.949 eV with 22 meV linewidth. The red shift and the linewidth narrowing by low temperature-capping process and high growth rate can be explained by the suppression of In segregation during the overgrowth process.

It is widely recognized that, indium segregates during the growth of InGaAs/GaAs QW which is the ultimate limitation to the building of abrupt interfaces. This limitation is evident from the optical properties of the QW. As described by Dahaese et al. (1995) and Grandjean et al. (1996) that in the temperature range of the III-V MBE growth, the bulk diffusion can not be effectively be operative. Therefore, atomic rearrangement, leading to indium segregation during the epitaxy, is a surface or a near-surface process. This can be seen as an exchange reaction between the substrate, the epilayer and the impinging atoms. The segregation process is kinetic process, which is at maximum at thermodynamic equilibrium and is possible to reduce by keeping the system away from the equilibrium by means of decreasing substrate temperature or increasing growth rate. We can simply provide a quantitatively idea of the relationship between the In segregation and the growth rate and the substrate temperature of the cap layer. The model we used is the simple kinetic model assuming that the exchange of In and Ga atoms occurs only between the first two monolayers. The details of the model are described by Dahaese et al. (1995).

Figures 5.12(a) and (b) are the In concentration profile evolution with different growth temperatures and growth rates, respectively. Parameters in our calculation are that the 2-ML InAs are grown at 500°C with 0.01 ML/s and the 30 ML GaAs cap layer is deposited at different conditions. The calculation excludes the desorption of In atoms at 500°C. Even though these profiles are not the profile from the QDs structure but from the 2 ML InAs QW structure, they provide an idea of the In segregation depending on growth rate and substrate temperature. From the calculated profile, at substrate temperature equal to 450°C, the In segregation is enhanced when GaAs growth rate is 0.1 ML/s. If the growth rate was kept at 0.6 ML/s, the substrate temperature equal to 500°C would cause more segregation. The calculation results are consistent with the experimental results

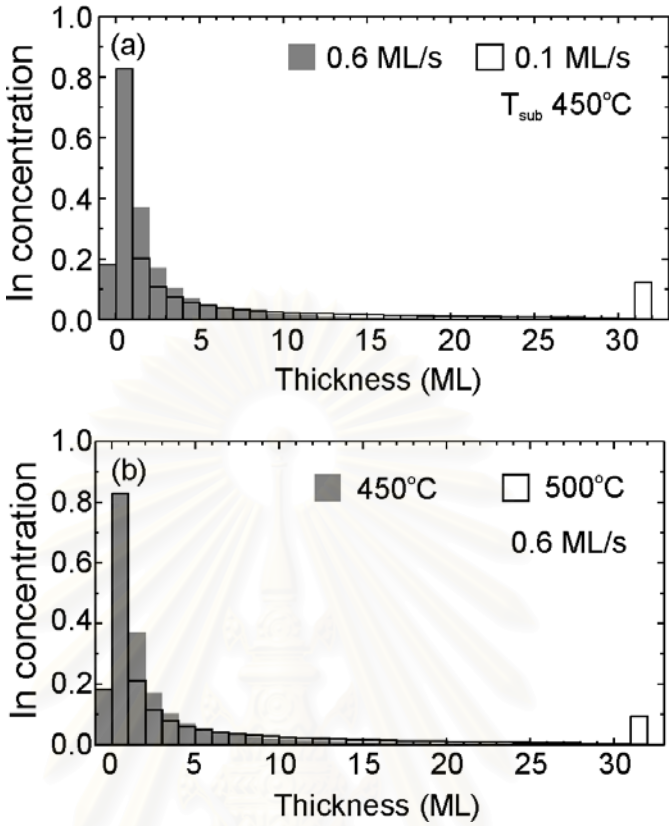

Figure 5.12 Indium concentration profile evolution of GaAs/InAs 2 ML grown at 500°C and covered with 30 ML GaAs (a) grown at 450°C with 0.1 and 0.6 ML/s and (b) grown with 0.6 ML/s at 450°C and 500°C

that the segregation is enhanced by low growth rate and high growth temperature of GaAs overgrowth layer, resulting in the blue shift of the PL spectrum.

5.4.2 InGaAs overgrowth

From the previous experiment, we can extend the emission wavelength from the large InAs QDs, which are capped with GaAs by suppressing the In segregation in GaAs layer. Low substrate temperature overgrowth and high GaAs growth rate successfully provide 1.3 μm emission with a narrow linewidth. By using GaAs matrix, it is difficult to extend

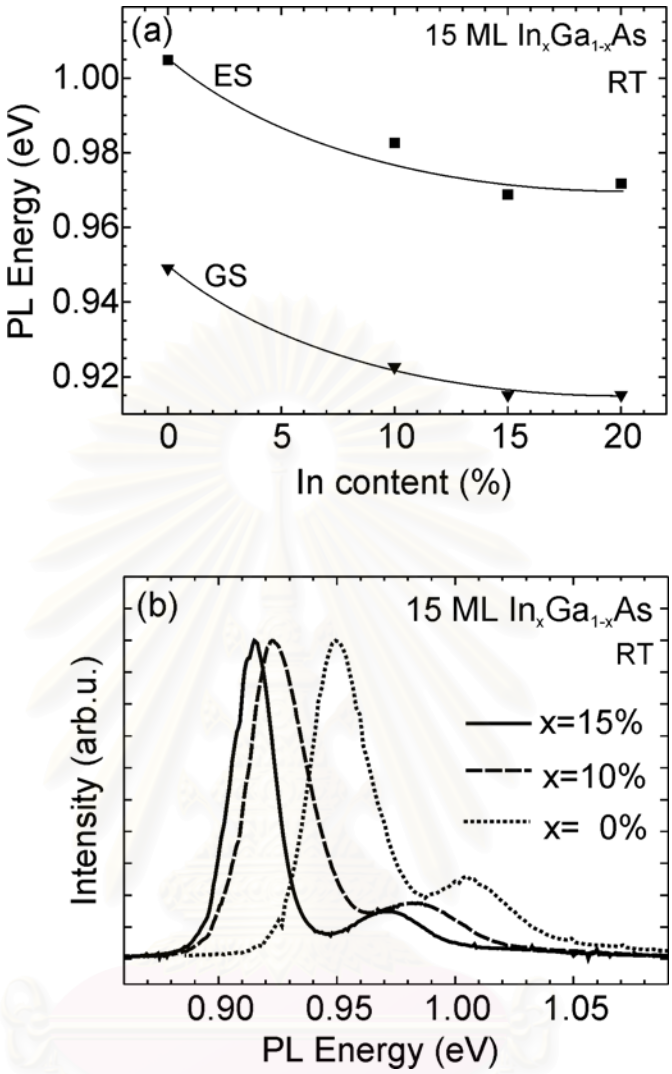

Figure 5.13 (a) The PL peaks of the ground state (GS) and excited state (ES) of LGR InAs QDs overgrown with 15 ML $In_xGa_{1-x}As$ as a function of In content. (b) PL spectrum with normalized intensity.

the emission wavelength beyond 1.3 μm, though there is a report from da Silva. et al. (2003) that they can tune the emission wavelength to 1.3-1.5 μm by using extremely low growth rate (0.003 ML/s). However, the PL intensity is deteriorated. By using the $In_xGa_{1-x}As$ strain-reducing layer, several groups succeed to extend the emission wavelength from small InAs QDs to 1.3-μm. The InGaAs layer decreases the barrier around the dot, decrease the strain between the matrix and the QDs and also suppresses

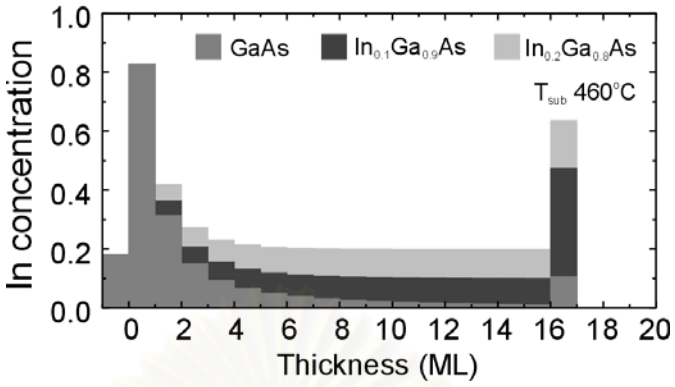

Figure 5.14 Indium concentration profile evolution during overgrowth 2 ML InAs with 15 ML of $In_xGa_{1-x}As$ by using different content.

the In segregation. We therefore apply this technique to InAs LGR QDs to extend the emission wavelength beyond 1.3-μm regime.

Figure 5.13 is the summary of PL peak position of the ground state and the excited state with 15 ML of $In_xGa_{1-x}As$ and PL spectrum with normalized intensity. PL ground state peak red shifts with In content from 0.949 eV to 0.915 eV and the separation between ground state and excited state is constantly equal to 65 meV, implying that the $In_xGa_{1-x}As$ does not affect on the separation between the two states. With In content larger than 10%, the PL intensity is drastically reduced. We attribute the deterioration of the crystal quality to the large amount of In causing highly strain and introducing the dislocations to the experimented samples.

Figure 5.14 is the gradient of In composition of 2 ML InAs covered with 15 ML $In_xGa_{1-x}As$ with the different *x* calculated by the same model as those used in figure 5.11. The $In_xGa_{1-x}As$ cap was overgrown at 460°C with a growth rate of 0.6 ML/s. The gradient clearly shows that InGaAs cover layer suppress the In segregation from the InAs layer the cap layer. From AFM measurement, the height preservation of the QDs is also observed. However, from PL results in figure 5.15(a), the PL peak is saturated at 0.910 eV when the In content is larger than 15%. This can be explained by the formation of the small dot in between the large dot when the In content in InGaAs layer reaches 20% as shown in AFM results in figure 5.3, hence the strain reducing layer can not cover the QDs and can hardly suppress the In segregation.

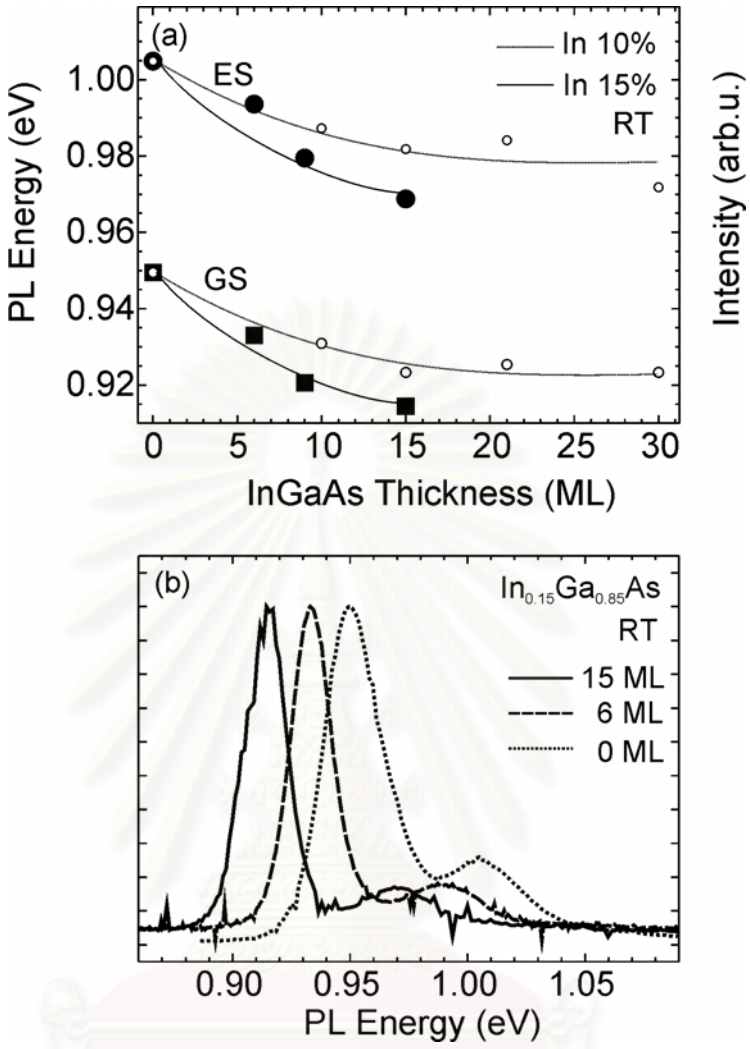

Figure 5.15 (a) The PL peaks of InAs QDs overgrown with $In_{0.1}Ga_{0.9}As$ and $In_{0.15}Ga_{0.85}As$ as a function of thickness. (b) PL spectrum with normalized intensity.

If the thickness of $In_xGa_{1-x}As$ with x=10% and 15% was changed from 0-30 ML, PL peaks red shifted with the increasing in InGaAs thickness since the InGaAs layer could not cover QDs and thus GaAs barrier could affect the structural properties of QDs. Figure 5.15(a) reveals that for *x*= 10% when the InGaAs exceed 15 MLs, the PL peak is saturated and the intensity drastically decreased. In the case of x=15%, the PL signal from the structure can not be obtained.

5.4.3 In-Ga intermixing effect on PL spectrum of large and small dots

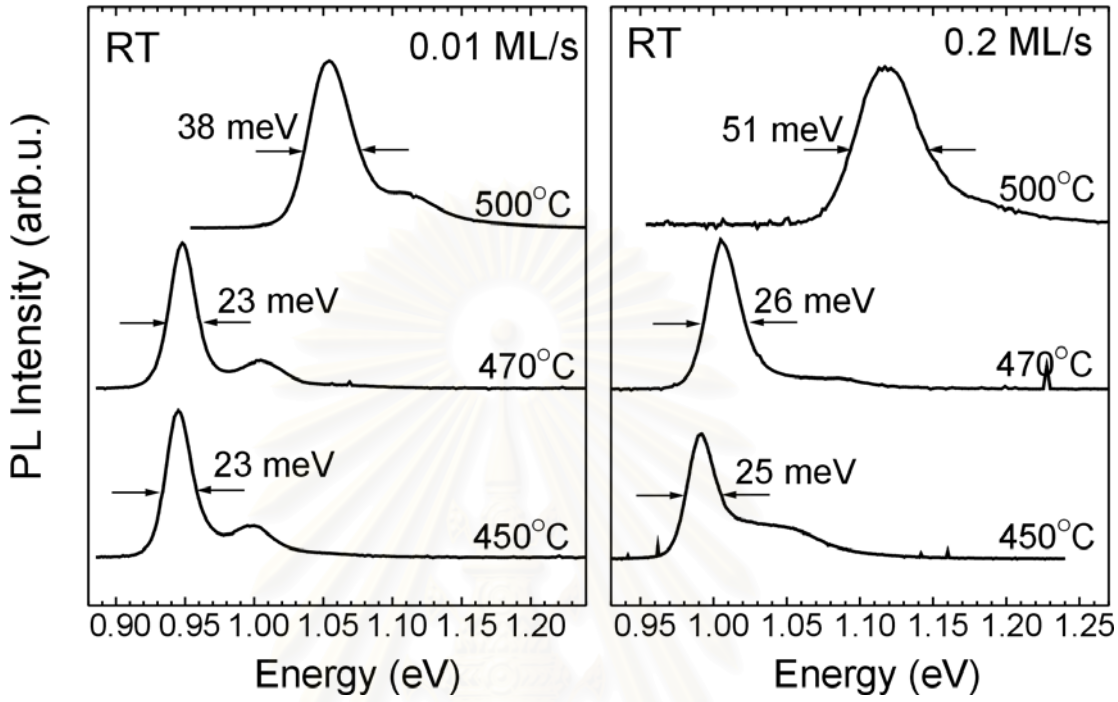

Figure 5.16 Room-temperature PL spectra of InAs QDs grown at InAs growth rates of 0.01 ML/s and 0.2 ML/s overgrown at different substrate temperature.

Since the In segregation strongly affects properties of QDs, in this experiment the segregation process in different QD types is comparatively studied by PL measurement. Figure 5.16 shows comparative room-temperature PL spectra QDs grown at growth rates of 0.01 ML/s and 0.2 ML/s overgrown at 450-500°C. At the overgrowth temperature equal to 500°C, the PL peaks located at 1.054 eV and 1.117 eV for the 0.01 and 0.2 ML/s, respectively. When the overgrowth temperature was decreased to 450°C, the PL peaks red shifted to 0.945 eV and 0.992 eV, indicating a clear redshift of 109 meV and 125 meV for large and small dots, respectively. Furthermore, the linewidths decreased from 38 and 51 meV to 23 and 26 meV with decreasing overgrowth temperature. We attribute the redshift and the linewidth narrowing mainly to the suppression of In segregation during the GaAs overgrowth at low temperature (Kiravittay et al., 2001; Schmidt et al. 2002; Eberl et al., 2001). In addition, TEM measurement show that the low

temperature overgrowth can preserve the shape of the QDs (Eberl et al., 2001). The PL results reveal that the In segregation has a strong effect on the small QDs. We explain this circumstance by the higher ratio of the surface area to the volume of small dots since the segregation process removes material from the surface.

Chapter 6

Self assembled nanohole

Heteroexpitaxial growth of highly strained structure has gained much interest as it offers the possibility to create dislocation free nano-islands. The island formation occurs due to strain relaxation during the deposition of lattice mismatched material. After the islands grow over a certain critical size, misfit dislocations form to relieve the strain energy in the system. It is shown that when the islands are overgrown, the strain plays an important role in the surface evolution of the overgrowth layer and the island shape itself as discussed in chapter 5. Moreover, the buried islands induce a spatial strain modulation on the surface of the cap layer, which is responsible for the uniform size and the vertical alignment of multi-stacked structure. In some material systems, the strain fields also provide a possible route to create lateral ordering of islands (Springholz et al. 2001). Hence, the strain is a crucial parameter in the formation of the self-assembled nanostructure.

In this work, the strain field in the GaAs cap layer created by buried InAs QDs are utilized as a self-patterning to create new structures. Schuler et al. (1998) reported the realization of holes on GaAs cap layer by *in situ* etching process. The strain modulation from buried InAs QDs locally enhances the etching rate of GaAs, inducing hole formation. However, these results show inhomogeneous holes which are probably due to the high density and inhomogeneity of the initial InAs QDs grown by using high growth rate. This research work focuses on nanohole fabrication, which utilizes the large InAs QDs as an initial template for the hole creation. The large QDs with low density are supposed to provide the higher and non-overlap strain field which might improve the uniformity of the holes structure. Due to the nanometer-size of holes obtained by this technique, we therefore name the investigated structure as **nanohole**.

This chapter presents the details of the nanohole realization process. The GaAs cap layer thickness and the etching time (the nominal etching depth) were systematically varied to study the nanohole formation by using AFM and PL characterization. The stability of the nanohole was studied by *in situ* annealing experiment.

6.1 Nanohole fabrication process

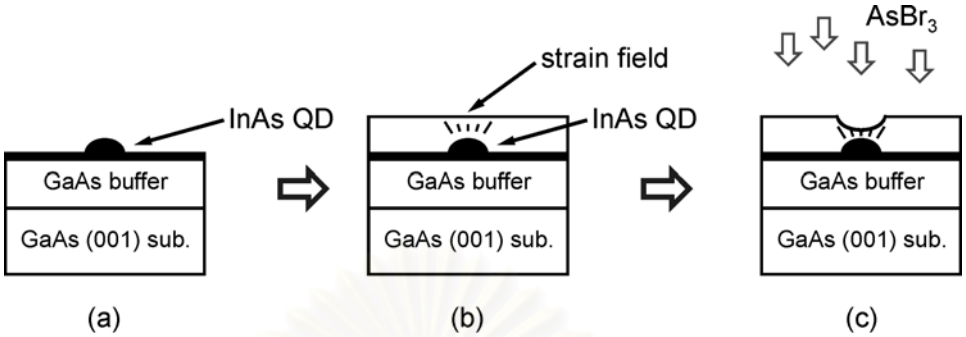

Figure 6.1 Schematic illustration of the nanohole fabrication process (a) initial InAs QDs, (b) overgrowth of InAs QDs with GaAs and (c) the nanohole formation by supplying the $AsBr_3$ *in situ* etching gas on to GaAs cap layer.

Figure 6.1 illustrates the details of nanohole fabrication process. After 0.4 μm GaAs buffer growth, 1.8 ML InAs QDs were grown at T_s = 500°C using a very low indium growth rate of 0.01 ML/s. A 30 s growth interruption was introduced in order to improve the size homogeneity (Kiravittaya et al., 2001). The substrate temperature was decreased to 470°C and the GaAs layer was subsequently deposited to cover InAs QDs layer, followed by the etching process by introducing the $AsBr_3$ *in situ* etching gas to the growth chamber. The etching rate is 0.24 ML/s for the GaAs and the substrate temperature was kept at 500°C which is in the supply rate-limited region as described in chapter 2. In this experiment, the GaAs cap layer thickness and the amount of $AsBr_3$ were systematically varied. For PL measurement, the nanoholes were covered by GaAs grown at 500 °C

6.2 Nanohole formation

Figure 6.2 shows selected AFM images of self-assembled nanoholes fabricated by supplying the $AsBr_3$ etching gas onto 10-nm GaAs layer. After covering InAs QDs

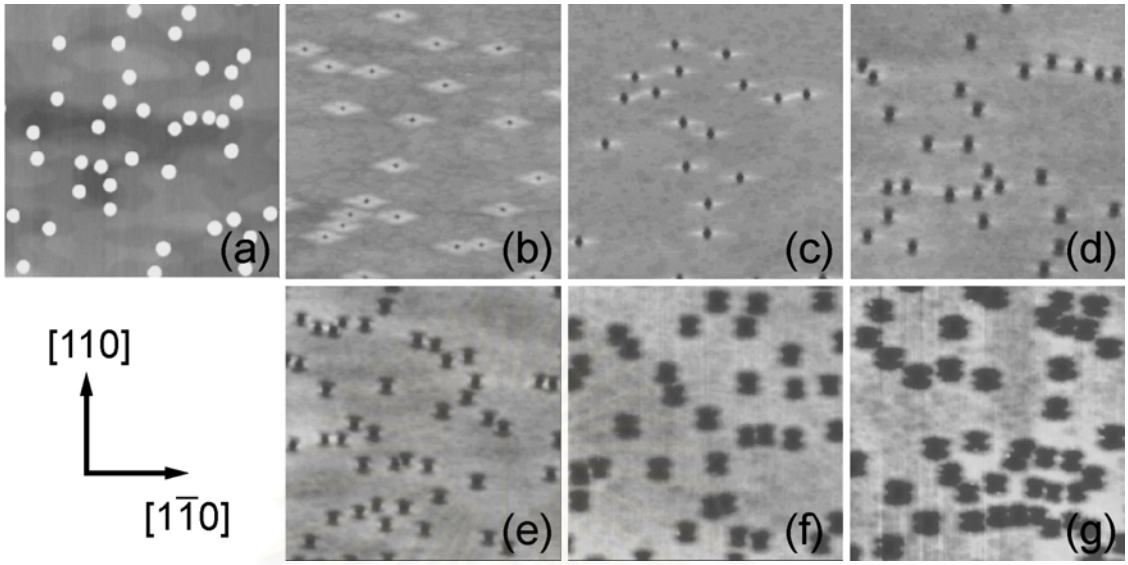

Figure 6.2 1×1 μm^2 AFM images of surface evolution during the nanohole fabrication process. (a) 1.8 ML InAs QDs (b) the rhombus structure obtained by 10 nm GaAs overgrowth. The nanohole structure obtained by different nominal etching depth (c) 1 nm, (d) 3 nm, (e) 5 nm, (f) 8 nm and (g) 10 nm

shown in figure 6.2(a) with 10 nm of GaAs layer, the rhombus-shaped structure with a tiny hole at the center was obtained (figure 6.2(b)). The GaAs surface morphology of the cap layer changes when $AsBr_3$ etching gas is supplied to the sample surface. With increasing the nominal etching depth, the holes at the center of rhombus structure increase in both depth and diameter as shown in figures 6.2(c)-(d), and then the hole shape transforms to the bow-tied shape hole (figure 6.2(e)). The AFM images in figure 6.2(f) and (g) reveal that with increasing the nominal etching depth beyond 5 nm, the hole depth is preserved while the diameter significantly increases. Moreover, the etched surface becomes rougher with increasing the etching time. The formation of the bow-tie-shaped holes is attributed to the anisotropic initial rhombus structures and an anisotropic etching rate (Schuler et al., 2000).

The average hole depth and diameter in [110] direction were obtained from AFM images and plotted as a function of nominal etching depth in figure 6.3(a). The

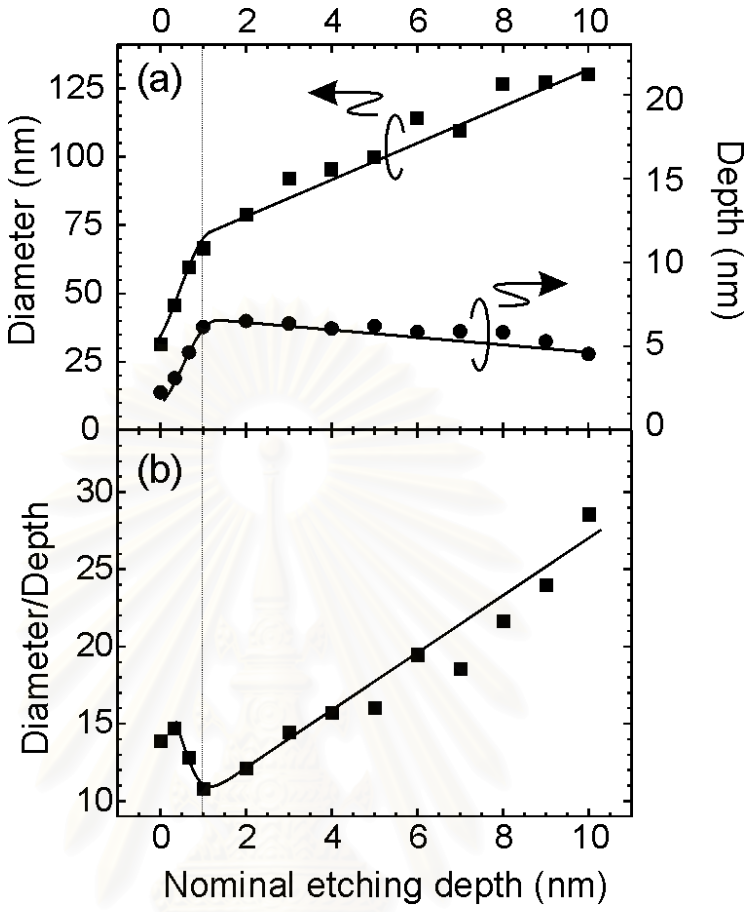

Figure 6.3 (a) The average depth and diameter in [110] directions versus nominal etching depths. (b) Ratio between average diameter and depth as a function of nominal etching depth. Note that the depths are measured from the vertical distance between rims along [110] direction and the bottom of the holes.

ratio between depth and diameter versus nominal etching depth is shown in figure 6.3(b) The etching mechanism can be divided into two distinct regimes. In the first regime where nominal etching depths is equal or less than 1 nm, the diameter and the depth increase with the nominal etching depth, but the ratio between diameter and depth decreases. If the etching gas is further supplied, we enter the second regime where the holes mainly increase in diameter but the depth slightly decreases. The ratio between the diameter and the depth follow the tendency of the diameter increment. In this second

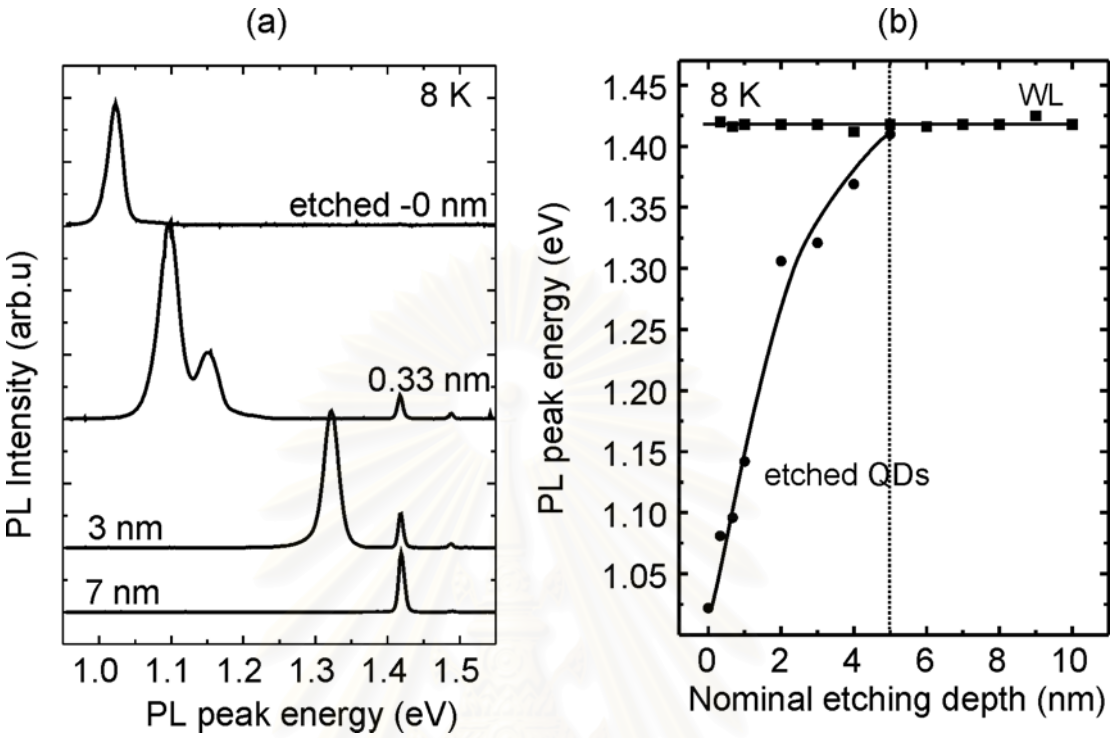

Figure 6.4 (a) Low temperature PL spectra during nanohole fabrication process. The peaks at lower energy come from the remaining buried InAs QDs. (b) The summary of the PL peak energies as a function of nominal etching depth.

regime, the holes transforms from a rhombus-like structure with a small hole in the middle to a bow-tie- shaped structures.

To understand more about the etching mechanism, the etched structures are overgrown with GaAs to record the PL of the remainders of the QDs. The PL spectra and the summary of PL peak energy at 8 K versus the nominal etching depth shown in figure 6.4 show a systematic blue shift of the QD-related peak. The initial peak of 1.8 ML of InAs QDs is located at 1.022 eV. After a 0.33 nm nominal etching depth, the peak shifts to 1.081 eV and further to 1.320 eV when the etching depth reaches 3 nm. The blue shift of QD related peak is the evident that the etching gas removes the material from the QDs, causing the decrease of the dot size. The peak disappears after 5-nm nominal etching depth, implying that the InAs material is completely removed. The energy

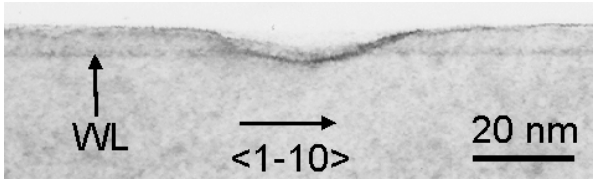

Figure 6.5 TEM image of a hole fabricated by 10-nm GaAs capping and 5-nm nominal etching.

of the signal at 1.412 eV from the initial wetting layer remains unchanged during the whole etching procedure. It is noteworthy that the PL linewidth of the buried QDs during the etching process is in the range of 24-40 meV, implying that the dots were uniformly etched by $AsBr_3$.

In order to confirm the AFM results, cross-sectional TEM was performed. The TEM image of a hole fabricated by a 10-nm GaAs cap layer and 5-nm etching is shown in figure 6.5. The depth and diameter measured from the figure are ~ 6 nm and 50 nm measured in [1-10] direction, respectively. The hole shape and size agree well with AFM investigation. TEM image reveals that the underlying InAs QD has been etched away completely, while the initial wetting layer (WL) is still present. Moreover, we found that the remaining GaAs on the WL is ~5.3 nm thick. This is due to the fact that the etching process is in the supply rate-limited region, hence, the enhanced etching rate on the area around the top of the buried QDs causes a reduction of the etching rate on the flat surface. The TEM results greatly agree with the PL results that at 5-nm nominal etching depth, the QDs related peak disappear and only the WL peak remains.

In case of the 15-nm GaAs cap layer, the initial surface is the ridge valley structure as shown in figure 6.6(a). The rhombus like structure forms with a tiny hole in the middle of the structure when the supplied $AsBr_3$ equal to 1-nm nominal depth (figure 6.6(b) transforms to the bow-tied shaped holes after 3 nm-nominal etching depth was supplied (figure 6.6(c)). The depth evolution during the etching process of different cap thicknesses as a function of nominal etching depth is shown in figure 6.7. The etching of the holes can be divided into two regimes similar to the case of the 10-nm GaAs cap. The transition from the first regime, occurs at a nominal etching depth of about 4 nm. Whereas the hole depth of the 10-nm capped samples saturates at a constant value of

about 6 nm after a nominal etching depth of 1 nm, the 15-nm capped structure shows a more gradual increase of the hole depth up to 4 nm.

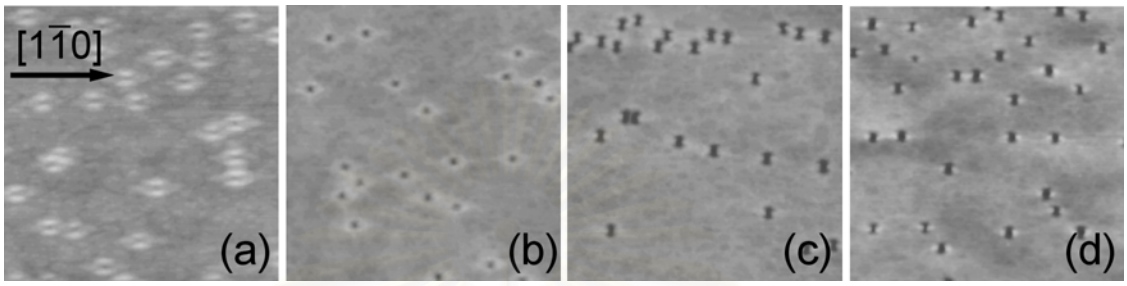

Figure 6.6 1×1 μm^2 AFM images of surface evolution during the nanohole fabrication process by using GaAs cap thickness equal to 15 nm. The nanohole structure obtained by different amount of nominal etching depth (a) 0 nm, (b) 1 nm, (c) 3 nm, and (d) 5 nm.

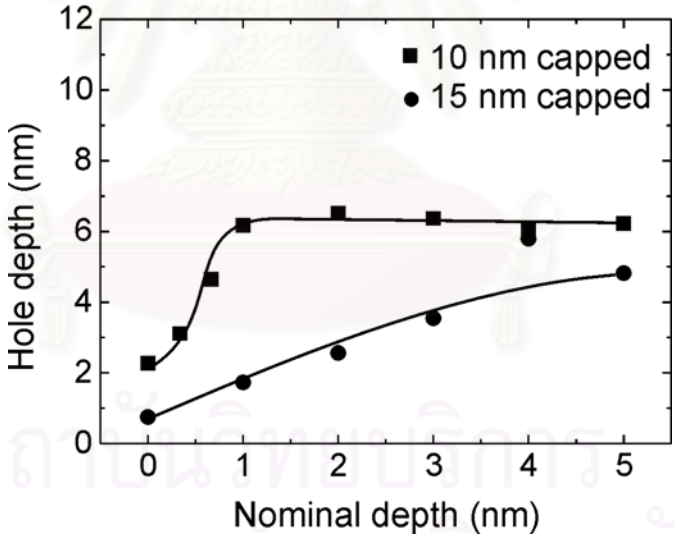

Figure 6.7 Average hole depths versus nominal etching depth for 10 nm (■) and 15 nm (●) GaAs capped.

6.3 Nanohole formation mechanism

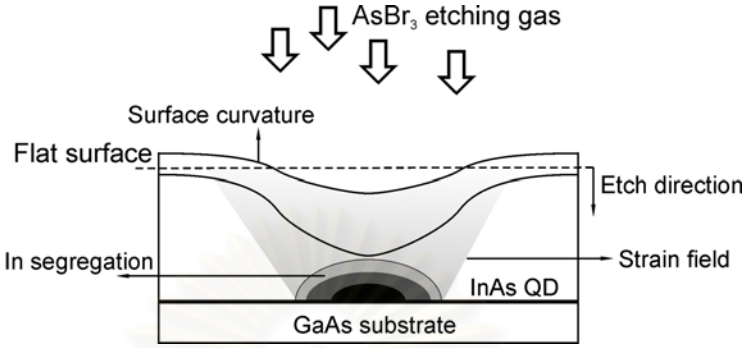

Figure 6.8 Schematic illustration of the possible parameters which lead the nanohole formation i.e. the material selectivity of the etching gas due to In segregation, the strain field from the buried InAs and the surface curvature of the etched front.

Kim et al. (2002) proposed a model of the etching reaction between the solid and etching gas interface that the etching speed is directly proportional to the chemical potential on the surface, which is contributed by the surface curvature term (which is related to the surface energy) and the strain energy term as described in chapter 5. We therefore applied this model to qualitatively explain the *in situ* etching mechanism. In our experiment, there are three possible parameters which are attributed to the evolution of the surface morphology during the etching process. First, material selectivity of the etching gas on the etched surface due to the In segregation from InAs QDs to GaAs cap layer. Second, the surface curvature of the etched front which can modify the chemical potential. Third, the strain contribution term which affects atomic bonding of the etched material. All parameters are depicted in the schematic shown in figure 6.8

Material selectivity

Schuler et al. (1998) reported material selectivity of the $AsBr_3$ etching gas that the etching rate of InAs is 1.24 times higher than that of GaAs at the supply rate limited

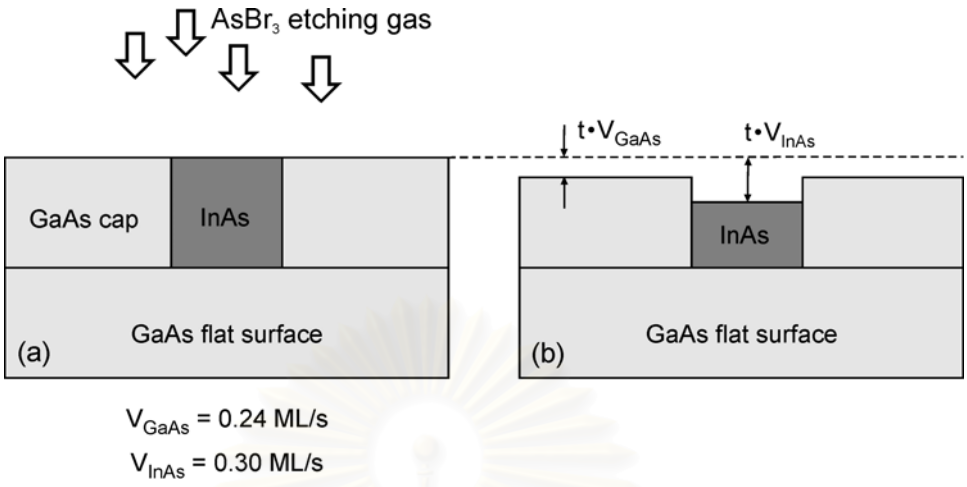

Figure 6.9 The simplified picture of the material selectivity mechanism. Assuming that In segregation process cause the uniform In-riched profile with In content 100% above QDs. (a) before etching process (b) after etching process for time *t*.

regime. The etching rate of InGaAs can be linearly interpolated from these two values. For the first regime where the hole depth and diameter rapidly increase, if we consider for the extreme case that the In segregation causes the In rich region above the QDs as shown in the simplified schematic in figure 6.8(a), the results can not provide a good explanation for the nanohole formation. For example, for the 1-nm etched sample with the 10-nm GaAs cap layer, the average hole-depth is 6 nm. This result means that the etching rate above the QDs is 6 times higher than the etching rate on the flat surface, which cannot be fully explained by the material selectivity of the etching gas.

Strain energy contribution

Assume that the initial etched front is completely flat and no In segregation process occur, the etching mechanism can simply be drawn as shown in figure 6.10. To understand the effect of the strain energy, the simple normalized strain energy distribution of the island in the isotropic elastic medium by approximating the island as a point-like source as proposed by Springholtz et al. (2001) is plotted in figure 6.10(b).

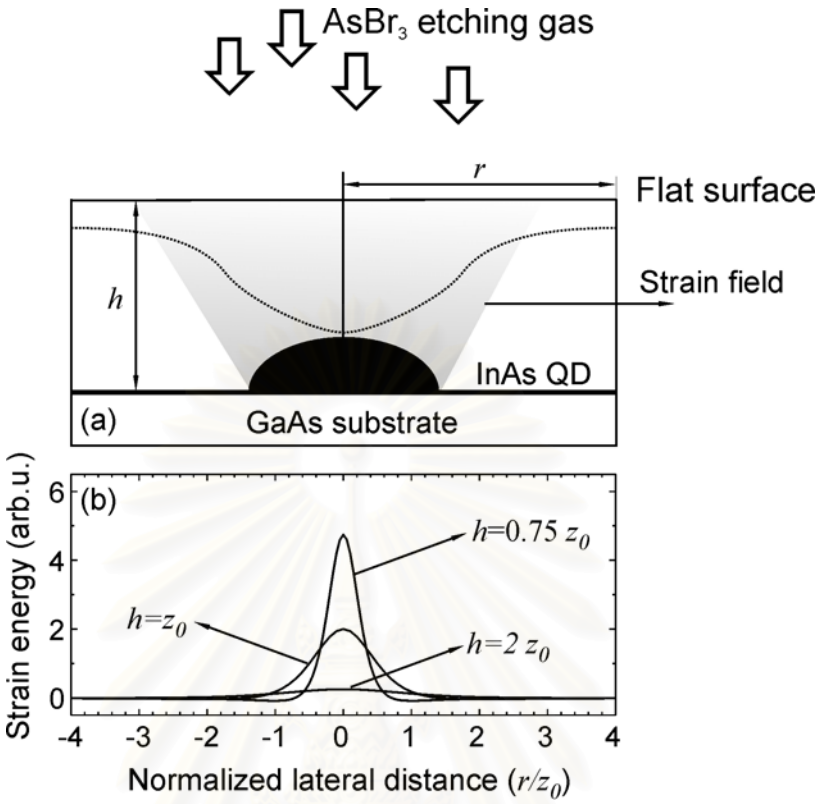

Figure 6.10 (a) Schematic illustration of the strain field in the strain field in GaAs cap layer which enhances the etching rate of GaAs. (b) The radial strain energy distribution on the cap layer with different cap thickness (*h*) (Springholtz et al. (2001).

Since InAs at the QDs are more relaxed compared to the wetting layer region, the GaAs cap layer above the QDs thus experience tensile strain which induces a higher strain energy. As a consequence, $AsBr_3$ etching gas can remove the material from those positions easily and originate the nanohole structure. Since the strain energy decrease as a function of the distance (Yu et al., 2001; Daruka et al. 1999), when the cap layer thickness increases, the strain enhancing mechanism is not strong. The gradual increase of the hole depth in the case of 15 nm cap thickness is a clear evident of the strain reduction with the cap thickness.

Surface curvature contribution

At an early stage of the etching process, the etched surface can be approximated as a flat surface, therefore the surface curvature can be neglected. When the nanohole forms, the surface curvature of the etched front starts to play a role on the etching mechanism. From Jesson et al. (1993), the surface curvature can be calculated by $\kappa(\mathbf{r}) = -\frac{h''(x)}{[1+(h'(x))^2]^{-\frac{3}{2}}}$, where $h(x)$ is the height of the surface at lateral position.

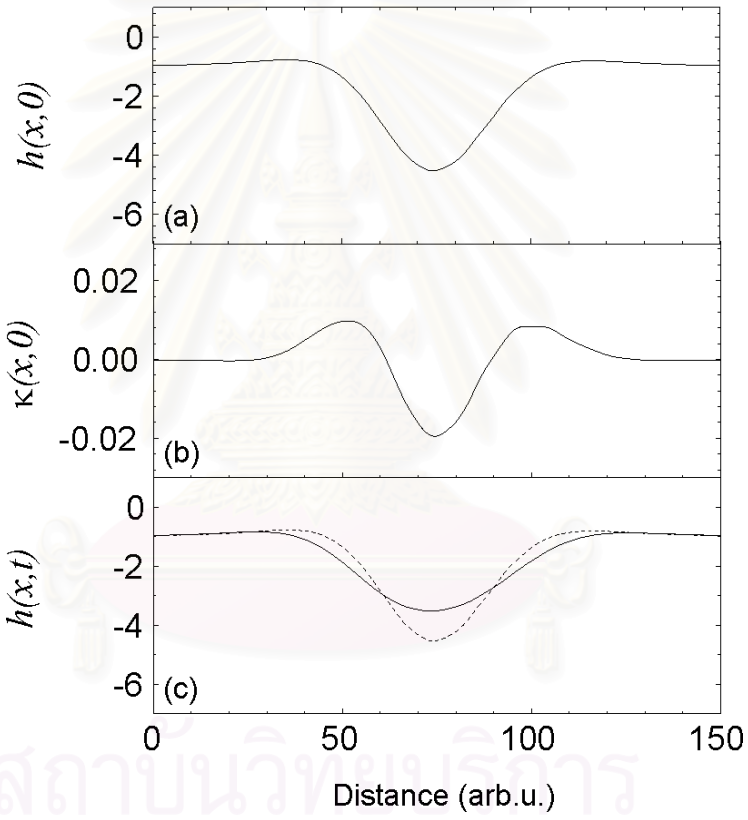

Figure 6.11 (a) The hole structure (b) the corresponding hole curvature and (c) the surface evolution after time t by assuming the etching process is proportional to the curvature (dotted line represent the initial hole in figure 6.11(a)).

The plot of the concave curve which represents the hole structure with its corresponding curvature is shown in figure 6.11. Kim et al (2001) proposed that the etching rate is proportional to the chemical potential, therefore, the etching gas would prefer to flatten the surface which results in the widen of the hole diameter during the etching process. From experimental results, the second regime shows the slightly decreasing of the hole depth and the continuous increase of the hole diameter with a slower rate compared to the first regime, therefore, the etching mechanism is expected to be different. In addition, the PL peak evolution shown in figure 6.4 which show the systematically blue shift with increasing of the etching depth, implying that the material from the buried InAs QDs was taken away by etching gas, as a consequence the strain from the buried dots was reduced. We, therefore, draw a conclusion from AFM and PL results that the etching mechanism in the second regime is due to surface curvature contribution. In other word, atomic bonding of the material at the hole edge is weaker compared to other places, thus the $AsBr_3$ etching gas can preferentially remove atoms at those positions.

In conclusion, we qualitatively describe the etching mechanism using the chemical potential concept. In the first region, where the depth and diameter increase rapidly, the strain enhance etching rate is the dominant mechanism which is responsible for the origin of the nanoholes. In the second region, where the depth shows the saturation while the diameter still increases, the curvature term is the factor which enhances the etching rate in the lateral direction.

6.4 Stability of the nanoholes

Thermal stability of the holes was investigated by annealing the samples at 450°C and 500°C under As_4 atmosphere by systematically varying the annealing time from 0-300 second. The initial hole in this experiment is the bow-tied shaped hole obtained by 5-nm nominal etching of 10-nm GaAs cap layer. The hole depth decreases with annealing time and the hole periphery changes from the bow tied shape to an elliptical

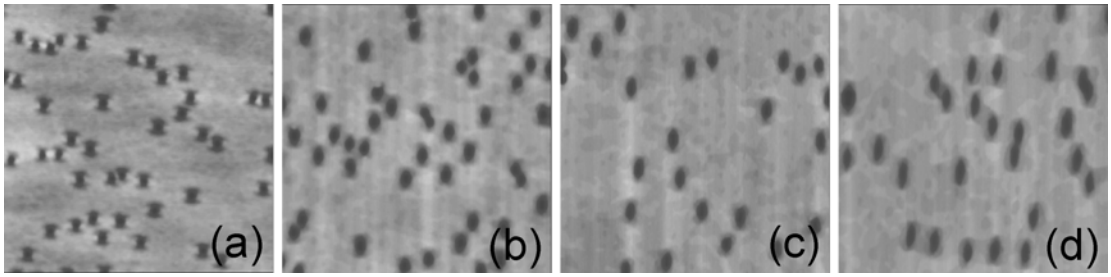

Figure 6.12 1×1 μm^2 AFM images of nanohole at different annealing time (a) 0 sec, (b) 60 sec, (c) 120 sec, (d) 300 sec

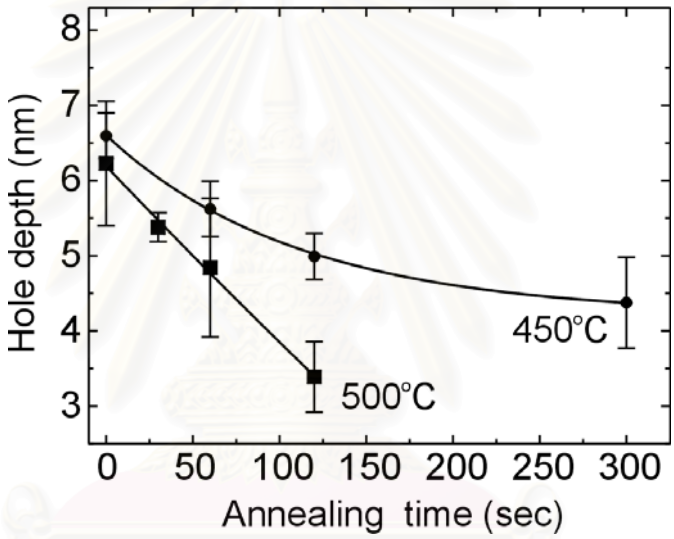

Figure 6.13 Hole depth as a function of annealing time at 450 °C and 500 °C.

structure (figure 6.12). The average hole depth as a function of annealing time at different temperatures in figure 6.13, revealing that the depth decrement rate increases with annealing temperature. The observed results can be qualitatively explained by the gradient of the chemical potential on the surface. Since the buried InAs QDs are completely removed in the nanohole used for this investigation, which is the strain contribution, is negligible in this case. The gradient of the chemical potential will follow the curvature term as depicted in figure 6.11 will drive the Ga atoms on the nanohole template to migrate down hill to the hole, causing the decrease of the hole depth during the annealing time. By increasing the annealing temperature, the hole depth decreases

more rapidly which is attributed to the higher adatom density on the surface and larger migration length of Ga adatoms at higher substrate temperature. The depth decrement of the nanohole during the annealing process is named as **self-collapsing process**.

Chapter 7

Quantum dot molecule

The self-assembled QDs caused by the strain-driven SK growth show an advantage of a possibility to obtain nanometer-sized islands without any expensive nano lithography process. However, the drawback of this growth process is that the random nature of island formation leads to the non-uniformity and unpredictable manner of spatial distribution. For optical applications, an ensemble of uniform distribution of QDs without spatial ordering might be adequate. However, for most electronics applications, accurate position control is required. Techniques which can provide lateral ordering of self-assembled QDs are still a major challenge from both physics and engineering points of view. There are several attempts to order the position of self-assembled QDs groups such as the utilization of lithographic defined patterned to control the growth kinetics and island nucleation (Karmins et al., 1997; Gin et al., 1999; Lee et al, 2000), the self patterning of strain field by the growth of stack QDs multilayer (Capellini et al., 2003), and the spontaneous forming of island group by annealing process (Zhang et al., 2001).

The aim of this chapter is to report an intriguing way of producing laterally and closely spaced self-assembled QDs, named **QD molecule,** by an *in situ* process, which is a combination of epitaxial growth and atomically precise etching. It was described in chapter 6 that the nanoholes could be created by strain modulation in GaAs cap which locally enhanced the etching rate of GaAs above the buried InAs QDs. Due to a simple and clean process and the obtained nanometer size without any prepatterning, the nanohole is therefore a promising template to laterally order self-assembled QDs.

This chapter starts with the QDs molecule realization process. Then the AFM and PL experimental results are presented. Finally, a possible model of the mechanism which is expected to occur during the deposition of InAs to the nanoholes, causing the molecule formation is proposed.

7.1 QD molecule fabrication process

In this experiment, the nanohole are used as an initial template to laterally order self-assembled QDs. The realization process of the QDs molecule fabrication process therefore consists of two main parts: the realization of nanohole template and the growth of QD molecule.

Nanohole template

The initial layer for nanohole template creation is a 1.8 ML InAs self-assembled QD layer deposited at 500°C using a very low In growth rate of 0.008- 0.01 ML/s. The substrate temperature was lowered down to 470°C and a 10-nm GaAs cap was deposited while the temperature was ramped up to 500°C. After GaAs deposition, the $AsBr_3$ etching gas was subsequently supplied at a substrate temperature of 500°C to produce the nanoholes, by using a 5 nm-nominal etching depth. The bow-tied nanoholes are used as a template for the deposition of InAs at 500°C.

QDs molecule fabrication

After a nanohole template was created, the InAs was deposited at different substrate temperatures ranging form 450°C-500°C and the amount of InAs deposition was systematically varied to understand the QD formation mechanism. The growth rate of InAs was kept at 0.008-0.01 ML/s throughout this experiment. For PL measurement, the QD molecule was embedded in a GaAs matrix and an AlGaAs confinement layer.

7.2 QD bi-molecule

Bow tied shaped hole template with a depth of around 5-6 nm shown in figure 7.1(a) is used as a new growth front for InAs deposition at 500ºC. By systematically varying the InAs thickness from 0-2.5 ML, the surface evolution during the filling process was obtained by AFM investigation. Figures 7.1 (b)-(d) illustrate that the hole depth becomes shallower and the diameter is narrower along the [1-10] direction during 0-0.6 ML InAs deposition. The morphology recovers an atomically flat surface after 0.8-

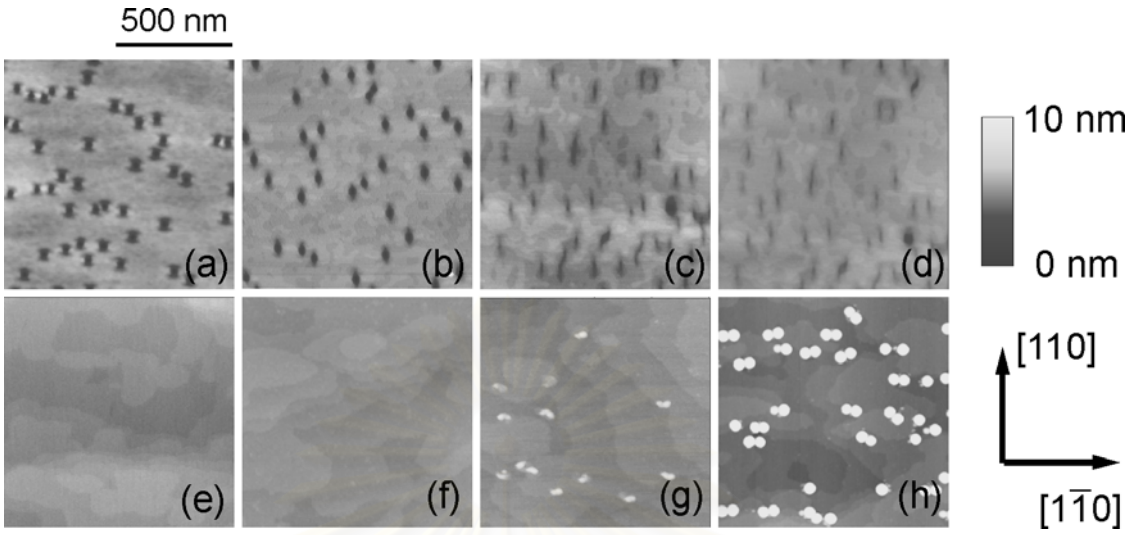

Figure 7.1 1×1 μm^2 AFM images of surface evolution during the filling hole at 500°C with InAs (a) 0 ML (b) 0.2 ML (b) 0.4 ML (d) 0.6 ML (e) 0.8 ML (f) 1.4 ML (g) 1.8 ML and (h) 2.5 ML.

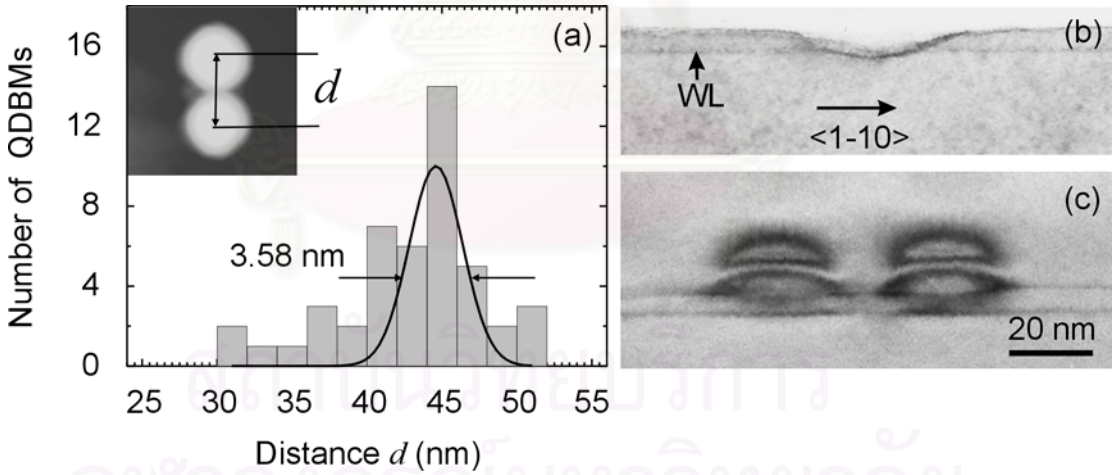

Figure 7.2 (a) The center-to-center distance between the QDs in the bi-molecule arrangement. The inset shows 125×125 nm^2 AFM image of bi-molecule structure (b) and (c) show cross-section TEM images of *in situ* etched nanohole and lateral InAs QD bi-molecule, respectively

1.4 ML InAs deposition (Figure 7.1(e)-(f)). For the 1.6 ML InAs filled holes, the initial state of the bi-molecule formation can be seen. The density of the bi molecule structure with slightly different sizes for each of the two QDs with an alignment along the [1-10] direction increased when 1.8 ML InAs was deposited as shown in figure 7.1(g). Further InAs deposition to 2.5 MLs leads to a fully-developed bi-molecule structure as shown in figure 7.1(h).

The center-to-center distance distribution of the QD bi-molecule ensemble, which is obtained from 2×2 μm^2 AFM image, is shown as a histogram in figure 7.2(a). By using a Gaussian distribution function, we obtain a mean center-to-center distance of 44.6±3.6 nm, which is similar to the distance between the QDs in the cross-sectioned TEM image (Figure 7.2(c)). From the dimension of the initial hole in figure 7.2(b), we infer that the QDs nucleate at the hole edges.

To understand the filling hole process and investigate the crystal quality of the structures, after InAs was deposited onto the nanoholes, the GaAs layer was then deposited to cover the structure for further PL measurements. The PL results at 8 K and room temperature are agree well with the AFM results. Figure 7.3(a) shows systematic PL study at 8 K of the bi-molecule formation process. For 5 nm nominal etching depth, the wetting layer (WL) signal at 1.414 eV is the dominant peak, indicating that the underlying QDs are completely removed and only the WL remains. At 0.2 ML InAs deposition, we observe another peak at 1.396 eV, which we attribute to the second InAs layer that partially filled the etched holes. For 1.6 ML InAs deposition, two peaks coexist in the spectrum, (apart from the third peak at 1.412 eV, which originates from the WL of the initial layer). The peak at 1.392 eV is appointed to some filled holes with InAs and the peak at 1.328 eV is attributed to the initial stage of the QD bi-molecule formation. This peak red-shifts to 1.046 eV with further InAs deposition and can therefore be attributed to fully developed QD bi-molecules. The linewidth of the peak is 29 meV, indicating a good size uniformity of the QD bi-molecules. Figure 7.3(b) is the summary of PL peak at room temperature as a function of InAs. The WL signal is the dominant peak until 1.6 ML InAs deposition and then the peak from the QDs in the second layer can be observed. It is noteworthy that for 2.5 ML InAs deposition, the QD bi-moelcules emit at 0.972 eV with 30 meV-linewidth and the PL intensity is comparable

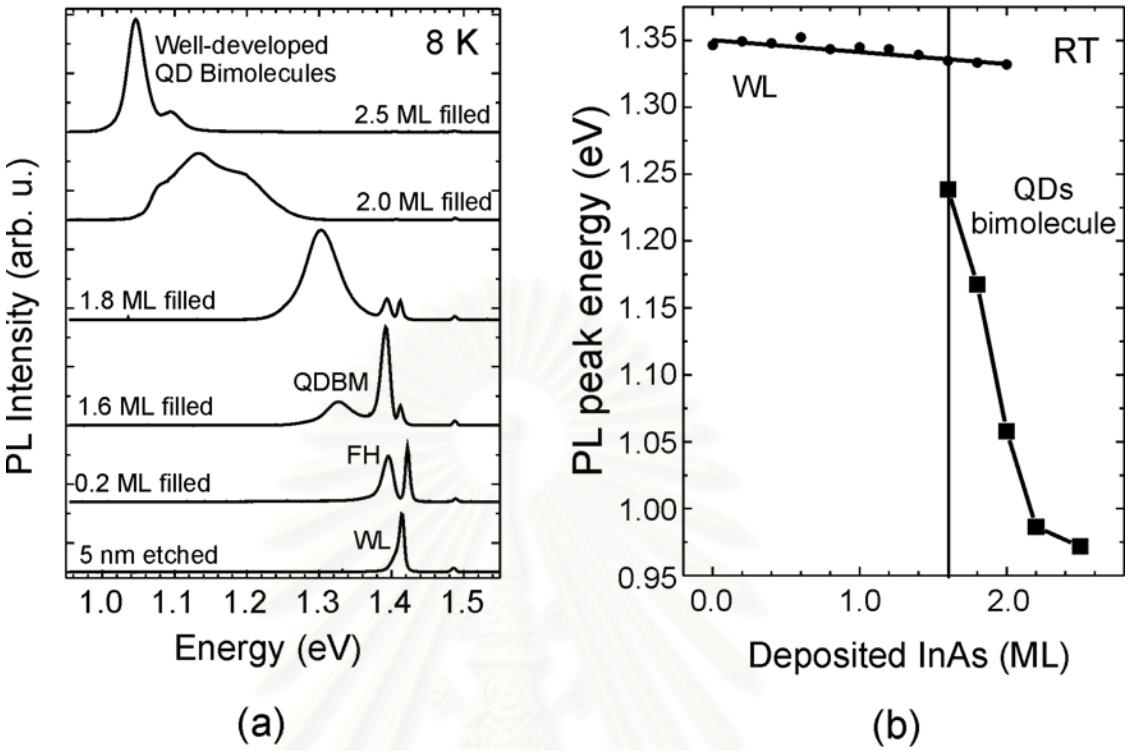

Figure 7.3. (a) PL spectra of the filled hole structure during the bi-molecule fabrication process at low temperature. (QDBM: QD bi-molecule, FH: filled hole, WL: wetting layer). (b) PL peak energy versus amount of deposited InAs at room temperature

to the original QD layer, which underlines a good size uniformity of the structure and the high crystal quality of the samples, respectively. Note that for room temperature measurements, the excitation power is 5 W for WL peak and 50 mW for QDs molecule structure.

7.3 QD Multi-molecule

From the nanohole annealing experiment, we found out that the nanohole rapidly collapse at a substrate temperature of 500°C due to the negative curvature of the nanoholes which drive Ga adatoms on surface down to the holes as described in chapter 6.

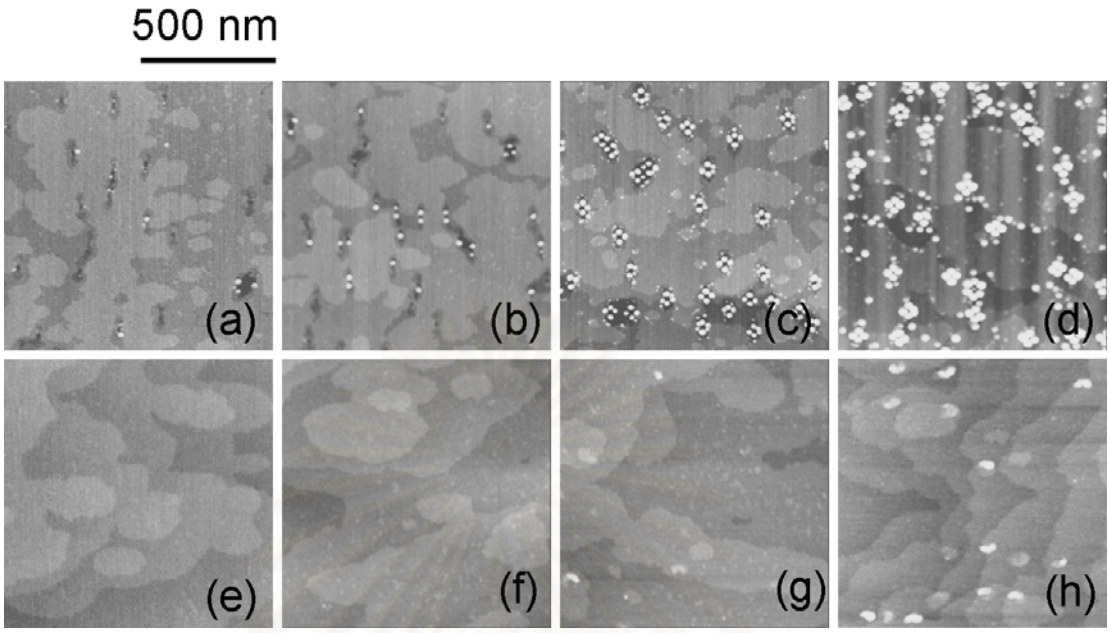

Figure 7.4 1×1 μm^2 AFM images of multi-molecule structure fabricated by deposited InAs onto nanoholes at 450°C and 500°C (a) and (d) 1.2 ML, (b) and (e) 1.4, (c) and (f) 1.6 ML, respectively. (d) 1.7 ML and (h) 1.8 ML. (The height scale is 5 nm.)

To prevent the self-collapse mechanism during the filling hole process, the substrate temperature was decreased to 450°C, where the collapse rate is low and then InAs was then deposited to fill the nanoholes. Figure 7.4 shows the comparison between the selected AFM images during the filling process at 450°C and 500°C with different amounts of InAs. At a substrate temperature of 450°C, with 1.2-ML of InAs which is far less than the critical value for InAs QDs formation, we observe the remains of the nanoholes with the InAs QD nucleation at the edge (figure 7.4(a)). Further depositing InAs to 1.4 ML, the QD nucleation density increase and preferentially occurs at the edge of the nanoholes (figure 7.4(b)). With the growth of 1.6 ML of InAs, the multi-molecule structure is obtained and the dot nucleation start forming on the flat surface between the molecule structure as shown in figure 7.4(c). Moreover, we can identify a small depression in the inner part of the molecule structure. Further depositing InAs to 1.7 ML, leads the growth of island which stay on the flat surface in between QD molecule (figure

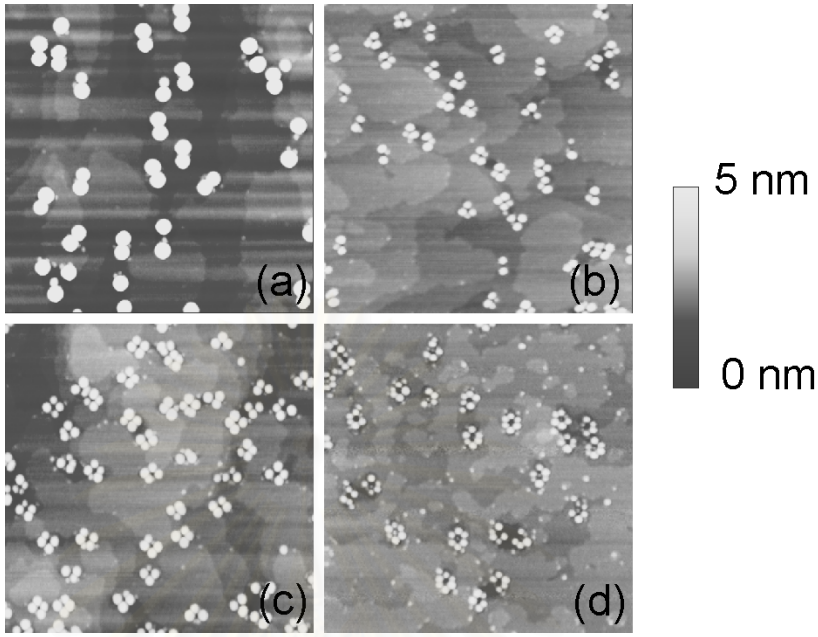

Figure 7.5 1×1 μm^2 AFM images of multi-molecule structure fabricated by deposited InAs onto nanoholes (a) 2.5 ML at 500°C (b)1.8 ML InAs at 470°C (c) 2.0 ML InAs at 470°C, and (d) 1.8 ML InAs at 450°C

7.4(d)). In this case we can clearly see that the QD preferentially grow at kinks or the atomic steps. The small depression inside the molecule structure is hardly observed due to the larger QD size in molecule structure.

Figures 7.4 (e)-(f) are the surface evolution during the filling hole with InAs at 500°C. The surface morphology developed in a completely different way compared with those at 450°C, mainly due to the larger collapse rate at this temperature. With 1.2 ML of InAs, the surface becomes atomically flat. There is no evident of the remaining of the nanoholes on the surface. With 1.4 ML of InAs, the 2D islands which is the initial state of QDs are observed on the surface. The nucleation of the QDs can be seen on the surface at 1.6 ML of InAs deposition. This deposited amount is comparable to the critical value for InAs QDs formation on the flat surface. Most of the QDs nucleation form in pairs with each having different size and align along [-110] direction. The density of the initial bi-molecule structure increases when 1.8 ML of InAs was deposited.

By changing the substrate temperature for InAs deposition from 450 to 500°C and the amount of InAs from 1.8 to 2.5 ML, the dominant number of QDs per molecules (*n*) can increase to 6 as shown in figure 7.5. Figures 7.6(a), (b), (c) and (d) are bi molecule (2 dots per molecule), tri-molecule (3 dots per molecule), quad-molecule (4 dots per molecule), and hexa-molecule (6 dots per molecule) which are obtained by the deposition of 2.5 ML InAs at 500°C, 1.8 ML InAs at 470°C, 2.0 ML InAs at 470°C, and 1.8 ML at 450°C, respectively. We found out that the numbers of QDs per molecule are sensitive to the growth conditions. If we compare the results from figure 7.4(d) to figure 7.5(d), by using the same growth condition, the structures obtained are different. Even though the growth rate and substrate temperature is controlled, the fluctuation of the substrate temperature during growth causes the numbers of QDs to be difficult to tune.

For statistical analysis we selected several different samples grown under growth conditions where the percentage of certain *n*-fold QD molecules was particularly high and the results are summarized as a histogram plotted shown in figure 7.6. For 2.5 ML InAs deposition at 500°C, we obtain 59% bi-molecules and 40% isolated dots, while for 2 ML InAs deposition at 470°C, we obtain 52% quad-molecules, 28% tri-molecules, 4% bi-molecules, and 16% others. In the case of 1.8-ML InAs deposition at 450°C, we obtained 32% hexa-molecules, 22% penta-molecules, 8% hepta-molecules and 38% others. We observe that the maximum percentage of *n*-fold QD molecules decreases with *n* due to a wider *n* distribution. The wider distribution of *n*-fold QD molecules with large *n* is caused by smaller atom migration lengths at lower temperatures

Figure 7.7 provides information about the maximum percentage on a sample surface as a function of *n*. *N*-fold QD molecules with large *n* tend to form when the hole-filling process was performed at lower substrate temperature, because In atoms have a higher possibility to nucleate before incorporation into the molecule. We note that the formation of even numbered QD molecules tends to have a higher probability than that of odd numbered QD molecules. We attribute this effect to the two-fold symmetry of the hole structure.

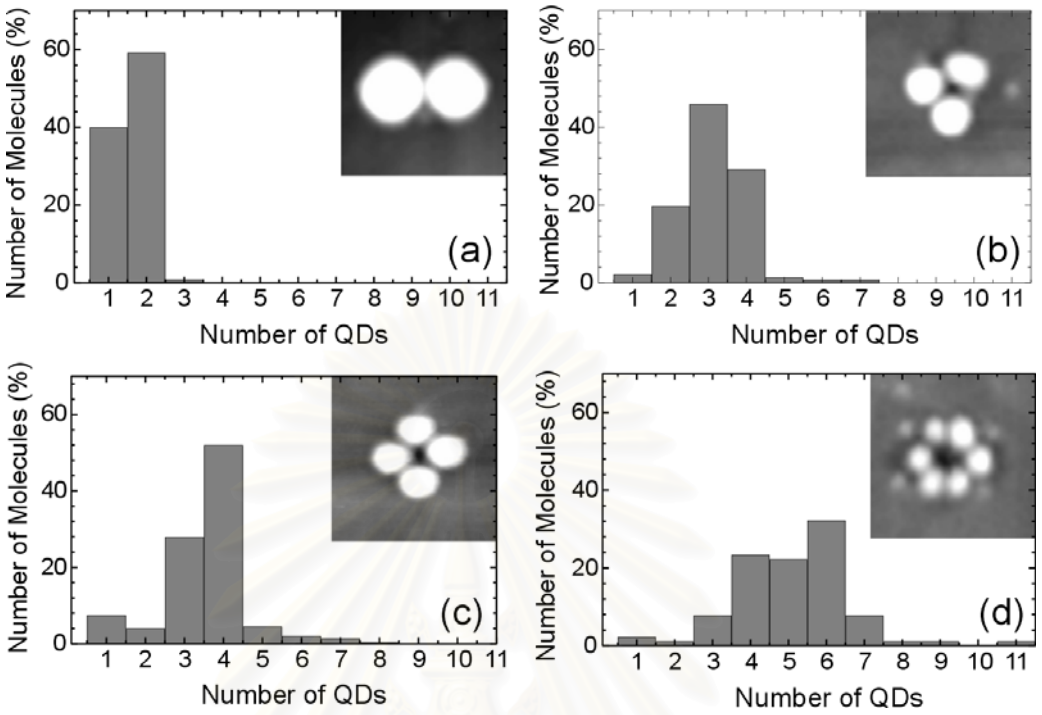

Figure 7.6 The histogram of the number of QD per molecules in the growth condition which provides the dominant number of QD equal to (a) two, (b) three, (c) four, and (d) six per molecule. The insets show 125×125 nm^2 AFM images of dominant multi-molecules.

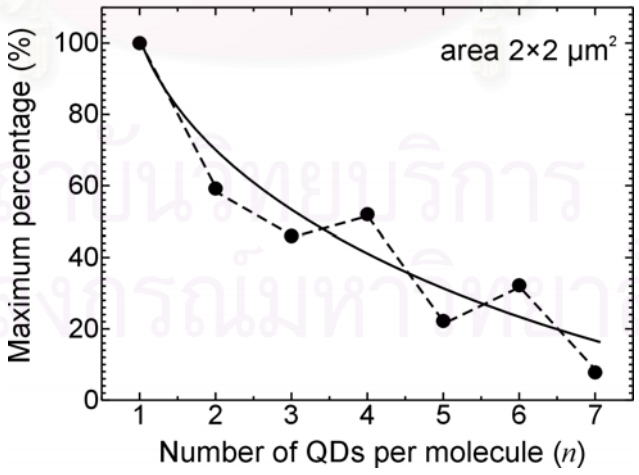

Figure 7.7 Maximum percentage of dominant molecules on the sample surface as a function of the dominant number of QDs per molecule (n)

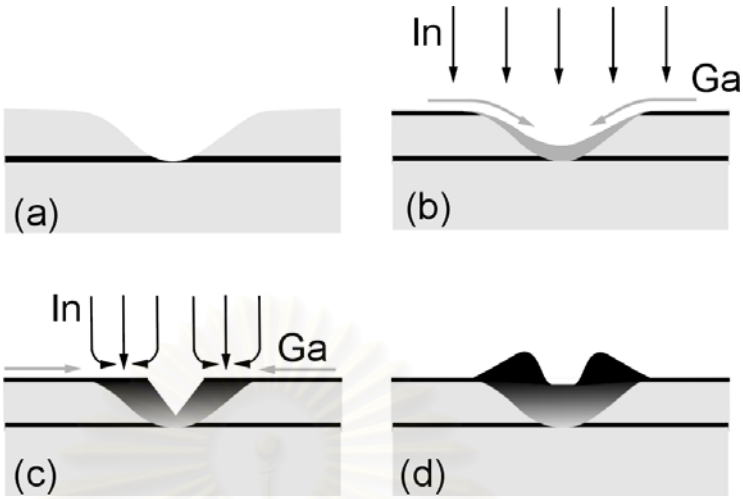

Figure 7.8 Schematic illustration of the molecule formation (a) initial nanohole (b) early stage of filling process, (c) preferential InAs growth at the hole edge, and (d) QDs- molecule formation

7.4 Possible mechanism of QD molecule formation

The surface morphology after the InAs filling hole at 450°C shows that the edge of the nanoholes is the dominant factor, which leads the formation of the molecule structure. The QD nucleation can be observed before the InAs thickness reaches the critical value for the dot formation and we clearly see the remain of the nanohole. The simple mechanism, which might explain the formation of the molecule structure, is schematically depicted in figure 7.8. The negative curvature of the initial nanohole in figure 7.8(a) could be the driving force for adatoms to migrate down to the hole both Ga adatoms (from self-collapse mechanism) and In atoms (from deposition). At high substrate temperatures, larger amount of Ga adatoms and larger migration length of Ga atoms cause the higher collapse rate during the filling hole process, therefore, the holes are expected to be filled with more Ga atoms at higher substrate temperatures. This is the reason why we can not observe the remaining of the holes before the QDs nucleation start at 500°C. At the initial stage of the deposition both In and Ga adatoms are supposed to grow at the bottom of the hole. The topmost layer is expected to be InAs due to the segregation of InAs (Gerard and Marzin, 1992). Since the InAs layer is strongly

compressed at the bottom of the hole, the In atoms preferentially attach at the hole edge where the InAs layer can relax more easily. This growth model is supported by the AFM images in figures 7.4(c)-(d) and figures 7.5(a)-(b) that the hole diameter drastically narrow with increasing the In deposition while the annealing process shows less effects to the hole diameter. Finally, the hole edge with the partially relaxed InAs induces a current of In atoms towards the edge leading to the QD molecule nucleation around the hole (figure 7.8(c) and 7.8(d)).

CHAPTER 8

Conclusions

This work presents a fundamental study of self-assembled InAs/GaAs quantum dots (QDs) and a fabrication process to realize the new nanostructures such as the nanohole and QD molecules by utilizing the InAs QDs as an initial template.

We first start the experiment with the investigation of the growth parameters to the structural and optical properties of InAs QDs grown Stranski Kranstanow (SK) growth mode. The amount of InAs deposition, the growth rate and substrate temperature are systematically varied to provide and understanding of the QD formation mechanism and a way to tune the QDs properties by changing the growth parameters. The comparative study of photoluminescence from different type of QDs gives the basic idea of the optical properties of SK QDs.

The large and low density QD grown by using very low InAs growth rate were selected to further the investigation of the overgrowth process. The structural and optical properties of the QDs covered with various types of the cap layer reveal the crucial effects of the overgrowth layers. The surface morphology evolution of large InAs QDs during GaAs and $In_xGa_{1-x}As$ overgrowth at low temperature were investigated by systematically varying the thickness and the strain (In composition) of the cap layer. For GaAs overgrowth, the InAs QDs transform into an elongated ridge-valley structure, whereas the InAs QDs tend to preserve their shape during the capping with InGaAs. The shape evolution during the capping process can be explained by the effect of elastic energy and surface energy on the chemical potential. Since the InGaAs cap layer not only preserves QDs shape but also decreases the strain between the QD and the matrix and reduces the energy barrier, the PL peak emitted from the QDs covered with InGaAs therefore extend to the longer wavelength. However, with In content larger than 20%, the highly strain in the experimented structure induces the dislocation formation and deteriorate the PL intensity.

The strain modulation on the GaAs cap layer introduced by the buried large InAs QDs was combined with $AsBr_3$ *in situ* etching process to create the new structures i.e. nanoholes and QD molecule. We presented a systematic investigation of self-assembled nanoholes formation on top of capped QDs by using $AsBr_3$ *in situ*

etching. We observed two etching regimes for the nanoholes formation. The evolution of the two regimes depends on the nominal etching depth and the thickness of the GaAs capping layer. We appoint the nanohole formation to a strain enhanced etching rate on top of the buried QDs.

The homogenous nanohole which created by supplying 5 nm-nominal etching gas on to 10-nm GaAs cap thickness was used as a new growth front for InAs deposition, leading the lateral QD molecule formation. These QD molecules naturally form around self-assembled nanoholes where InAs can be more relax. The number of QDs involved in the molecules can be tuned from 2 to 6 by simply changing the InAs growth conditions such as the amount of InAs deposition and the substrate temperature. We found that even-numbered QD molecules are more likely to form than odd-numbered molecules, attributing to the two fold symmetric of the initial nanoholes. A systematic study of the hole filling as well as hole collapsing process allows us to develop a qualitative growth model for the QD molecule formation.

References

Alferov, Z. I. 2001. Nobel Lecture: the double heterostructure concept and its applications. Reviews of Modern Physics 73: 767-782.

Arakawa, Y., and Sakaki, H. 1982. Multidimensional quantum well laser and temperature dependence of its threshold current. Applied Physics Letters 40: 939-941.

Asada, M.; Miyamoto, Y.; and Suematsu, Y. 1986 Gain and the threshold of three-dimensional quantum-box lasers. IEEE Journal of Quantum Electronics QE-22: 1915-1921.

Austing, D. G., et al. 1998. Quantum dot molecules. , Physica B 249-251: 206.

Barabási, A.-L. 1997. Self-assembled island formation in heteroepitaxial growth. Applied Physics Letters 70: 2565-2567.

Barabási, A.-L. 1999. Thermodynamic and kinetic mechanisms in self-assembled quantum dot formation. Material Science and Engineering B 67: 23-30.

Barabási, A.-L., and Stanley H. E. 1995. Fractal concepts in surface growth Cambridge: Cambridge University Press.

Bastard, G., and Brum, J. A. 1986. Electronic states in semiconductor heterostructures. IEEE Journal of Quantum Electronics QE-22: 1625-1644.

Bhattacharya, P., 1993 Eds, Properties of Lattice-Matched and Strained Indium Gallium Arsenide, IEE, INSPEC.

Bimberg, D.; Grundmann, M.; and Ledentsov, N. N. 1999. Quantum dot heterostructures. Chichester: Wiley.

Blosssey, R. and Lorke, A. 2002. Wetting droplet instability and quantum ring formation. Physical Review E 65: 021603-1-3.

Burkard, G., Loss D, and DiVincenzo, D.,P, (1999) Coupled quantum dots as quantum gates Physical Review B 59: 2070-2078.

Capellini, G., et al. 2003. Ordering self-assembled islands without substrate patterning. Applied Physics Letters 82:1-3

Chen, Y., and Washburn, J. 1996. Structural transition in large-lattice-mismatch heteroepitaxy. Physical Review Letters 77: 4046-4049.

Costantini G., et al. 2003. InAs/GaAs(001) quantum dots close to thermodynamic equilibrium. Applied Physics Letters 82:3194 -3196.

Dahaese, O.,Wallart, X., and Mollot, F. 1995, Kinetic model of element III segregation during molecular beam epitaxy of III-III'-V semiconductor compounds Applied Physics Letters 66:52 -54.

Daruka, I., and Barabási, A. L. 1997. Dislocation-free island formation in heteroexpitaxial growth: a study at equilibrium. Physical Review Letters 79: 3708-3711.

Daruka, I., and Barabási, A.-L. 1998. Equilibrium phase diagrams for dislocation free self –assembled quantum dots. Applied Physics Letters 72: 2102-2104.

Daruka, I., et al. 1999. Molecular dynamics investigation of the surface stress distribution in a Ge/Si quantum dots superlattice. Physical Review B 60: R2150-R2153.

Dobbs, H. T., et al. 1997. Mean-field theory of quantum dot formation. Physical Review Letters 79: 897-900.

Eberl, K., et al. 2001. Self-assembling quantum dots for optoelectronic devices on Si and GaAs. Physica E 9: 164-174.

Eliseev, P. G. et al. 2001. Ground-state emission and gain in ultralow-threshold InAs-InGaAs quantum-dot lasers. IEEE Journal on Selected Topics in Quantum Electronics 7: 135-142.

Farrel, H. H., and PalmstrØm, C. J. 1990. Reflection high energy electron diffraction characteristic absences in GaAs(100)(2×4)-As: A tool for determining the surface stoichiometry. Journal of Vacuum Science and Technology B 8:903-907.

Garcia, J. M., et al. 1997. Intermixing and shape changes during the formation of InAs self-assembled quantum dots. Applied Physics Letters 71:2014-2016.

Gerard, J. M., and Marzin, J. Y. 1992. Monolayer-scale optical investigation of segregation effects in semiconductor heterostructures Physical Review B 45:6313-6316.

Grandjean, N., Massies, J., and Leroux, M. 1996. Monte Carlo simulation of In surface segregation during the growth of $In_xGa_{1-x}As$ on GaAs (001) Physical Review B 53:998-1001.

Grundmann M. et al. 1996. Excited states in self-organized InAs/GaAs quantum dots: Theory and experiment Applied Physics Letters 68:978-981.

Grundmann, M. 2000. The present status of quantum dot laser. Physica E: 5 167-184.

Heidemeyer, H., et al. 2002. Closely stacked InAs/GaAs quantum dots grown at low growth rate. Applied Physics Letters 80:1544-1546.

Herman, M. A., and Sitter, H. 1989. Molecular beam epitaxy fundamentals and current status Berlin: Spinger-Verlag.

Holý, V., et al.1999. Strain induced vertical and lateral correlations in quantum dot superlattices Physical Review Letters 83:356-359.

Hu, S.M. 1989 Stress from a parallelepipeic thermal inclusion in a semispace. Applied Physics Letters 66: 2741-2743

Jesson, D. E., et al. 1993. Direct Imaging of surface cusp evolution during strained-layer epitaxy and implications for strain relaxation. Physical Review Letters 71: 1744-1747.

Jin, G. et al. 1997 Controlled arrangement of self-organized Ge islands on patterned Si (001) substrates Applied Physics Letters 75: 2752-2754.

Joyce, P. B., et al. 2000. Effect of growth rate on size, composition, and optical properties of InAs/GaAs quantum dots grown by molecular-beam epitaxy. Physical Review B 62: 10891-10895.

Joyce, P. B., et al. 2001. Shape and surface morphology changes during the initial stages of encapsulation of InAs/GaAs quantum dots. Surface Science 492: 345-353.

Joyce, P. B., et al. 2001. Shape and surface morphology changes during the initial stages of encapsulation of InAs/GaAs quantum dots. Surface Science 492: 345-353.

Kamins, T. I, and Stanley Williams, R. 1997. Lithographic positioning of self-assembled Ge islands on Si(001). Applied Physics Letters 71: 1201-1203.

Kamiya, I.; Tanaka, I.; and Sakaki, H. 1998. Optical properties of near surface InAs quantum dots and their formation processes. Physica E 2: 637-642.

Kaneko, T., et al. 1995. Reentrant layer-by-layer etching of GaAs(001). Physical Review Letters 74: 3289-3292.

Kim, S. M; Hurtado, J. A.; and Tan. H. 1999. Evolution of a Surface-roughness caused by stress in nanometer-scale chemical etching. Physical Review Letters 19: 3872-3875

Kiravittaya, S.; Nakamura, Y.; and Schmidt, O. G. 2002. Photoluminescence linewidth narrowing of InAs/GaAs self-assembled quantum dots. Physica E 13: 224-228

Kiravittaya, S.; Songmuang, R.; and Schmidt, O. G. 2002. Self-assembled quantum dots and nanoholes by molecular beam epitaxial growth and atomically precise *in situ* etching. Proceedings of the Material Research Society Symposium 722: K10.11.1-6.

Kiravittaya, S.; Songmuang, R.; and Schmidt, O. G. 2003. Self-assembled nanoholes and lateral QD bi-molecules by molecular beam epitaxy and atomically precise *in situ* etching. 2003 Journal of Crystal Growth 251: 258

Kohmoto, S., et al. 1999. Site-controlled self-organization of individual InAs quantum dots by scanning tunneling probe-assisted nanolithography. Applied Physics Letters 74: 3488-3490.

Ledentsov, N. N., et al. 1996. Direct formation of vertically coupled quantum dots in Stranski-Krastanow growth. Physical Review B 54: 8743-8750.

Lee, H., et al. 2000. Controlled ordering and positioning of InAs self-assembled quantum dots. Journal of Vacuum Science and Technology B 18: 2193-2196.

Leonard D., et al. 1993 Direct formation of quantum-sized dots from uniform coherent islands of InGaAs on GaAs surfaces. Applied Physics Letters 63: 3203-3205.

Lorke, A. et al. 2000. Spectroscopy of nanoscopic semiconductor rings. Physical Review Letters 84: 2223-2226.

Lorke, A. et al. 2001. Growth and electronic properties of self-organized quantum ring. Japanese Journal of Applied Physics 40: 1857-1859.

Marzin, J. Y., et al. 1994. Photoluminescence of single InAs quantum dots obtained by self-organized growth on GaAs**.** Physical Review Letters 73: 716-719

Mo, Y. M., et al. 1990 Kinetic pathway in Stranski-Krastanov growth of Ge on Si(001) Physical Review Letters 65: 1020–1023

Moison, J. M., et al. 1994 Self-organized growth of regular nanometer-scale IhAs dots on GaAs Applied Physics Letters 64:196-198. 64: 196-198.

Nishi, K., et al. 1999. A narrow photoluminescence linewidth of 21 meV at 1.35 μm from strain-reduced InAs quantum dots covered by $In_{0.2}Ga_{0.8}As$ grown on GaAs substrates. Applied Physics Letters 74: 1111-1113.

Oshinowo J., et al. 1994. Highly uniform InGaAs/GaAs quantum dots (~15 nm) by metalorganic chemical vapor deposition. Applied Physics Letters 65: 1421-1423

Pimpinelli, A., and Villain, J. 1998. Physics of crystal growth Cambridge: Cambridge University Press.

Priester, C., and Lannoo, M. 1995 Origin of self-assembled quantum dots in highly mismatched heteroepitaxy. Physical Review Letters 75: 93-98.

Ritz, M.; Kaneko, T.; and Eberl, K. 1997. The effect of surface reconstructions on the surface morphology during *in situ* etching of GaAs. Applied Physics Letters 71: 695-697.

Saito, H.; Nishi, K.; and Sugou, S. 1998. Influence of GaAs capping on the optical properties of InGaAs/GaAs surface quantum dots with 1.5 μm emission. Applied Physics Letters 73: 2742-2744.

Schuler, H., et al. 1998. Size modification of self-assembled InAs quantum dots by in situ etching. Semiconductor Science and Technology 13: 1341-1345.

Schuler, H., et al. 2000. *In situ* etching with $AsBr_3$ and regrowth in molecular beam epitaxy. Semiconductor Science and Technology 15: 169-177.

Schmidt, O. G., et al. 2002. Self-assembled semiconductor nanostructures: climbing up the ladder of order. Surface Science 514: 10-18.

Seifert, W. et al. 1996. In-situ growth of quantum dot structures by the Stranski-Krastanow growth mode. Progress in Crystal Growth and Characterization 33: 423-471.

Seifert, W. et al. 1999. Continuous and discontinuous metal-organic vapor phase epitaxy of coherent self-assembled islands effects on size homogeneity. Journal of Crystal Growth 197: 19-24.

Shiraishi K. 1992, Applied Physics Letters 60:1363.

Shchukin, V. A. et al. 1995. Spontaneous ordering of arrays of coherent strained islands. Physical Review Letters 75: 2968-2971.

Shchukin, V. A., and Bimberg, D. 1999. Spontaneous ordering of nanostructures on crystal surfaces. Reviews of Modern Physics 71: 1125-1171.

Shchukin, V. A., et al. 2001. Spontaneous formation of nanostructures on crystal surfaces. Physica E 9: 140-148.

Springholz et al. 1998. Self-organized growth of three-dimensional quantum-dot crystals with fcc-like stacking and a tunable lattice constant. Science 282: 734-738

Spencer, B. J., and Tersoff, J. 2001. Stresses and first-order dislocation energetics in equilibrium Stranski-Krastanow islands. Physical Review B 63: 205424-1-9

Srolovitz, D. J. 1989. On the stability of surfaces of stressed solids. Acta Metallurgica 37: 621-625.

Sugawara, M. 1999. Theoretical based of the optical properties of semiconductor quantum nano-structures. In M. Sugawara (ed.), Semiconductors and Semimentals vol. 60: Self-assembled InGaAs/GaAs quantum dots, pp. 1-116, San Diego: Academic Press.

Sutter, P. and Lagally, M. G. 1998. Embedding of Nanoscale 3D SiGe islands in a Si Matrix. Physical Review Letters 81: 3471-3474.

Tatebayashi, J., et al. 2001. Over 1.5 μm light emission from InAs quantum dots embedded in InGaAs strain reducing layer grown by metalorganic chemical vapor deposition. Applied Physics Letters 78: 3469-3471.

Tersoff, J., Teichert, C. and Lagally, M. G. 1996. Self-organization of growth of quantum dot superlattice. Physical Review Letters 76:1675-1678.

Tsang, W.T, Chiu, T.H., and Kapre R. M. 1993. Monolayer chemical beam etching: Reverse molecular beam epitaxy Applied Physics Letters 63: 2500-2502.

Wang, L. G. et al. 2000. Size, shape, and stability of InAs quantum dots on the GaAs(001) substrate. Physical Review B 62: 1897-1904.

Wang L.G., Kratzer, P., and M. Scheffler 2000 Japanese Journal of Applied Physics 39: 429-431.

Wang, L. G. et al. 2000. Size, shape, and stability of InAs quantum dots on the GaAs(001) substrate. Physical Review B 62: 1897-1904.

Wang, L.G., et al. 2001. Island dissolution during capping layer growth interruption Applied Physics A 73: 161-165.

Wang, X. D., Niu, Z., and Feng, S. 2000. Influence of $In_xGa_{1-x}As$ ($0 \leq 0 \leq 0.3$) cap layer on structural and optical properties of self-assembled InAs/GaAs quantum dots. Japanese Journal of Applied Physics 39: 5076-5079.

Wang, X. D.,et al. 2001. Effect of $In_xGa_{1-x}As$ ($0 \leq x \leq 0.4$) capping layer on self-assembled 1.3 μm wavelength InAs/GaAs quantum islandsJournal of Crystal growth 223: 363-368.

Xie, Q., Chen, P., and Madhukar, A. 1994. InAs island-induced-strain driven adatom migration during GaAs overlayer growth. Applied Physic Letters 65: 2051-2053 .

Xie, Q., et al. 1995. Vertically self-organized InAs quantum box islands on GaAs(100). Physical Review Letters 75: 2542-2545

Yu, W. and Madhukar, A., 1997. Molecular dynamics study of coherent island energetics, stresses, and strains in highly strained epitaxy. Physical Review Letters 79, 905-908.

Zhang J., et al. 1997. Modulated beam studies of the layer by layer etching of GaAs (001) using $AsBr_3$ identification of the reaction mechanism. Journal of Crystal Growth 175/176: 1284-1288.

List of Publications

1. International Journals and International Conferences

1. Suwit Kiravittaya; **Rudeesun Songmuang;** Supachok Thainoi; Suwat Sopitpan; Songphol Kanjanachuchai; Somchai Ratanathammaphan; Montri Sawadsaringkarn; and Somsak Panyakeow. 2000. Self-assembled composite quantum dots for photovoltaic applications. Proceedings of the 28th IEEE Photovoltaic Specialists Conference 818-821.

2. **Rudeesun Songmuang**; Suwit Kiravittaya; Supachok Thainoi; Pornchai Changmuang; Suwat Sopitpan; Somchai Ratanathammaphan; Montri Sawadsaringkarn; and Somsak Panyakeow. 2001. Selective growth of InAs/GaAs self-organized quantum dots by shadow mask technique. Journal of Crystal Growth 227-228: 1053-1056.

3. Suwit Kiravittaya; **Rudeesun Songmuang**; Pornchai Changmuang; Suwat Sopitpan; Somchai Ratanathammaphan; Montri Sawadsaringkarn; and Somsak Panyakeow. 2001. InAs/GaAs self-organized quantum dots on (411)A GaAs by molecular beam epitaxy. Journal of Crystal Growth 227-228: 1010-1015.

4. Schmidt, O. G.; Suwit Kiravittaya; Nakamura, Y.; Heidemeyer, H.; **Rudeesun Songmuang**; Müller, C.; Jin-Phillip, N. Y.; Eberl, K.; Wawra, H.; Christiansen, S.; Gräbeldinger, H.; and Schweizer, H. 2002 Self-assembled semiconductor nanostructures: climbing up the ladder of order. Surface Science 514: 10-18.

5. Suraphol Kamprachum; Suwit Kiravittaya; **Rudeesun Songmuang**; Supachok Thainoi; Songphol Kanjanachuchai; Montri Sawadsaringkarn; and Somsak Panyakeow. Multi-stacked quantum dots with graded dot sizes for photovoltaic applications. Proceedings of the 29th IEEE Photovoltaic Specialists Conference (in press).

6. Schmidt, O. G.; Deneke, C.; Suwit Kiravittaya; **Rudeesun Songmuang**; Nakamura, Y.; Zapf-Gottwick, Y.; Müller, C.; and Jin-Phillip, N. Y. Self-assembled nanoholes, lateral quantum dot molecules, and semiconductor nanotubes. 2002 IEEE Journal of Selected Topics in Quantum Electronics 8: 1025-1034.

7. **Rudeesun Songmuang**; Suwit Kiravittaya; and Schmidt, O. G. Shape evolution of InAs quantum dots during overgrowth. 2003 Journal of Crystal Growth 249: 416-421.

8. Suwit Kiravittaya; **Rudeesun Songmuang**; Jin-Phillip, N. Y.; Panyakeow, S.; and Schmidt, O. G. Self-assembled nanoholes and lateral QD bi-molecules by molecular beam epitaxy and atomically precise *in situ* etching. 2003 Journal of Crystal Growth 251: 258-263.

9. **Rudeesun Songmuang**; Suwit Kiravittaya; Montri Sawadsaringkarn; Somsak Panyakeow; and Schmidt, O. G. Photoluminescence investigation of low temperature capped self-assembled InAs/GaAs quantum dots. 2003 Journal of Crystal Growth 251: 166-171.

10 **Rudeesun Songmuang;** Suwit Kiravittaya; and Schmidt, O. G. Formation of lateral quantum dot molecules around self-assembled nanoholes. 2003 Applied Physics Letter 82: 2892-2894.

11. Costantini, G.; Manzano, C.; **Rudeesun Songmuang**; Schmidt, O.G.; and Kern, K. InAs/GaAs(001) quantum dots close to thermodynamic equilibrium. 2003 Applied Physics Letter 82: 3194-3196.

2. Domestic Journals and Domestic Conferences

1. ***Rudeesun Songmuang;*** *Suwat Sopitpan; and Somsak Panyakeow, "Study on Optically Pumped Edge Emission of $Al_{0.2}Ga_{0.8}As/GaAs$ 10 Multiple Quantum Well and $GaAs/In_{0.2}Ga_{0.8}As$ Single Quantum Well,"* Proceeding of the 21st conference on electrical engineering, Kasetsart University *(8-9 December 1998)*

2. Suwit Kiravittaya; **Rudeesun Songmuang**; Montri Sawadsaringkarn; and Somsak Panyakeow. 2000. *In-situ* RHEED investigation of MBE-grown InAs QDs on (0 0 1) GaAs epilayer. Proceedings of the 23rd Electrical Engineering Conference 689-692.

3. **Rudeesun Songmuang**; Suwit Kiravittaya; Montri Sawadsaringkarn; and Somsak Panyakeow. 2000. InAs/GaAs, InGaAs/GaAs, and InAs/InGaAs/GaAs composite quantum dots. Proceedings of the 23rd Electrical Engineering Conference 685-688.

4. **Rudeesun Songmuang**; Suwit Kiravittaya; Montri Sawadsaringkarn; and Somsak Panyakeow. 2002. The growth of InAs self-organized quantum dots by molecular beam epitaxy. Research and Development Journal, The Engineering Institute of Thailand 13: 34-41.

5. Suwit Kiravittaya; **Rudeesun Songmuang**; Montri Sawadsaringkarn; and Somsak Panyakeow. 2002. Kinetic Monte-Carlo simulation of molecular beam epitaxial growth. Proceedings of the 25th Electrical Engineering Conference EL134-EL138.

List of Presentations

1. International presentations

Oral presentation

Rudeesun Songmuang; Suwit Kiravittaya; and Schmidt, O.G. Molecular beam epitaxy and *in situ* etching for nanohole and lateral quantum dot multi-molecule fabrication. The 4th International conference on low dimensional structures and devices, Fortaleza, Ceará, Brazil, December 8-13 (2002).

Oral presentation

Rudeesun Songmuang; Suwit Kiravittaya; and Schmidt, O.G. Nanoholes and lateral quantum-dot molecules by molecular beam epitaxy and *in situ* etching. 12th Euro-MBE workshop Congress Center Bad Hofgastein, Austria, Febuary 16 – 19 (2003).

Poster presentation

Rudeesun Songmuang; Suwit Kiravittaya; Pornchai Changmuang; Suwat Sopitpan; Somchai Ratanathammaphan; Montri Sawadsaringkarn; and Somsak Panyakeow. Selective growth of InAs/GaAs self-organized quantum dots by shadow mask technique. The 11th International Conference on Molecular Beam Epitaxy, Beijing, China, September 10-15 (2001).

Poster presentation

Rudeesun songmuang; Supachok Thainoi; Songphol Kanjanachuchai; Montri Sawadsaringkarn; and Somsak Panyakeow. Photovoltaic solar energy conference and exhibition photovoltaic effects in composite quantum dot structures 2001 international congress center, Munich, Germany 22-26 October (2002)

2. Domestic presentations

Oral presentation

Suwit Kiravittaya; Rudeesun Songmuang; Montri Sawadsaringkarn; and Somsak Panyakeow. *In-situ* RHEED investigation of MBE-grown InAs QDs on (0 0 1) GaAs epilayer. The 23rd Electrical Engineering Conference, Empress hotel, Chiang-Mai, November 23-24 (2000).

Oral presentation

Rudeesun Songmuang; Suwat Sopitpan; and Somsak Panyakeow, Study on Optically Pumped Edge Emission of $Al_{0.2}Ga_{0.8}As$/GaAs 10 Multiple Quantum Well and GaAs/$In_{0.2}Ga_{0.8}As$ Single Quantum Well The 21st conference on electrical engineering, Kasetsart University, December 8-9 (1998)

Miscellaneous

Oral presentation

Suwit Kiravittaya; **Rudeesun Songmuang**; Jin-Phillip, N. Y.; Somsak Panyakeow; and Schmidt, O. G. Self-assembled nanoholes and lateral QD bi-molecules by molecular beam epitaxy and atomically precise *in situ* etching. The 12th International Conference on Molecular Beam Epitaxy, San Francisco, U.S.A., September 16-20 (2002).

Oral presentation

Costantini, G.; Manzano, C.; **Rudeesun Songmuang**; Schmidt, O.G.; and Kern, K. STM analysis of the growth and overgrowth of "large" InAs/GaAs(001) quantum dots Deutsche Physikalische Gesellschaft (DPG), Dresden, Germany, March 24-28 (2003).

Poster presentation

Rudeesun Songmuang; Suwit Kiravittaya; Montri Sawadsaringkarn; Somsak Panyakeow; and Schmidt, O. G. Photoluminescence investigation of low temperature capped self-assembled InAs/GaAs quantum dots. The 12th International Conference on Molecular Beam Epitaxy, San Francisco, U.S.A., September 16-20 (2002).

Poster presentation

Costantini, G.; Manzano, C.; **Rudeesun Songmuang**; Schmidt, O.G.; and Kern, K. Importance of kinetic effects during the overgrowth of large InAs quantum dots 12th Euro-MBE workshop Congress Center Bad Hofgastein, Austria, Febuary 16 – 19 (2003).

Miscellaneous

2. Domestic Presentations

- *Oral presentation*

  Suwit Kiravittaya; **Rudeesun Songmuang**; Montri Sawadsaringkarn; and Somsak Panyakeow. *In-situ* RHEED investigation of MBE-grown InAs QDs on (0 0 1) GaAs epilayer. The 23rd Electrical Engineering Conference, Empress hotel, Chiang-Mai, November 23-24 (2000).

- *Oral presentation*

  Suwit Kiravittaya; **Rudeesun Songmuang**; Montri Sawadsaringkarn; and Somsak Panyakeow. Kinetic Monte Carlo simulation of molecular beam epitaxial growth. The 25th Electrical Engineering Conference, Prince of Songkla University, Songkla, November 21-22 (2002).

VITAE

Rudeesun Songmuang was born in Bangkok, Thailand on March 17, 1976. In June 1993, she entered Chulalongkorn University and received the Bachelor of Engineering in Electrical Engineering Program in May 1997.

She received the Master degree of Engineering in Electrical Engineering Program in May 2000 from the Graduate School of Chulalongkorn University and further her study in June 2000, as a Ph.D. student. She was financial supported by National Science and Technology Development Agency (NSTDA) through "Sis Kon Kuti" Program during Master degree study. Since June 2000, she has received Royal Golden Jubilee Scholarship from Thailand Research Fund.

Between July 2001 and October 2002, he received the DAAD-RGJ Scholarship and worked as a guest scientist in Max-Planck-Institute for Solid State Research, Stuttgart, Germany. Moreover, she was also supported by Prof. Dr. Klaus von Klitzing for a funding of short research program at Max-Planck-Institute for Solid State Research, Stuttgart, Germany.